PROTON ELASTIC AND INELASTIC SCATTERING FROM ^{28}SI AND ^{24}MG AT INTERMEDIATE ENERGIES

by

Lin, Chin-Cheng Kenn

B. Sc., National Tsing Hua University, Taiwan, R. O. C., 1980

M. Sc., University of Oregon, U. S. A., 1983

THESIS SUBMITTED IN PARTIAL FULLFILLMENT OF

THE REQUIREMENT FOR THE DEGREE OF

MASTER OF SCIENCE

in the Department

of

Physics

SIMON FRASER UNIVERSITY

December 1986

APPROVAL

Name: Lin, Chin-Cheng Kenn

Degree: Master of Science

Title of thesis: Proton Elastic and Inelastic Scattering from ^{28}Si and ^{24}Mg at Intermediate Energies.

Examining Committee:

Chairman: Dr. D. H. Boal

Dr. O. F. Häusser
Senior Supervisor

Dr. K. S. Viswanathan

Dr. K. H. Hicks

Dr. S. Yen, External Examiner
Research Scientist, TRIUMF

Date approved: December 19th, 1986

PARTIAL COPYRIGHT LICENSE

I hereby grant to Simon Fraser University the right to lend my thesis, project or extended essay (the title of which is shown below) to users of the Simon Fraser University Library, and to make partial or single copies only for such users or in response to a request from the library of any other university, or other educational institution, on its own behalf or for one of its users. I further agree that permission for multiple copying of this work for scholarly purposes may be granted by me or the Dean of Graduate Studies. It is understood that copying or publication of this work for financial gain shall not be allowed without my written permission.

Title of Thesis/Project/Extended Essay

Proton Elastic and Inelastic Scattering

from $^{28}_{Si}$ and $^{24}_{Mg}$ at Intermediate Energies

Author:

(signature)

Chin-Cheng Kenn LIN

(name)

Mar 27 '87

(date)

ABSTRACT

This thesis is an experimental and theoretical study of proton-nucleus elastic and inelastic scattering. Three purposes are emphasized in this work. First of all, I will describe the experimental set-up at TRIUMF's Medium Resolution Spectrometer(MRS) which is used in the ($\vec{p}$,p') experiments. Secondly, the non-relativistic Optical Model(OM) is studied with either a phenomenological or a microscopic treatment, and the calculation is compared with data obtained at TRIUMF. Finally, predictions using the Dirac formulation are compared with the experiment by employing an optical potential with a Wood-Saxon(WS) form.

The data were taken at the TRIUMF's MRS using the target nuclei ^{24}Mg and ^{28}Si. Observables measured are :

1) differential cross sections and analyzing powers for ^{24}Mg at Ep=250 MeV.

2) differential cross sections and analyzing powers for ^{28}Si at Ep=200 MeV.

3) differential cross sections and analyzing powers for ^{28}Si at Ep=250 MeV.

4) differential cross sections for ^{28}Si at Ep=400 MeV.

Absolute cross sections were extracted with a solid angle defined by a wire chamber at the entrance of the MRS spectrometer.

The OM analysis includes both Schrödinger and Dirac formulations. The non-relativistic phenomenological optical model (POM) applies the Schrödinger equation with a Wood-Saxon form of potential, whereas the Dirac treatment of POM (RPOM) is found to have an unconventional (wine-bottle) shape. Calculations for inelastic collective states are done with the Distorted Wave POM(DWPOM) and the Dirac DWPOM(RDWPOM). The deformation lengths of the inelastic state are found and compared to those from electron scattering.

It was suggested that some version of the Impulse Approximation (IA) which includes Medium Modification(MM) might be appropriate for understanding nucleon-nucleus scattering at a nucleon bombarding energy above 100 MeV. Calculations are compared using the free t-matrix and, in addition, the density dependent G-matrix.

The microscopic study shows that a 3-parameter Fermi density from electron scattering with the finite size of the proton unfolded requires the empirical reduction of the potentials to approximately 70% to 85% of the impulse-model and MM values to obtain agreement with the data. The inelastic prediction using IA and MM shows that an extra ~30% reduction on the differential cross section of the first 2^+ state is necessary in order to fit the data well.

DEDICATION

To my parents

ACKNOWLEDGEMENT

I am very much indebted to Professor O. F. Häusser, my senior supervisor, for his guidance and his financial support for the experiments. He has been a source of encouragement and inspiration throughout the course of the research.

The author would also like to express gratitute to Professor R. Dymarz, Professor W. G. Love, Dr. R. I. Sawafta, Dr. K. H. Hicks, Dr. S. Yen, Dr. E. D. Cooper, Dr. R. Jeppesen and Dr. M. Vetterli for their numerous helpful discussions in the theories of nuclear structure and reactions.

I would like to thank everyone at TRIUMF MRS. Without their expertise, the experiments 335 and 272 would not have been completed as easily as they have been.

I am also grateful to Professor K. S. Viswanathan, Dr. K. Hicks and Dr. S. Yen for their supervision of this thesis.

Finally, very special thanks go to Lu-Ping, my wife, who supports me in every possible way she can.

TABLE OF CONTENTS

LIST OF FIGURES

LIST OF TABLES

CHAPTER I

INTRODUCTION

This research work mainly studies the strong interaction via proton scattering. The study of proton elastic and inelastic scattering at intermediate energies provides information on nuclear structure and reaction mechanisms which are either complementary or comparable to that obtained with other probes. Since the nucleon has size, and the interacton of the projectiles with target nuclei is a sophisticated many-body problem, a simplified model and reasonable approximations are suggested. It is obvious that some ambiguities when doing this are inevitable. It is well known that absorption is involved in the collision processes. Thus, the translucent model of nucleon scattering – the Optical Model(OM) – is assumed in this paper.

Conventionally, two approaches are possible with the Schrödinger formulation: the phenomenological optical model(POM) and the Impulse Approxition(IA).

1. POM. The POM has a potential based on the Schrödinger equation with Wood-Saxon(WS) form factors which describes the interaction with a complex formalism. The complex potential makes absorption possible which satisfies the translucent optical phenomenon. One often chooses the central and spin-orbit potentials as the dominant part of the optical potential. Therefore, the optical potential is described by four parts: real central, imaginary central, real spin-orbit and imaginary spin-orbit part. Each part has three parameters for a WS shape: strength, radius and diffuseness. The strength tells one how strong the potential is. The radius denotes how far the potential can reach. The diffuseness shows how quickly the potential dies out.

2. Impulse Approxition(IA) and Medium Modification(MM). In the POM, the

potential is obtained by fitting the observables phenomenologically with a WS form. It is more important (and complicated) to study the OM microscopically without fitting any (p,p) data. The microscopic OM prediction has two parts: the structure and the interaction. Nuclear charge distributions have been well studied by electromagnetic probes, especially electron scattering. The interaction for protons is described by IA or MM. For a bombarding energy above 100 MeV, one can think of the interaction between projectiles and the target nucleus as free scattering without being affected by other nucleons of the target(Ja70). Mathematically, this free N-N interaction is parameterized with a t-matrix form(Ke59, Cl64, Lo81). This very sudden collision approach is named the Impulse Approximation. A modifying effect can be included which considers Pauli-blocking(PB) and a short distance correction due to the strong repulsion force. This medium modification(MM) can be described by introducing a density dependent(DD) G-matrix(Br67, Ge82, Ge83, Ri84). The nucleon-nucleon interaction related to MM is taken from the PARIS83 force(Ri84). It will be shown that at intermediate energy(200 to 400 MeV), MM results in better agreement with the data than the IA does.

Recently, the Dirac approach which is constructed from a Lorentz Scalar term and a time-like Lorentz vector term(Ar81, Sh85) is found to be very successful in describing proton scattering processes. Basically, two relativistic (Dirac) approaches for nucleon-nucleus scattering have been studied:

1. Dirac (Relativistic) Phenomenological Optical Model(RPOM). In this model, the effective potential is decribed with four parts: real-vector, imaginary-vector, real-scalar and imaginary scalar part(Du56, Sa83, Sa83a). The effective central and spin-orbit potentials are the combinations of these four parts with an unconventional (wine-bottle) shape of real-central potential for a projectile energy between 100 and 400 MeV(or higher). The effective potential of RPOM has the deformed shape near the center of the nucleons. This wine-bottle shape cures the problem of the POM which cannot predict

the observables very well.

2. Relativstic Impulse Approximation. This approach will not be discussed in this work.

For the inelastic scattering process, the optical potential is deformed. Distorted waves obtained with certain deformation lengths of the potential are used to describe the excitation of collective states in both Schrödinger(Sh69, Sa83a) and Dirac(Co81, Pi83, Sa83a) formulations.

The transition densities used for inelastic scattering were obtained from a modified single particle model(Br83, Wi85, Br86). Since the electron scattering process is well known, the result of transition matrix elements and harmonic oscillator parameters can be applied to proton scattering directly. Finally, the nuclear matter density is taken from the three parameter Fermi model(Ja74) of (e,e) experiments by unfolding the size of the proton.

CHAPTER 2

THEORETICAL BACKGROUND

2.1 Scattering Theory

If one thinks of the incident particles as an incoming wave and the target nuclei as a potential well, then scattering theory can be treated as a perturbation problem in quantum mechanics. To study the scattering phenomenon, one has to know how many particles are scattered into a certain direction and with what kind of intrinsic spin. The observables to be studied here are differential cross sections and analyzing powers. The definition of differential cross section $\frac{d\sigma}{d\Omega}$, polarization P and analyzing power Ay for proton scattering for spin-zero target nuclei is as follows:

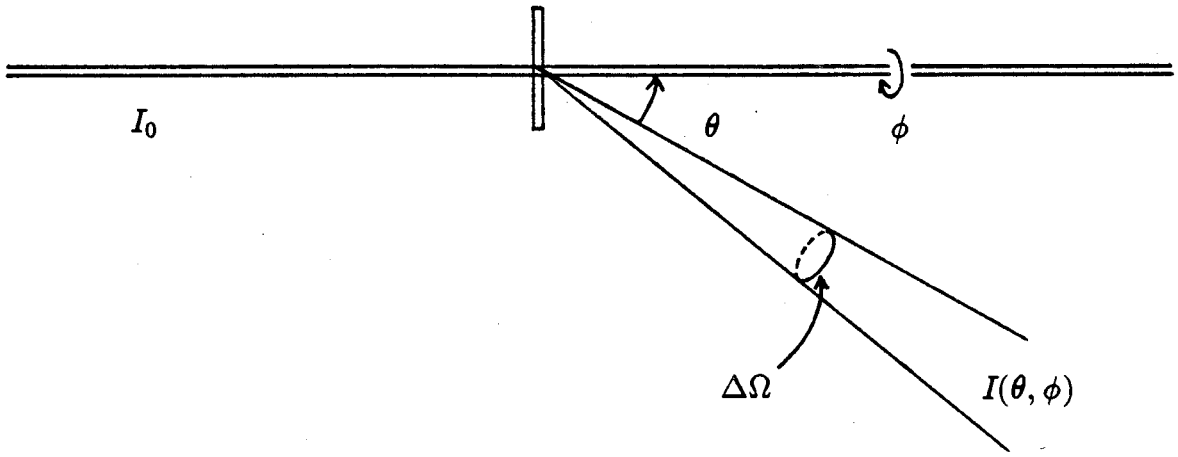

Fig. 2.1 Simplied diagram of the scattering process.

If I_0 is the number of particles incident from the left hand side in figure 2.1, and $I(\theta, \phi)$ is the number of these particles scattered into the $d\Omega$ cone, then

$$\frac{d\sigma}{d\Omega} \equiv \frac{I(\theta, \phi)}{I_0}. \tag{2.1}$$

If the Pauli matrices $\vec{\sigma}$ describes the spin form of the incident particle, then

$$P \equiv < \vec{\sigma} > . \tag{2.2}$$

For the projectile nucleons with the differential cross section of spin-up particles $\sigma_\uparrow$, spin-down particles $\sigma_\downarrow$ and incoming beam polarizations $P_\uparrow$ and $P_\downarrow$ respectively, the analyzing power is defined as:

$$Ay \equiv \frac{\sigma_\uparrow - \sigma_\downarrow}{P_\uparrow \sigma_\downarrow + P_\downarrow \sigma_\uparrow}. \tag{2.3}$$

Alternately, one could obtain the representations of them by solving the Schrödinger equation with a small perturbation. For the initial and final states Φ_i, Φ_f, the transition matrix element T_{fi} is defined to as:

$$T_{fi} \equiv < \Phi_f | \dot{T^+} | \Phi_i > . \tag{2.4}$$

where T^+ is the outgoing transition operator. For non-spinflip case in the asymptotic region, one has:

$$\begin{aligned} \Phi_i &= e^{i\vec{k}\cdot\vec{r}} \chi^i \\ \Phi_f &= \left(e^{i\vec{k}\cdot\vec{r}} + \frac{e^{ikr}}{r} f(\theta, \phi) \right) \chi^i \end{aligned} \tag{2.5}$$

$\chi^i (= \chi^f)$ is the initial spinor of the projectile.

The complex transition amplitude can be written as:

$$f(\theta,\phi) = -\frac{\mu}{2\pi\hbar^2} T_{fi}. \tag{2.6}$$

One can define the transition amplitude in the following way:

$$f(\theta,\phi) \equiv g(\theta) I + h(\theta)\vec{\sigma}\cdot\hat{n}. \tag{2.7}$$

where g, h are complex functions of energy and scattering angle and $\hat{n} = \hat{k}_i \times \hat{k}_f$ with $\vec{k}_i$, $\vec{k}_f$ the momentum of the incoming and outgoing particles respectively.

Then the differential cross section and analyzing power can be found as:

$$\frac{d\sigma}{d\Omega} \equiv (f\chi^i)^\dagger (f\chi^i) = |g(\theta)|^2 + |h(\theta)|^2 + 2Re(gh^*)\vec{P}\cdot\hat{n}. \tag{2.8}$$

$$A_y \equiv <\sigma_n> = \frac{2Re(gh^*)}{(|g(\theta)|^2 + |h(\theta)|^2)}. \tag{2.9}$$

where

$$\vec{P} = \chi^{i+}\vec{\sigma}\chi$$

To get the exact form of $f(\theta,\phi)$, it is necessary to solve the wave equation with a perturbation being the optical model potential. The wave equation could be either the Schrödinger or Dirac equation. The Dirac equation seems to work best at energies above 200 MeV.

2.2 Optical potential: formal(OM) and phenomenological(POM)

In order to describe the nucleon-nucleus interaction, one applies the general optical potential(Sh68) U_{OM} as

$$U_{OM} \equiv V_{Coul}(r) + V_{RC} f_{RC}(r) + i\left(W_{IC}(r) - 4W_D(r)\frac{d}{dr}\right) f_{IC}(r)$$

$$+ \left(\frac{\hbar}{m_\pi c}\right)^2 \left[V_{RSO}(r)\frac{1}{r}\frac{d}{dr} f_{RSO}(r) + iW_{ISO}(r)\frac{1}{r}\frac{d}{dr} f_{ISO}(r)\right] \vec{\sigma}\cdot\vec{L}. \qquad (2.10)$$

where

$$V_{Coul} = \begin{cases} \frac{Ze^2}{r}, & \text{if } r \geq R_C; \\ \frac{Ze^2}{2R_C}\left[3 - (\frac{r}{R_C})^2\right], & \text{otherwise.} \end{cases} \qquad (2.11)$$

and R_C is the Coulomb radius of the target.

Phenomenologically, the Wood-Saxon form is applied:

$$f_x(r) = \left\{1 + exp\left[\frac{(r - R_x)}{a_x}\right]\right\}^{-1}. \qquad (2.12)$$

where

$$R_x = r_x A^{\frac{1}{3}}. \qquad (2.13)$$

W_{IC} and W_D corresponds to volume and surface absorption for the central potential respectively. The surface absorption term $4W_D\frac{d}{dr}f_{IC}(r)$ is included because the volume term is damped at low energy due to Pauli blocking(PB)(Sa83a). For the intermediate or high energy range, the volume term dominates most of the absorption. Equation 2.10 is the so called POM potential.

Formally, the optical potential U_{OM} does not need the Wood-Saxon 3-parameter form. The following assumptions are made for the formal U_{OM}:

1. It has no discontinuity.

2. It vanishes at infinity.

3. There are scattering parts as well as absorption parts.

4. It ignores the very detailed features of the nuclear structure.

5. The reduced mass is replaced by the reduced relativistic energy because the speed of the projectile is very high compared to the classical case.

It is very helpful to solve the Schrödinger equation since the Dirac formulation result has to be consistent with it. The time evolution of the system is thus governed by this formula from Schrödinger formulation:

$$(E - H)\Psi = 0. \tag{2.14}$$

where the full Hamiltonian is

$$H = H_0 + V + H(\xi). \tag{2.15}$$

H_0 is the kinetic energy operator for the incident nucleon.

V is the interaction potential.

$H(\xi)$ is the internal Hamiltonian of the target nucleus as a function of all the internal coordinates ξ.

The total wavefunction Ψ is a linear combination of basis functions Φ_α from a complete set of eigenfunctions:

$$\Psi = \sum_\alpha \psi_\alpha \Phi_\alpha. \tag{2.16}$$

where ψ_α describes the motion of the projectile relative to the target and

$$H(\xi)\Phi_\alpha(\xi) = \epsilon_\alpha \Phi_\alpha(\xi). \tag{2.17}$$

In order to find the formal representation of the optical model potential, it is convenient to introduce two types of scattering channels and two types of projection operators. Following equation 2.15, the elastic channel state can be described as:

$$\Psi_{el} \equiv \psi_0 \Phi_0. \tag{2.18}$$

Define P and Q as the elastic and the inelastic channel projection operators respectively, i.e., define:

$$\begin{aligned} P\Psi &\equiv \Psi_{el} \\ Q\Psi &\equiv \Psi_{inel} \end{aligned} \tag{2.19}$$

Then,

$$P\Psi(\vec{r},\xi) = \psi_0(\vec{r})\Phi_0(\xi). \tag{2.20}$$

and,

$$P + Q = 1. \tag{2.21}$$

$$P^2 = P. \tag{2.22}$$

$$Q^2 = Q. \tag{2.23}$$

$$PQ = QP = 0. \tag{2.24}$$

Thus,

$$Q\Psi(\vec{r},\xi) = \Psi(\vec{r},\xi) - \psi_0(\vec{r})\Phi_0(\xi). \tag{2.25}$$

One finds the following relations by using equations 2.15 thruogh 2.25:

$$P = |\Phi_0(\xi) >< \Phi_0(\xi)|. \tag{2.26}$$

$$Q = \sum_{\alpha \neq 0} |\Phi_\alpha(\xi) >< \Phi_\alpha(\xi)|. \tag{2.27}$$

From 2.14, we get

$$(E-H)(P+Q)\Psi = 0. \tag{2.28}$$

$$(E-H)P\Psi = -(E-H)Q\Psi. \tag{2.29}$$

After some simple mathematics, a neat expression is obtained:

$$\left(E - PHP - PHQ\frac{1}{E-QHQ}QHP\right)P\Psi = 0. \tag{2.30}$$

The result of the optical potential is listed(Sa83a):

$$U(r) = < \Phi_0|VQ\frac{1}{E-QHQ}QV|\Phi_0 > + < \Phi_0|V|\Phi_0 > . \tag{2.31}$$

One should notice that the U(r)=U_{OM} is actually a combination of the interaction potential and internal Hamiltonian of the target nucleus and not just either one of them. Also, the first term on the right hand side of equation 2.31 weakly couples non-elastic channels to the elastic channel. For the high energy case(comparing to the interaction potential strength), this term is small compared with the last term. Thus,

$$U \approx < \Phi_0|V|\Phi_0 > . \tag{2.32}$$

with the overall interaction represented by the sum of each nucleon in the nucleus:

$$V(\vec{r},\xi) \equiv \sum_{i=1}^{A} v_i(\vec{r}-\vec{r}_i). \tag{2.33}$$

Thus

$$U \approx < \Phi_0|\sum_i v_i(\vec{r}-\vec{r}_i)|\Phi_o > . \tag{2.34}$$

or in the integral form:

$$U \approx \int d\vec{r'} v(\vec{r} - \vec{r'}) \rho(\vec{r'}). \tag{2.35}$$

where

$$\rho(\vec{r'}) = < \Phi_0 | \sum_i \delta(\vec{r}_i - \vec{r'}) | \Phi_0 > . \tag{2.36}$$

is the matter density distribution, and for short range v_i, one may use the $\delta-$interaction for v_i and get:

$$U = (constant)\rho(\vec{r}). \tag{2.37}$$

Thus, in the optical model approach, the potential follows the density by a simple form at high energy, and is linear in the matter density for the short range case which is the case for strongly interacting particles.

The transition matrix element can be expressed in terms of the Optical Model potential as:

$$T_{fi} = < \Phi_f | T^+ | \Phi_i > = < \Phi_f | U | \psi_i^+ > . \tag{2.38}$$

and

$$|\psi_i^+ > = \Omega^+ | \Phi_i > . \tag{2.39}$$

$$\Omega^\pm \equiv (1 + G^\pm U). \tag{2.40}$$

is the Moller wave operator, and

$$G^\pm = (E - H \pm i\epsilon)^{-1}. \tag{2.41}$$

By applying equations 2.6 to 2.9 and 2.38 one can find the observables of the elastic scattering process with an Optical Model analysis.

2.3 Standard optical Model(DWPOM): Schrödinger treatment

The Standard Optical Model is simply the POM with a distorted wave treatment. This is also called the Distorted Wave Phenomenological Optical Model(DWPOM). The Distorted Wave Born Approximaton with WS potentials has also proved suitable to describe proton scattering from deformed nuclei(Sh69, Sa83a). From the previous section, it is clear that the optical model potential is related to the matter density. It is thus reasonable to describe the inelastic collective state by deforming the shape of the nuclear matter. Define the distorted wave χ for the projectile as the following:

$(H_0 + U_0 - E)\chi = 0$ where U_0 is a spherical optical potential.

If for the deformed poential $U_D \cong U_0 + \Delta U$ where ΔU is the non-spherical part of the optical potential, then the transition matrix element for a single excitation of 2^I−pole collective mode of an even target nucleus is given by:

$$T_{fi} = \langle \chi^-(\vec{k}_f, \vec{r}) | \langle IM | \Delta U | 00 \rangle | \chi^+(\vec{k}_i, \vec{r}) \rangle. \tag{2.42}$$

Here $|IM\rangle$ describes a collective excited state with spin I and projection M and χ^+, χ^- are the incoming and outgoing distorted waves of the projectile. The parity of the state is given by $\pi_f = (-1)^I$.

The deformed interacton potential ΔU is obtained by deforming the optical model potential of equation 2.10 and keeping terms to first order in the deformation parameter. One can write ΔU as:

$$\Delta U \equiv \Delta U_C + \Delta U_{RE} + \Delta U_{IM} + \Delta U_{SO}. \tag{2.43}$$

where

ΔU_C, ΔU_{RE}, ΔU_{IM}, ΔU_{SO} refer to Coulomb, real, imaginary and spin-dependent

parts repectively. Define the deformed radius R'(Bl64) as:

$$\rightarrow R' = R + \alpha(\hat{r}). \tag{2.44}$$

with

$$\alpha(\hat{r}) = \sum_{L,M} \xi_{L,M} (Y_L^M)^*(\hat{r}). \tag{2.45}$$

and $\xi_{L,M}$ is the dynamical coordinate which describes the surface displacement. Then,

$$\begin{aligned} f_x(r) \longrightarrow f_x^{defo.}(r) &= f_x(r, R + \alpha(\hat{r}), a) \\ &\approx f_x(r, R, a) + \alpha(\hat{r}) \frac{\partial f_x}{\partial R}. \end{aligned} \tag{2.46}$$

The deformed central potential has the real and imaginary parts as:

$$\Delta U_{RC} = -V_{RC} \alpha_{RC}(\hat{r}) \frac{\partial}{\partial R_{RC}} f(r, R_{RC}, a_{RC}). \tag{2.47}$$

$$\Delta U_{IC} = -\alpha_{IC}(\hat{r}) \left(W - 4 a_{IC} W_D \frac{\partial}{\partial r} \right) \frac{\partial}{\partial R_{IC}} f(r, R_{IC}, a_{IC}). \tag{2.48}$$

The deformed spin-orbit piece ΔU_{SO} can be written as the sum of two terms (Sh69), $\Delta U_{SO} \equiv \Delta U_{SOL} + \Delta U_{SOD}$ where(SOL for $\vec{\sigma} \cdot \vec{L}$ term and SOD for $\vec{\nabla}$ term):

$$\Delta U_{SOL} = \left[\frac{\hbar}{m_\pi c} \right]^2 \left[V_{SO} \alpha_{SO} \frac{i}{r} \frac{\partial}{\partial r} \left(\frac{\partial f_{SO}}{\partial R_{SO}} \right) + i W_{SO} \alpha_{ISO} \frac{1}{r} \frac{\partial}{\partial r} \left(\frac{\partial f_{ISO}}{\partial R_{ISO}} \right) \right] \vec{\sigma} \cdot \vec{L}. \tag{2.49}$$

$$\Delta U_{SOD} = \left[\frac{\hbar}{m_\pi c} \right]^2 \left[V_{SO} \frac{\partial f_{SO}}{\partial R_{SO}} \vec{\sigma} \cdot \left(\vec{\nabla} \alpha_{SO} \times \frac{1}{i} \vec{\nabla} \right) + i W_{SO} \frac{\partial f_{ISO}}{\partial R_{ISO}} \vec{\sigma} \cdot \left(\vec{\nabla} \alpha_{ISO} \times \frac{1}{i} \vec{\nabla} \right) \right] \tag{2.50}$$

The deformed Coulomb part up to the first order is:

$$\langle IM|\Delta U_C|00\rangle = \frac{3ZZ'e^2}{R_C^2}\frac{C(I)(Y_I^M)^*}{2I+1}\begin{cases}(\frac{R_C}{r})^{I+1}, & \text{if } r \geq R_C;\\ (\frac{r}{R_C})^I, & \text{otherwise.}\end{cases} \tag{2.51}$$

For the even target in the final state $|IM\rangle = |I0\rangle$ with an orbital angular momentum L, the real-central α_{RC} becomes:

$$\alpha_{RC} \equiv R_{RC}\sum_L \xi_{L0}Y_L^0(\theta',\phi'). \tag{2.52}$$

Then, one can get:

$$\langle\Phi_f|\alpha_{RC}|\Phi_i\rangle \sim R_{RC}\beta_L(Y_L^M)^*. \tag{2.53}$$

where $\beta_L \equiv \xi_{L0}$ is the deformation parameter. The $(R_{RC}\beta_L)$ can be written as δ_L – the deformation length.

The final T–matrix thus has three parts:

$$T_{fi} \equiv [T_0 + T_{SOL} + T_{SOD}]_{i\to f}. \tag{2.54}$$

with

T_0 is the non spin-orbit term.

T_{SOL} is the $\vec{\sigma}\cdot\vec{L}$ term from equation 2.48.

T_{SOD} is the SOD term from equation 2.49.

The final expression of the transition matrix(see equation 2.42) has been solved by Sherif(Sh68)and Sawafta(Sa83a) which includes all the three terms in it. We refer to their work for the full expression of the T–matrix.

Finally, the expressions of observables in terms of the T-matrix form are found and listed. The inelastic differential cross section is given by:

$$\frac{d\sigma}{d\Omega} = \frac{m^{*2}}{4\pi^2\hbar^4}\frac{k_f}{k_i}\frac{1}{2}\sum_{\mu_i\mu_f M}|T(\mu_i;\mu_f M)|^2$$

$$= \frac{m^{*2}}{4\pi^2\hbar^4}\frac{k_f}{k_i}\sum_{\mu_f M}|T(\frac{1}{2};\mu_f M)|^2 \tag{2.55}$$

for spin$-\frac{1}{2}$ particle where $(\sum_{\mu_i})$ gives rise to a factor of 2.

The inelastic analyzing power becomes:

$$A_y(\theta) = \frac{-2Im\left[\sum_M(-)^M T(\frac{1}{2};-\frac{1}{2}M)T^*(\frac{1}{2};\frac{1}{2}M)\right]}{\sum_{\mu_f M}|T(\frac{1}{2};\mu_f M)|^2}. \tag{2.56}$$

This model was found to be somewhat successful for low-lying states at low energies. It will also be shown in this paper that it nicely describes the scattering processes at the intermediate energies.

2.4 Phenomenological Dirac Optical Model(RPOM, RDWPOM)

The Dirac Optical Model is also known as the relativistic Phenomenological Optical Model(RPOM). Based on the Dirac equation, the relativistic optical model approach was constructed recently(Ar81, Co81, Sa83a, Sh86). Both the macroscopic WS fit and the microscopic calculations were found to do well when compared with the experimental data(the microscopic way will not be discussed here). In this section, the methods of RPOM and RDWPOM are introduced. The Dirac optical model has the mixture of potentials consisting of a Lorentz scalar part U_S and the time-like component of a vector part U_V. The equation governing proton elastic scattering is :

$$\{\vec{\alpha}\cdot\vec{p}+\beta[m+U_S(r)]+U_V(r)+V_C(r)\}\psi(\vec{r})=E\psi(\vec{r}). \tag{2.57}$$

where

α, β are 4 by 4 Dirac matrices:

$$\alpha=\begin{pmatrix}0 & \vec{\sigma}\\ \vec{\sigma} & 0\end{pmatrix}. \tag{2.58}$$

$$\beta=\begin{pmatrix}I & 0\\ 0 & -I\end{pmatrix}. \tag{2.59}$$

$\vec{p}$ is the momentum operator of the incident proton with $\vec{p}=-i\vec{\nabla}$

m is the rest mass of the incident proton.

Ψ is the Dirac 4-spinor.

V_C is the Coulomb potential which is determined from the empirical nuclear charge distribution given by electron scattering experiment.

E is the proton total energy.

It is well known that the nucleon-nucleon interaction can be interpreted by the exchange processes of elementary particles. The major part of the interaction is considered as the combination of "one boson exchange potential" (OBEP) and "two pion exchange potential"(TPEP) in the asymptotic region. The dominant characteristics of the nucleon-nucleus interaction for a spin-zero isospin-zero target nucleus are expected to be represented by the exchange of neutral scalar and vector mesons(Ar81, Co81, Sh86). This exchange process is found to be directly related to the scalar and vector potentials of the Dirac formulation. The main effects of using a mixture of a scalar U_S and a vector U_V potential in the Dirac equation was originally discussed by Fury(Fu36) who pointed out that to the lowest order in $(\frac{v}{c})$, the sum of U_V and U_S contributes to the central potential, while the difference $U_V - U_S$ affects the spin-orbit part. It was found that this feature of mixed potential successfully described both elastic and inelastic scattering at intermediate energies(Co81, Ar82, Sa83a, Sh86).

If one writes the spinor as a 2-component Dirac spinor ψ:

$$\psi = \begin{bmatrix} \psi_u \\ \psi_l \end{bmatrix}. \tag{2.60}$$

with an upper and a lower part, then one preserves not only the Dirac version but one obtains the standard optical model-like form.

Now, using equation 2.58, 2.59 and 2.60 in 2.57, one obtains:

$$\left[\begin{pmatrix} 0 & \vec{\sigma}\cdot\vec{p} \\ \vec{\sigma}\cdot\vec{p} & 0 \end{pmatrix} + \begin{pmatrix} m+U_S & 0 \\ 0 & -(m+U_S) \end{pmatrix} + \begin{pmatrix} U_V+V_C & 0 \\ 0 & U_V+V_C \end{pmatrix}\right]\begin{bmatrix} \psi_u \\ \psi_l \end{bmatrix} = E\begin{bmatrix} \psi_u \\ \psi_l \end{bmatrix}. \tag{2.61}$$

giving

$$\vec{\sigma}\cdot\vec{p}\psi_l + (m + U_S + U_V + V_C)\psi_u = E\psi_u. \tag{2.62}$$

$$\vec{\sigma}\cdot\vec{p}\psi_u + (U_V + V_C - m - U_S)\psi_l = E\psi_l. \tag{2.63}$$

From 2.63, one solves for ψ_l:

$$\psi_l = \frac{1}{D}\vec{\sigma}\cdot\vec{p}\psi_u. \tag{2.64}$$

with

$$D = D(r) \equiv E + m + U_S - U_V - V_C. \tag{2.65}$$

Now, define a new wave function in order to get the Schrödinger equivalent equation:

$$\psi_u(\vec{r}) \equiv D^{1/2}\phi_u(\vec{r}). \tag{2.66}$$

Then, the Schrödinger-like equation is found after a few substitutions:

$$\left[\frac{p^2}{2m} + U_{eff}(r) + U_{so}(r)\vec{\sigma}\cdot\vec{L}\right]\phi_u(r) = \frac{k^2}{2m}\phi_u(r) \tag{2.67}$$

where

$$U_{eff} = \frac{1}{2m}\left[\frac{3}{4}\left(\frac{D'}{D}\right)^2 - \frac{1}{2}\frac{D''}{D} - \frac{1}{r}\frac{D'}{D}\right] + U_S + \frac{E}{m}(U_V + V_C) + \frac{1}{2m}\left[U_S^2 - (U_V + V_C)^2\right]. \tag{2.68}$$

$$U_{so}(r) = -\frac{1}{2m}\frac{1}{D}\frac{1}{r}\frac{dD}{dr}. \tag{2.69}$$

and $k^2 = E^2 - m^2$

Equation 2.67 which produces equivalent elastic scattering is called the "Schrödinger equivalent equation". The ϕ_μ has the same asymptotic behavior as ψ_μ in the absence of the Coulomb potential because of the short range of U_V and U_S.

For the neutral vector meson exchange portion, one gets a repulsive U_V, while for the neutral scalar meson exchange, one gets an attractive potential U_S. One can see that U_S and U_V tend to cancel each other when calculating U_{eff}.

Phenomenologically, one writes the U_V and U_S with:

$$U_V(r) = V_{RV} f_{RV}(r, R_{RV}, a_{RV}) + iW_{IV} f_{IV}(r, R_{IV}, a_{IV}). \quad (2.70)$$

$$U_S(r) = V_{RS} f_{RS}(r, R_{RS}, a_{RS}) + iW_{IS} f_{IS}(r, R_{IS}, a_{IS}). \quad (2.71)$$

where f_i is the 3-parameter WS form(see 2.11).

The inelastic standard optical model has successfully described nucleon-nucleus scattering at low energy. For energies above 50 MeV(especially above 150 MeV), it didn't predict the data so well. It was then suggested that the Dirac model which describes the elastic scattering so well(Ar81, Ar82) should also be able to describe the low-lying collective states. Satchler (Sa83) and Sawafta(Sa83a) have recently studied the inelastic observables for the low-lying states near 200 MeV and up for various nuclei. Olmer(Ol84) studied ^{28}Si and other nuclei between 80 and 200 MeV. Hintz(Hi84) interpreted some data on ^{28}Si with energies up to 800 MeV. Both Olmer and Hintz fitted their elastic scattering data and available reaction cross sections with elastic POM potentials. This paper presents the inelastic data together with the standard model and the Dirac model calculations for ^{28}Si and ^{24}Mg. These results are then compared to those obtained by Olmer, Hintz and Sawafta.

The Dirac theory of the inelastic process is also based on deforming the vector and the scalar potentials just as in the non-relativistic standard optical model where one deforms the central and spin-orbit potentials. Thus, the potentials U_V and U_S described in 2.70 and 2.71, can be written as deformed potentials:

$$U_X^D(r) = V_{RX} f_{RX}(r, R_{RX} + \alpha_{RX}(\hat{r}), a_{RX}) + iW_{IX} f_{IX}(r, R_{IX} + \alpha_{IX}(\hat{r}), a_{IX}). \quad (2.72)$$

where X stands for V(vector) or S(scalar) part.

Then, U_X^D can be expressed in terms of spherical and non-spherical parts:

$$U_X^D = U_X(r) + \Delta U_X(\vec{r}). \tag{2.73}$$

with

$$\Delta U_X(\vec{r}) = \alpha_{RX}(\hat{r}) V_{RX} \frac{\partial f_{RX}}{\partial R_{RX}} + i\alpha_{IX}(\hat{r}) W_{IX} \frac{\partial f_{IX}}{\partial R_{IX}}. \tag{2.74}$$

The detailed calculation of the transition matrix T_{fi} and form factors for the inelastic scattering is listed in Sh68 and Sa83a. It is interesting to note that the Dirac treatment predicts an effective potential in the shape of a wine-bottle bottom which acts like a density dependent potential. This will be demonstrated in chapter 5.

2.5 DWIA and DWMM

DWIA and DWMM stand for Distorted Wave Impulse Approximation and Distorted Wave Medium Modification respectively. The nucleon-nucleus(NA) interaction can be simply approximated by assuming a single nucleon-nucleon(NN) collision at energies above 80 MeV. This single scattering model is the so-called Impulse Approximation(IA).

The inleastic process can be treated using the distorted wave approach. This is called DWIA. The related transition amplitude(or propagator) for nucleon scattering in the first Born approximation is:

$$f = V(\vec{q})\rho(\vec{q}). \tag{2.75}$$

where $V(\vec{q})$ and $\rho(\vec{q})$ are the Fourier transformations of the effective interaction potential and the momentum transition density respectively. This consideration of a single NN scattering which neglects the effects of other nucleons in the target is valid at high energies(Lo83, Fr85). For the energy range between 60 and 350 MeV, Medium-Modification such as Pauli-Blocking effects and short range correlations should be considered. This medium-modified approach , DWMM(Ge79, Ri84 and Dy85), is thus a refinement of the DWIA. The interaction of the DWIA with a pseudopotential t(r) by Love and Franey is refered to as LF later in this paper. The transition density is well described by the shell model calculation of Brown and Wildenthal(Br83, Wi85 and Br86) which describes electron scattering data very well provided "effective charges" for proton and neutron are introduced. The results from Brown are thus taken as the input of the (p,p') calculaton for 2^+. The spin-orbit as well as the tensor force give parts of the nuclear force for nucleon scattering. For this reason, the localized t-matrix (not the T-matrix which is a normal represention of the transition matrix) by LF can be written as:

$$t(\vec{r}) \equiv V^C(r) + V^{LS}(r)\vec{L}\cdot\vec{S} + V^T(r)S_{12}. \tag{2.76}$$

with the well-known expressions:

$$V^C(r) \equiv V_0^C(r) + V_\sigma^C \vec{\sigma}_1 \cdot \vec{\sigma}_2 + V_\tau^C \vec{\tau}_1 \cdot \vec{\tau}_2. \tag{2.77}$$

$$V^{LS}(r) \equiv V_0^{LS}(r) + V_\tau^{LS}(r) \vec{\tau}_1 \cdot \vec{\tau}_2. \tag{2.78}$$

$$V^T(r) \equiv V_0^T(r) + V_\tau^T(r) \vec{\tau}_1 \cdot \vec{\tau}_2. \tag{2.79}$$

$$S_{12} \equiv 3(\vec{\sigma}_1 \cdot \hat{r})(\vec{\sigma} \cdot \hat{r}) - \vec{\sigma}_1 \cdot \vec{\sigma}_2. \tag{2.80}$$

The Fourier transformation of $t(\vec{r})$ gives the first part of the transition amplitude.

$$t(\vec{q}) = \frac{1}{(2\pi)^{3/2}} \int e^{i\vec{q}\cdot\vec{r}} t(\vec{r}) d^3r. \tag{2.81}$$

After some manipulations, one finds for $t(\vec{q})$(Lo81, Ye83):

$$t(\vec{Q}) = V^C(Q) + \frac{i}{4} q V^{LS}(Q)(\vec{\sigma}_1 + \vec{\sigma}_2) \cdot \hat{n} - V^T(Q) S_{12}(\hat{Q}). \tag{2.82}$$

with

$$t'(\vec{q}) = V^C(q) + \frac{i}{4} Q V^{LS}(q)(\vec{\sigma}_1 + \vec{\sigma}_2) \cdot \hat{n} - V^T(q) S_{12}(\hat{q}). \tag{2.83}$$

with

$$\vec{Q} = \vec{k}_i + \vec{k}_f. \tag{2.84}$$

$$\vec{q} = \vec{k}_i - \vec{k}_f. \tag{2.85}$$

and $\hat{n} = \hat{k}_i \times \hat{k}_f$. The observables can be found in much the same way as for the POM.

Medium Modification uses a density dependent matrix, the G-matrix, instead of the free NN t-matrix in IA. This G-matrix not only takes care of the strong short range repulsion problem but also includes the Pauli-Blocking effect. Since the strength of interaction of a nucleon pair depends upon the density of the nuclear matter, the G-matrix is found to be weaker inside the nucleus than outside. At high energy, the

G-matrix approaches the complex t-matrix for the free NN scattering(IA). The force used is the PARIS83 free NN force which is based on meson exchange theory. For the elastic scattering process, the information of ground state density is (like the IA) taken from the 3 parameter Fermi model via electron scattering with the neutron density the same as the proton density. We find that both models(IA and MM) are not able to predict the data for light, non-spherical nuclei. By changing the optical potentials substantially(approximately 15% to 30% reduction), we obtain much better fits to the data than with the full strength. This will be explored latter in this paper.

CHAPTER 3

Experimental

3.1 General

A typical proton scattering experimental facility is shown in figure 3.1. It includes mainly 5 parts: source, beamline, target, counters and electronics and data aquisition system. The extracted polarized or unpolarized proton beam from the source strikes a thin target. The vast majority of the projectiles pass through the target without interacting with any target nuclei. The evacuated beamline contains magnetic elements(dipoles and quadrupoles), some beam profile monitors and a beam dump. The MRS spectrometer(see section 3.2) consists of a focussing quadrupole(Q) and a dispersing dipole(D) which bends scattered particles by about 60° and spatially seperates particles of different momenta. Position sensitive gas counters then detect the scattered particle and digital information for each event is recorded on magnetic tape. The spectrometer used for the present results is shown schematically in figure 3.2.

One of the results is a spectrum, the graph of position along the focal plane versus the number of particles detected at each position. It reveals a number of peaks each of which corresponds to the excitation of a particular state of the target nucleus. Figure 3.3 shows the typical large angle spectra for light nuclei with $\sim$ 140 keV resolution taken at TRIUMF, Spring 1986.

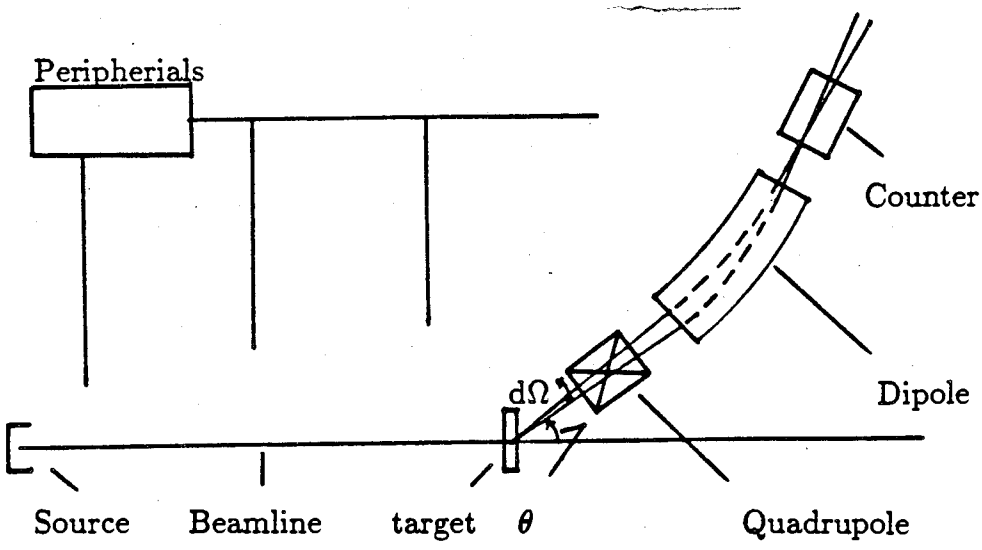

Figure 3.1 Typical proton scattering experimental facility layout.

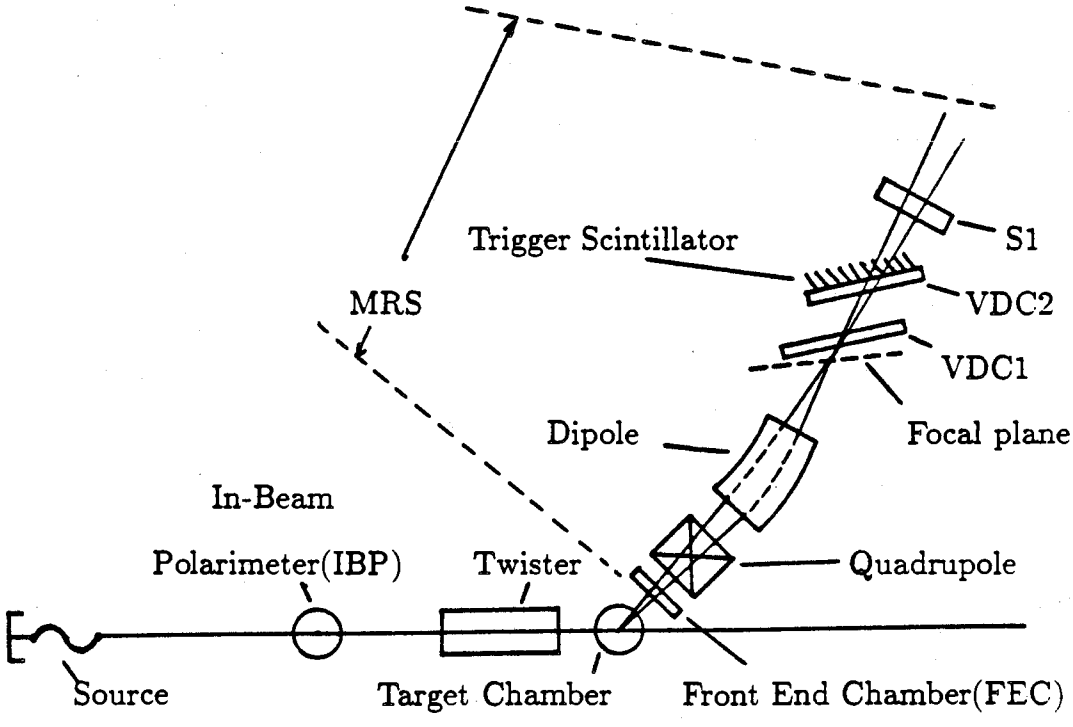

Figure 3.2 The geometry and outline of the TRIUMF MRS spectrometer for this experiment.

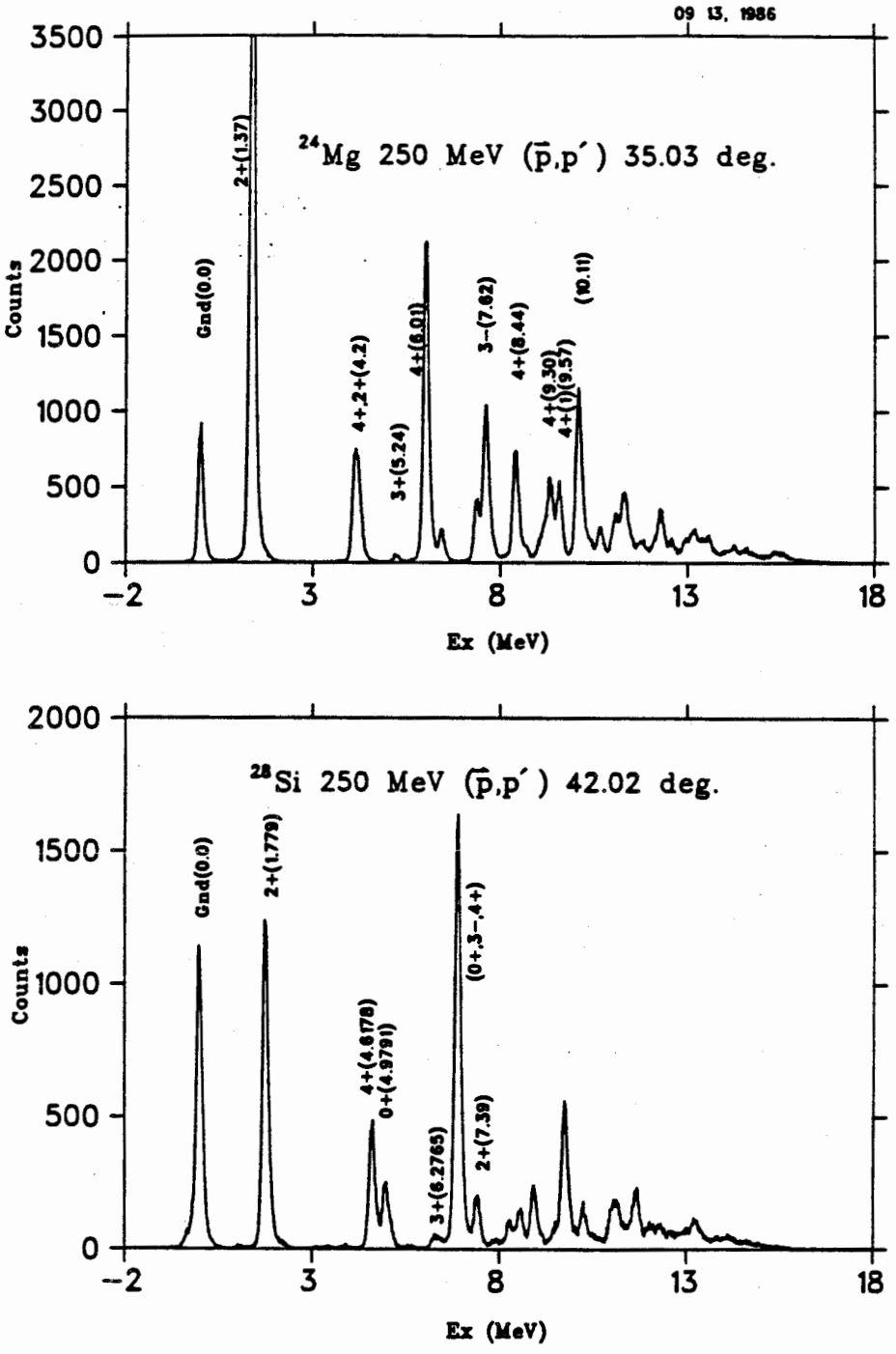

Figure 3.3 Large angle spectra for light nuclei with $\sim$ 140 keV resolution taken at TRIUMF. Shown on top is the ^{24}Mg spectrum for inelastic 35.03° MRS angle at 250 MeV. The spectrum below is for ^{28}Si 42.02°. The ground and 2^+ states are very clean in both spectra.

3.2 TRIUMF and MRS

TRIUMF is Canada's national Meson Facility. It provides world-leading facilities for experiments in subatomic research with beam of pions, muons, protons and neutrons. The TRIUMF accelerator is a six-sector isochronous cyclotron which is capable of accelerating H^- ions to a continuously varying extraction energy from 180 to 520 MeV by adjusting the radius of a stripping foil along a track inside the cyclotron. The stripper here can strip off electrons from H^- to get H^+ which is transported down the beamline.

The In-Beam Polarimeter(IBP) is placed at an intermediate focus of the beamline to detect the beam polarization. The beam intercepts a thin foil target and some protons that undergo nuclear reactions are scattered into the Medium Resolution Spectrometer(MRS). This is a large dipole magnet which analyzes particles from nuclear scattering as described above. The MRS is capable of detecting protons with energy resolution as low as 100 keV. The momentum acceptance is about 10% for particles up to 1.5 $\frac{GeV}{c}$.

The dipole and the quadrupole magnets are mounted on a framework which rotates horizontally around the scattering chamber. The dipole bends the particles' trajectory 60° in the vertical plane(bend plane) and disperses them over a focal plane. The quadrupole magnet only focuses in the horizontal plane allowing a larger solid angle to be accepted(and defocuses in the vertical plane as well). Focusing is accomplished by adjusting the optical parameters which describe the QD magnet system. The locations of the beam on the target X_I and focal plane X_f are described by:

$$\Delta X_I = R_{11(beam)}\Delta X_{source} + R_{12(beam)}\Delta\theta_{source} + R_{16(beam)}\frac{\Delta P_{(beam)}}{P_{(beam)}}. \tag{3.1}$$

$$\Delta X_f = R_{11(MRS)}\Delta X_I + R_{12(MRS)}\Delta\theta_I + R_{16(MRS)}\frac{\Delta P_{(MRS)}}{P_{(MRS)}}. \tag{3.2}$$

R_{ij}'s are the beam optics parameters which depend on the characteristics of the magnet system. The dispersion matching condition is:

$$\frac{R_{16(MRS)}}{R_{11(MRS)}} = R_{16(beam)}. \tag{3.3}$$

In this case, the momentum spread of the incident beam does not affect the resolution in the focal plane. This will give better position(energy) resolution at X_f.

The scattering chamber can be operated at small and large angle configurations: SAC and LAC, each of which has a different set-up and range of experimental angles. The range of LAC is from 16° to 135°, For SAC, it is from -7° to 16°.

3.3 MRS detectors and IBP

There are 5 detector sets in the MRS: Front End Chamber(FEC), Elastic Veto Scintillator(EV), Vertical Drift Chambers(VDC), Trigger Paddles(TP) and S1 Scintillator.

FEC: This first MRS detector is located just after the target to allow ray-tracing back to the target in order to set solid angle gates and to correct for aberrations in the MRS.

EV: This scintillator is placed just below the focal plane to pre-scale the elastically scattered particles(i.e., only count a small fraction of the elastic peak). In this way, one can increase the amount of useful data on tape and reduce the dead-time.

VDC: The heart of the MRS detectors is a pair of vertical drift chambers just above the focal plane and set at 45° with respect to the scattered protons. Each VDC consists of two crossed wire planes which give positions in the X(bend plane) and U(30° to X) directions: X1, X2, U1 and U2. This information is then transformed into X- and

Y-coordinates.

TP: There are 10 scintillator trigger paddles above the VDC's which are powered seperately and thus allow the experimenter to limit the amount of the focal plane which is considered in the trigger. Details are given in the MRS manual at TRIUMF(Hi86).

The In-Beam Polarimeter(IBP) is the primary monitor of the beam intensity and polarization. It consists of a thin CH_2 polyethylene target and two pairs of counter telescopes(each in coincidence with a recoil counter) that counts elastic proton-proton scattering events. The "real" event rate(per second) and the "accidental" event rate(formed by delayed coincidence) are counted in scalers and are periodically recorded on tape.

The intensity of the beam is proportional to the total event rate T:

$$T = (L - L_a) + (R - R_a). \tag{3.4}$$

where L=Left real rate, L_a=Left accidental rate; and R, R_a the same at the right.

The polarization is defined as:

$$P = \epsilon / A_y(CH_2). \tag{3.5}$$

where

$$\epsilon = \frac{(L - L_{ac}) - (R - R_{ac})}{(L - L_{ac}) + (R - R_{ac})}. \tag{3.6}$$

There is another monitor of the beam current, the Second Emission Monitor(SEM), which collects electrons from surface emission as the proton passes through several aluminum foils located downstream of the target. For small angle configuration(SAC), SEM is replaced by a Faraday brick. Normally, IBP and SEM give the incoming particle number to an accuracy of $\sim$ 1.5%.

Finally, two corrections of the beam polarization are given. First, is the spin-off (unpolarized) correction factor to correct for mechanical asymmetry for Left and Right side of the IBP.

$$\epsilon_{corr} = \frac{\epsilon_{on} - \epsilon_{off}}{1 + \epsilon_{on}\epsilon_{off}}. \tag{3.7}$$

This correction factor could be very large if the beam tune is poor. Nevertheless, a few percent still exist even with good beam.

The second correction is a small carbon correction factor. Since the CH_2 target was used instead of pure hydrogen, the (p,2p) reaction from carbon can contribute. A seperate run with a carbon target is needed. The final correction of the carbon can be written as:

$$\epsilon_{corr}(H) = P * A_y(H) = \frac{\epsilon_{corr} + \epsilon_c}{1 + \epsilon_{corr}\epsilon_c}. \tag{3.8}$$

with

$$\epsilon_c = \frac{N_L(C) - N_R(C)}{N_L(C) + N_R(C)}. \tag{3.9}$$

and $N_X(C) = X(C) - X_{ac}(C)$ is the scattered count from the carbon target detected by the IBP.

3.4 Data Aquisition

The detector and polarimeter system are interfaced to the on-line computer through CAMAC. The on-line computer is a Data General Eclipse S200. A generalized program called DACS was written to acquire and analyze data with this aquisition system. The data tapes can be analyzed by the Eclipse or by the VAX. A program called LISA(see chapter 4) can replay and refine the data off-line.

3.5 Targets

The targets(see Table 3.1) chosen are ^{24}Mg and ^{28}Si for this experiment. Three other targets are used for the purpose of obtaining the normalization factor and angle calibration result: CH_2, ^{208}Pb and Mylar($C_5H_4O_2$).

Target Thickness List

Target	**Ep(MeV)**	**Configuration**	**Thickness(mg/cm^2)**
^{24}Mg	250	SAC,LAC	20.5
^{28}Si	200,250,400	SAC,LAC	17.2
CH_2	200	SAC	12.1
$C_5H_4O_2$	200	LAC	24.6
CH_2	250	SAC,LAC	55.0
CH_2	400	SAC,LAC	12.1
^{208}Pb	200	SAC	(Not measured)
^{208}Pb	200	LAC	21.2
^{208}Pb	250	SAC,LAC	49.98
^{208}Pb	400	SAC,LAC	21.2

Table 3.1 Target thickness for different energies and configurations.

CHAPTER 4

DATA ANALYSIS

4.1 Genaral

Analysis of the experimental data consists of the replaying of the data tapes, extracting peak areas from the momentum spectra, calculating differential cross sections and analyzing powers and calibrating the MRS for angles and normalizations.

4.2 Spectrum Analysis

A 2-dimensional particle identification spectrum is obtained by using the time of flight and energy loss of the scattered protons. Different types of particles(p,d,π,...etc.) are in different regions of this spectrum. The focal plane position is determined using the VDC coordinates and simple geometry. Details are given in the MRS manual(Hi86). Ray tracing to the target is also done using the FEC and VDC coordinates. Gates are then set around the beam spot.

The focal plane spectra XF can be corrected to have a better resolution by the use of the FEC chamber coordinates. These corrections take into account aberrations due to trajectories passing through non-homogeneous regions of the magnetic field (analogous to optical aberations at the edges of a lens). The multiwire chambers can also identify the missing or multiple counts of the scattered particles, and thus determine the chamber efficiency.

4.3 Differential cross section and analyzing power

Since both unpolarized and polarized beams for incoming projectiles were used, two calculations are discussed in the following.

4.3.1 Unpolarized scattering

The center of mass differential cross section for an incident unpolarized beam can be formulated in this way:

$$(\frac{d\sigma}{d\Omega})_{CM} = \frac{AREA \times PSCL}{CL \times CE \times (n_B d\Omega_{lab.}) \times (n_T dx)} \left(\frac{d\Omega_{lab.}}{d\Omega_{CM}}\right). \tag{4.1}$$

where:

AREA is the counts for the excited state one is interested in.

PSCL is the prescale factor.

CL is the computer livetime which is the ratio of the pulses recorded by the computer over the pulses generated(and recorded in as a scaler).

CE is the wire chamber efficiency, the ratio of good proton events over proton events that produce a signal in each and every multiwire chamber.

n_B is the number of beam projectiles per unit time which can be derived from the IBP. The Faraday cup(SAC) and the SEM(LAC) numbers are used to double-check the n_B's validity.

$d\Omega_{lab.}$ is the differential solid angle of the beam:

$$d\Omega_{lab.} \cong \Delta\Omega_{lab.} = \frac{[\Delta X0 \times \Delta Y0 \times (50 \times 10^{-4})^2]cm^2}{L^2(cm^2)}. \tag{4.2}$$

where L is the distance between target chamber and FEC. In this experiment,

$$L = \begin{cases} 132\ cm, & \text{for SAC;} \\ 63\ cm, & \text{for LAC} \end{cases}$$

$n_T dx$ is the number of target atoms per unit area, often simply called thickness and $\Delta X0, \Delta Y0$ are measured in 50μm unit. In the unit of number per millibarn, we have:

$$n_T dx = \frac{\tau(\frac{mg}{cm^2}) * 10^{-3}(\frac{g}{mg})}{M_T(\frac{g}{mole})} * 6.02 \times 10^{23} \left(\frac{\#}{mole}\right) * 10^{-27} \left(\frac{cm^2}{mb}\right). \tag{4.3}$$

where τ is the thickness in unit $\frac{mg}{cm^2}$ and M is the atomic weight of the target nucleus.

4.3.2 Polarized scattering

First we need to find the polarization of the projectile from IBP analysis (see chapter 3). The corrected polarization is denoted $P_\uparrow$ and $P_\downarrow$ for spin-up and spin-down respectively. If one uses the simple notation σ for differential cross section, then,

$$\sigma = \frac{P_\uparrow \sigma_\downarrow - P_\downarrow \sigma_\uparrow}{P_\uparrow - P_\downarrow}. \tag{4.4}$$

The analyzing power can be calculated from differential cross sections and beam polarizations:

$$\sigma_\uparrow = \sigma_0 * (1 + P_\uparrow * A_y). \tag{4.5}$$

$$\sigma_\downarrow = \sigma_0 * (1 + P_\downarrow * A_y). \tag{4.6}$$

Thus, $\sigma_\uparrow - \sigma_\downarrow = P_\uparrow \sigma_\downarrow * A_y + P_\downarrow \sigma_\uparrow * A_y$. It turns out that the result has the simple form:

$$A_y = \frac{\sigma_\uparrow - \sigma_\downarrow}{P_\uparrow \sigma_\downarrow + P_\downarrow \sigma_\uparrow}. \tag{2.3}$$

4.4 Angle calibration

It is very important to find the exact laboratory angle of the MRS. The Y0 plane of the target multiwire chamber has 1,600 channels, where the separation of two adjacent channels is 50×10^{-4}cm. Chamber alignment is often not that precise and the center of Y0 does not coincide with the nominal MRS angle. Thus the real center of the MRS angle on Y0 plane has to be recalculated very carefully. Since there are different MRS structures and angle configurations, the angle calibration for different cases is required.

A way to determine the Y0 center is to compare the Y0XF graph(see figure 4.1) with a kinematics calculation(figure 4.2) of θ_L versus momentum. If we calculate the angle-dependent momenta for ^{12}C and H, we see that there could be a cross point for hydrogen ground state and carbon excited states(especially 4.439 MeV). Thus, for example, in 250 MeV SAC, we did the 7.51° CH_2 run to get enough counts on ^{12}C 3^-(4.439 MeV) state. Then, the kinematic calculation is done for those two states. From the calculation, a cross point of 7.55° was found. Now check the Y0-XF angle versus momentum plot for CH_2 run. It was then found that the cross point is 772 channels of the Y0 coordinate. Thus, we say that in this experiment, $\theta_C = 7.55°$ is at $Y_C = 772$ channels. Since the nominal MRS angle is 7.51 degree, we could find correspondingly what the Y0 center is:

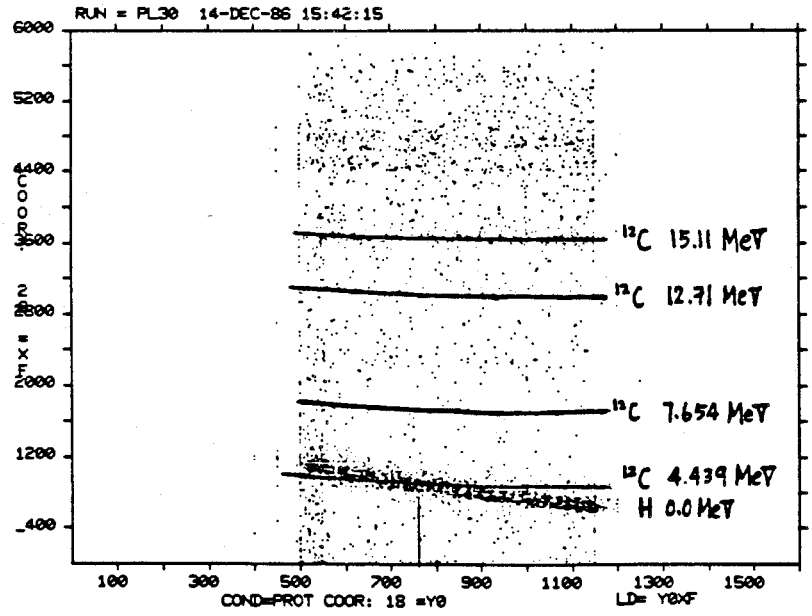

Figure 4.1 Y0XF 2-dimensional density plot of the outgoing beam for CH_2 7.51° MRS angle run at Ep=250 MeV.

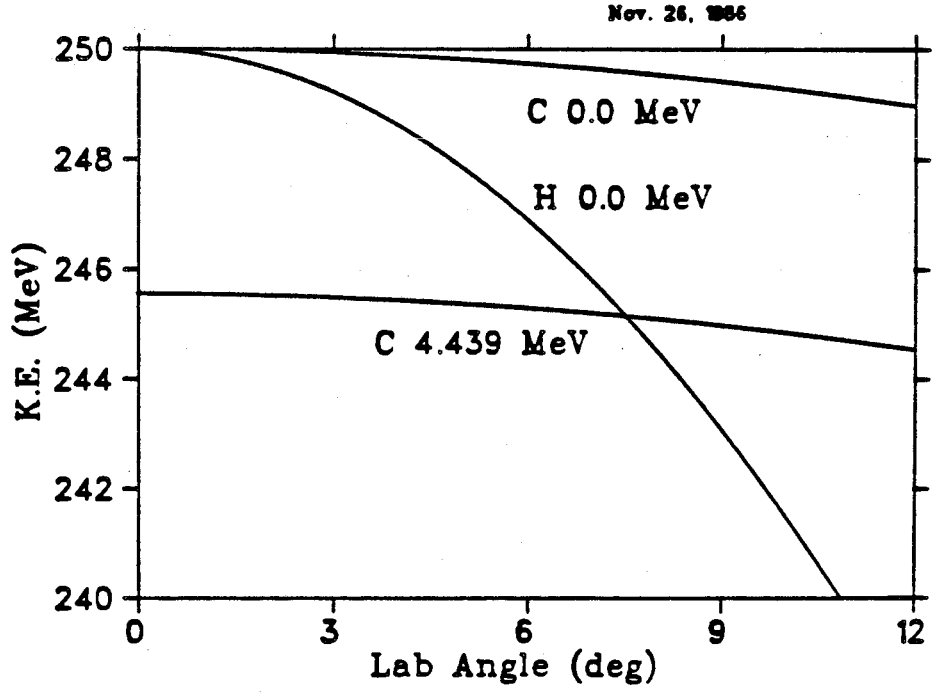

Figure 4.2 Kinematic calculation of projectile kinetic energy to laboratory angle for ^{12}C and H at Ep=250 MeV. A cross point is found at 7.55 lab. angle.

$$Y_{0C} \equiv Y_{0C(MRS)} = (\theta_C - \theta_{MRS})(deg) * \frac{\pi}{180}\left(\frac{rad}{deg}\right) * \frac{L(cm)}{50 * 10^{-4}(cm/channel)} + Y_C \quad (4.7)$$

Thus,

$$Y_{0C} \equiv \Delta\theta * R_\theta + Y_C. \quad (4.8)$$

where

$$R_\theta\left(\frac{channel}{deg}\right) = \begin{cases} 460.77, & \text{for SAC;} \\ 219.91, & \text{for LAC.} \end{cases} \quad (4.9)$$

Thus, in 250 MeV SAC run, its Y_{0C} for MRS angle is $772+18 \approx 790$ channels. This is the target chamber Y plane center of the MRS angle. For LAC, the CH_2 target is replaced by ^{208}Pb and the angle minimum can be compared to known data(for example, Hu86). The cross point method can also be applied to get the center of the MRS angle. The results for Y_{0C} are shown in table 4.1.

Ep(MeV)	Configuration	Y_{0C}	Angle shift
200	SAC	590	0.46°
200	LAC	728	0.33°
250	SAC	790	0.02°
250	LAC	762	0.17°
400	SAC	682	0.04°
400	LAC	840	-0.18°

Table 4.1 The MRS angle centers and angle shifts for different cases.

4.5 Normalization

The MRS allows one to calculate absolute differential cross sections using the front MWC to determine the solid angle acceptance. It is often not necessary to normalize the data to other states of known cross sections(e.g., H or ^{208}Pb). The proton-CH_2 experiment allows one to compare the values of hydrogen cross section with those calculated from phase shift analysis (Ji83, Ar81). Normally, the uncertainty is within 5%. The ^{208}Pb run could be used for normalization purposes using the previous data set by Hutcheon et al(Hu86).

4.6 Uncertainties

The uncertainty in the differential cross section is a combination of uncertainties from various sources. Each of the normalization factor pieces in equation 4.1 gives uncertainty, and the peak area of the momentum spectrum gives an uncertainty. We often refer to the former one as "systematic uncertainty" or "systematic error".

The relative error formula gives the uncertainty of the experiment. For example, a quantity S is of the form:

$$S \equiv \frac{A_1 * A_2 * .... * A_M}{B_1 * B_2 * .... * B_N}. \tag{4.10}$$

Then ΔS can be formulated as:

$$\Delta S = \sqrt{\sum_{m=1}^{M} \left(\frac{\partial S}{\partial A_m}\right)^2 \Delta A_m^2 + \sum_{n=1}^{N} \left(\frac{\partial S}{\partial B_n}\right)^2 \Delta B_n^2}. \tag{4.11}$$

The systematic error is estimated as:

$$\Delta u_s \sim 6\%. \tag{4.12}$$

from uncertainties in the solid angle, the beam charge integration, the target thickness, etc.

The differential cross section uncertainty can be found easily:

$$\frac{\Delta\sigma}{\sigma} = \sqrt{\Delta u_0^2 + \Delta u_s^2}. \tag{4.13}$$

for unpolarized case, where,

$$\Delta u_0 \equiv \frac{1}{\sqrt{N}}. \tag{4.14}$$

The polarized scattering has the uncertainties for σ and A_y as:

$$(\frac{\Delta\sigma}{\sigma})_{up,down} = \sqrt{\sum_{i=u,d}\left[(\frac{\partial\sigma}{\partial P_i})^2(\Delta P_i)^2 + (\frac{\partial\sigma}{\partial\sigma_i})^2(\Delta\sigma_i)^2\right]}_{up,down}. \tag{4.15}$$

$$(\frac{\Delta A_y}{A_y})_{up,down} = \sqrt{\sum_{i=u,d}\left[(\frac{\partial A_y}{\partial P_i})^2(\Delta P_i)^2 + (\frac{\partial A_y}{\partial\sigma_i})^2(\Delta\sigma_i)^2\right]}_{up,down}. \tag{4.16}$$

CHAPTER 5

RESULTS AND DISCUSSIONS

5.1 General

The invariant differential cross sections $\left(\frac{d\sigma}{dt}\right)$ and the center of mass(CM) differential cross sections $\left(\frac{d\sigma}{d\Omega}\right)_{CM}$ of ^{28}Si at 200, 250 and 400 MeV are shown in figures 5.1 and 5.2. From figure 5.2, one sees that for higher beam energy, one gets lower $\left(\frac{d\sigma}{d\Omega}\right)_{CM}$ for a specific center of mass angle. The invariant differential cross sections is almost a constant with respect to the momentum transfer q. This is because $\left(\frac{d\sigma}{dt}\right)$ is a Lorentz invariant as is the electromagnetic interaction.

The beam polarizations are shown in figures 5.3, 5.4 and 5.5. The beam polarizatons varies between 70% and 85% in Proton Hall BL4. The analyzing power data are discussed later together with the optical model result.

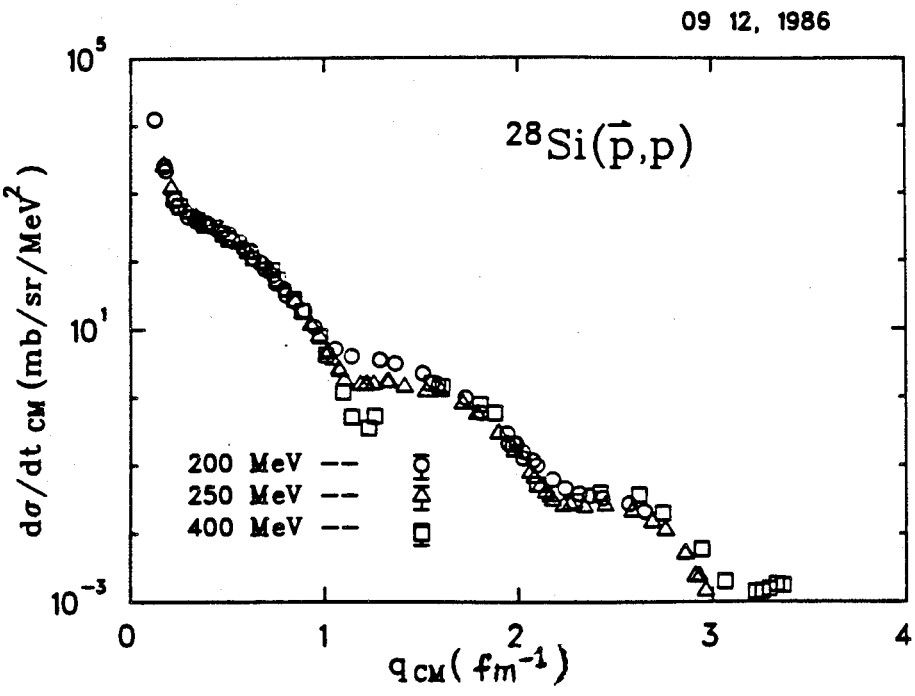

Figure 5.1 The invariant differential cross sections of ^{28}Si.

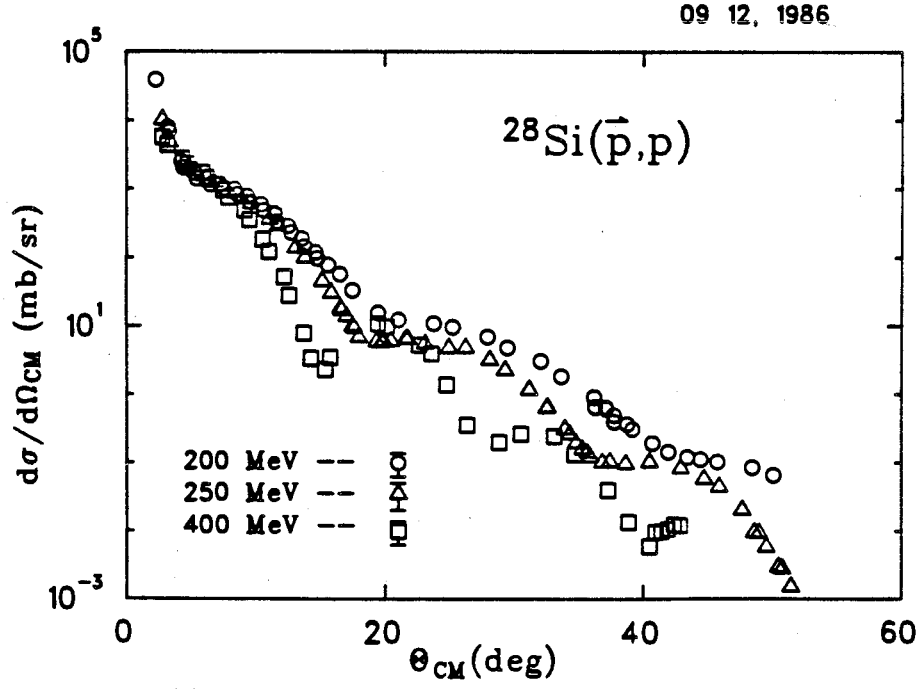

Figure 5.2 The center of mass differential cross sections of ^{28}Si.

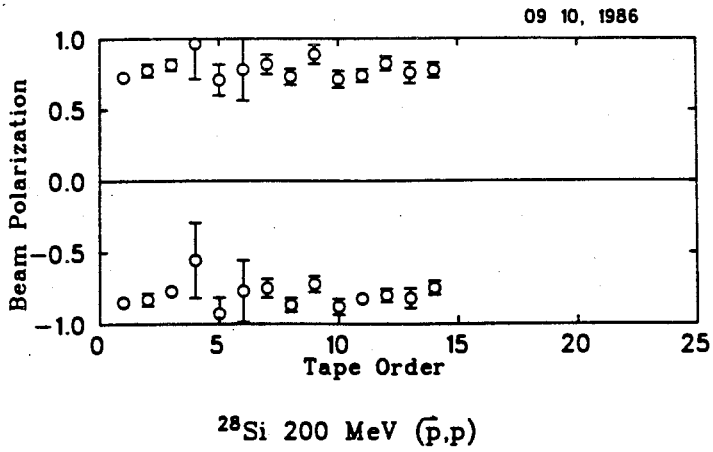

Figure 5.3 Incoming beam polarization data for ^{28}Si at 200 MeV.

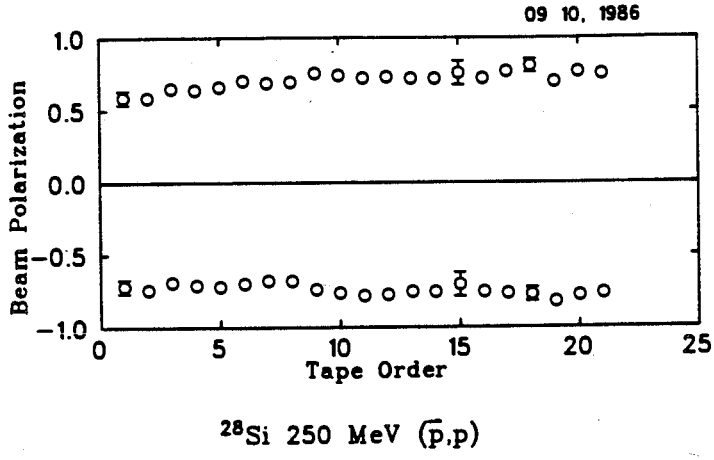

Figure 5.4 Incoming beam polarization data for ^{28}Si at 250 MeV.

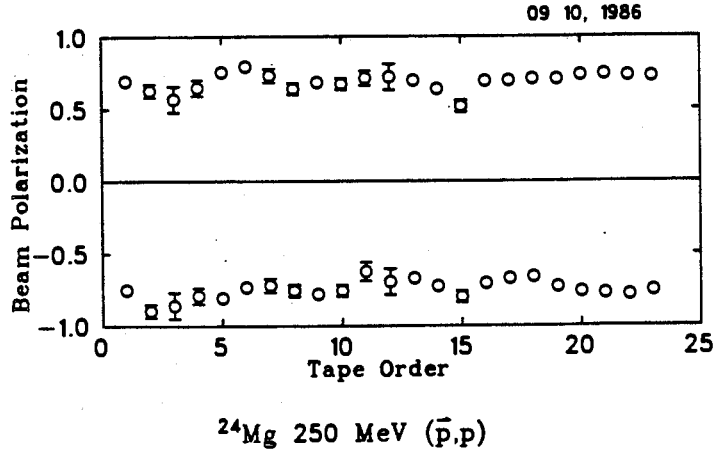

Figure 5.5 Incoming beam polarization data for ^{24}Mg at 250 MeV.

5.2 POM and RPOM

The RPOM uses the scalar and vector potentials (with Wood-Saxon form): V_V, W_V, V_S, W_S. The results were obtained from fitting the data with the code RUNT. Figures 5.6, 5.7, 5.8 and 5.9 show the scalar and vector potentials from fitting to ^{28}Si and ^{24}Mg. Note that these potentials are not the effective nuclear potentials. Rather, the combination of them forms the effective potentials.

The POM on the other hand gives the central and spin-orbit potentials directly: V_C, W_C, V_{SO} and W_{SO}. These potentials can be compared with the effective potentials from Dirac calculations. The results are shown in figures 5.10, 5.11, 5.12 and 5.13 where the RPOM optical potentials correspond to the solid lines and the POM potentials to the dotted lines. Table 5.1 is the comparison of the optical model fits with the Wood-Saxon potential parameters. Note that the experiment by Olmer applies the code SNOOPY which is slightly different from RUNT.

The RPOM effective potentials shown in the figures 5.10 to 5.13 (solid line) always exhibit a deformation at small radii. This shape looks like the bottom of a wine bottle with a rise at the center of the bottom face of the wine bottle. This unconventional shape is therefore refered to as the wine-bottle shape. Potentials of this shape can not be obtained in the POM. Other than this shape, there is not much difference in the radius or the diffuseness from these two models. It is also found that the fitting results are not unique. Two different fits for each data set are shown in table 5.1. Both fits reproduce the data nicely.

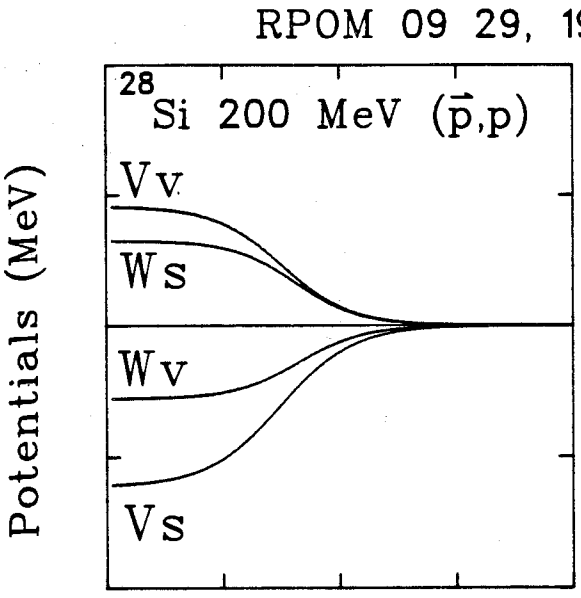

Figure 5.6 RPOM vector and scalar potentials for ^{28}Si at 200 MeV.

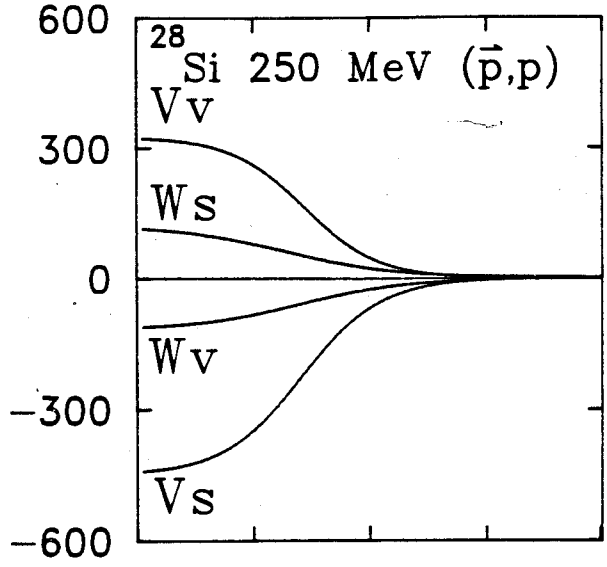

Figure 5.7 RPOM vector and scalar potentials for ^{28}Si at 250 MeV.

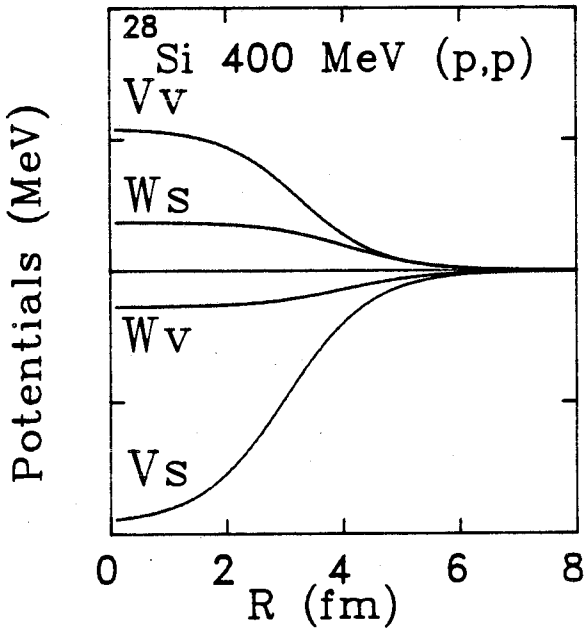

Figure 5.8 RPOM vector and scalar potentials for ^{28}Si at 400 MeV.

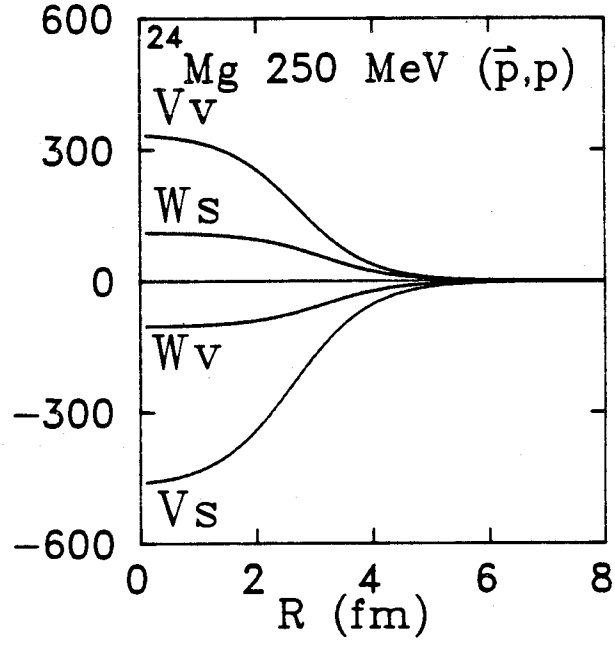

Figure 5.9 RPOM vector and scalar potentials for ^{24}Mg at 250 MeV.

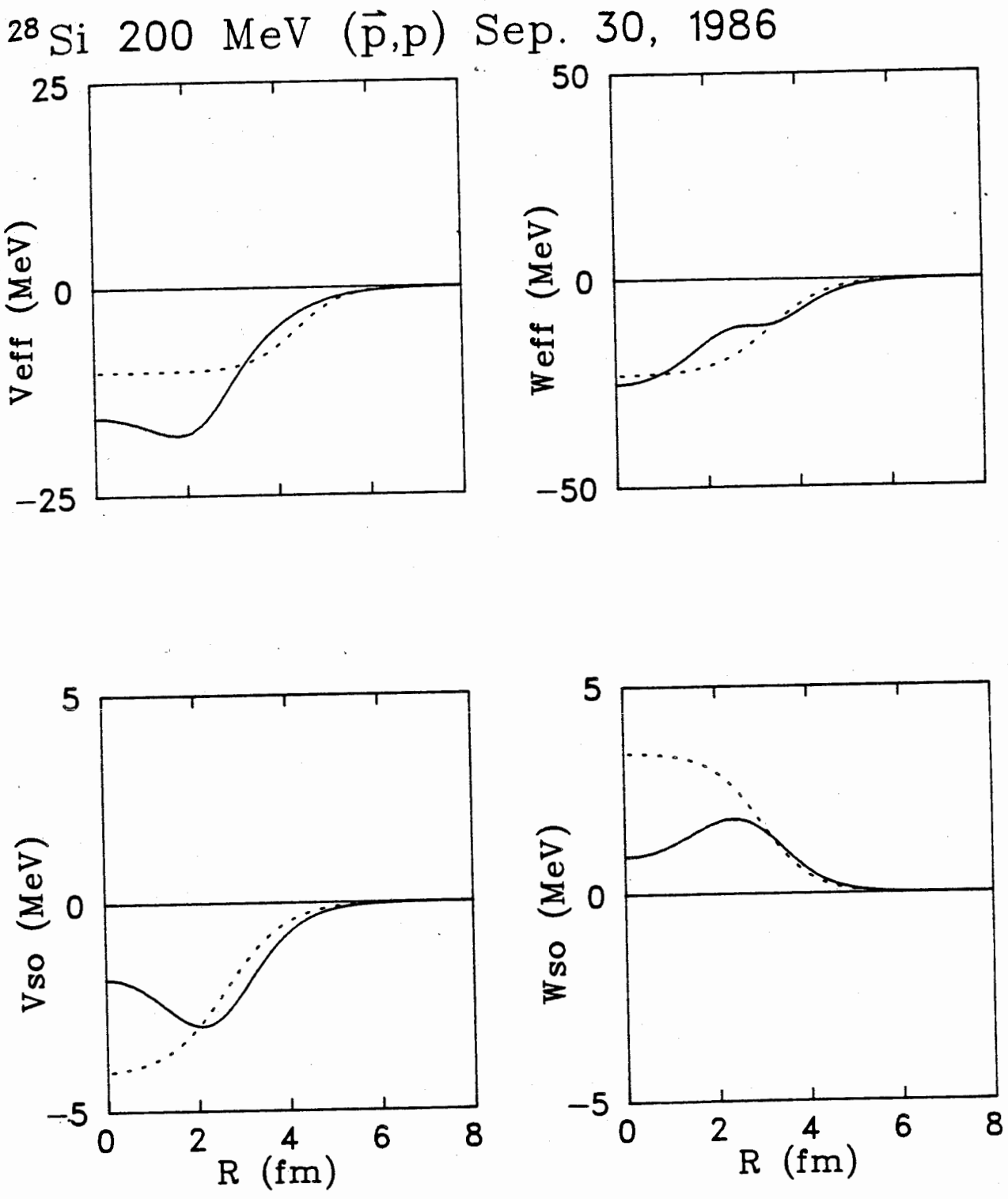

Figure 5.10 POM(dotted line) and RPOM optical potentials for ^{28}Si at 200 MeV.

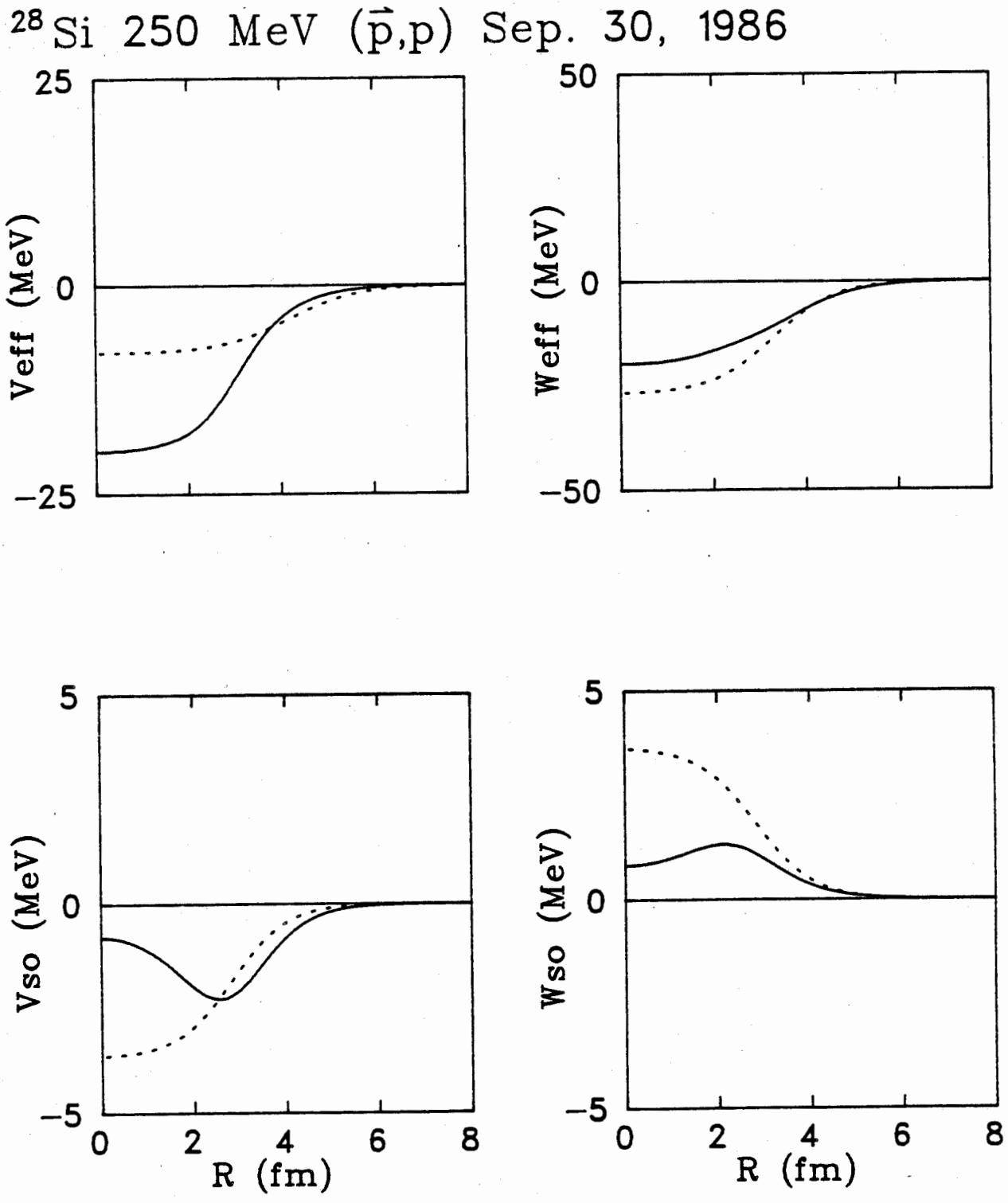

Figure 5.11 POM(dotted line) and RPOM optical potentials for ^{28}Si at 250 MeV.

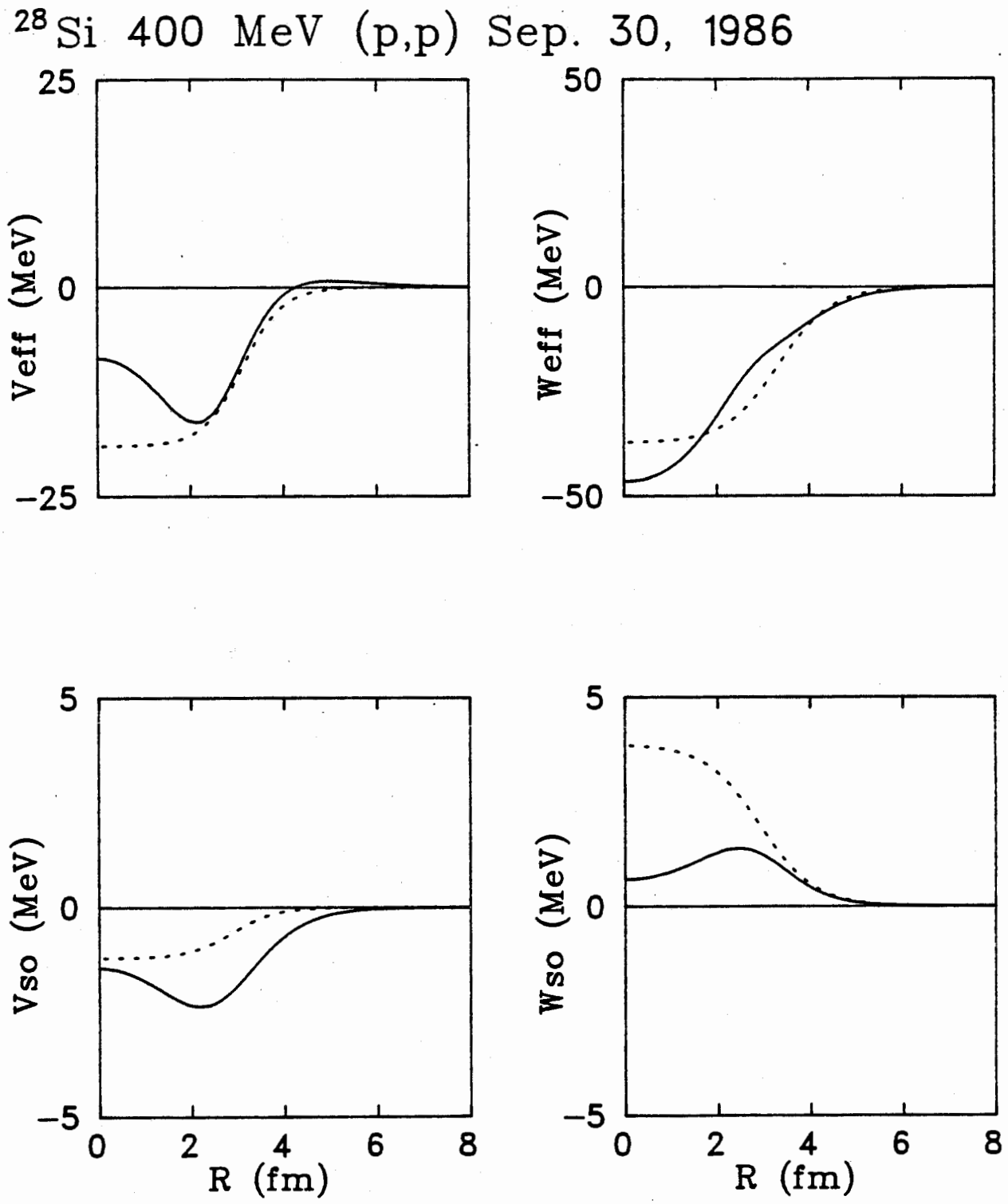

Figure 5.12 POM(dotted line) and RPOM optical potentials for ^{28}Si at 400 MeV.

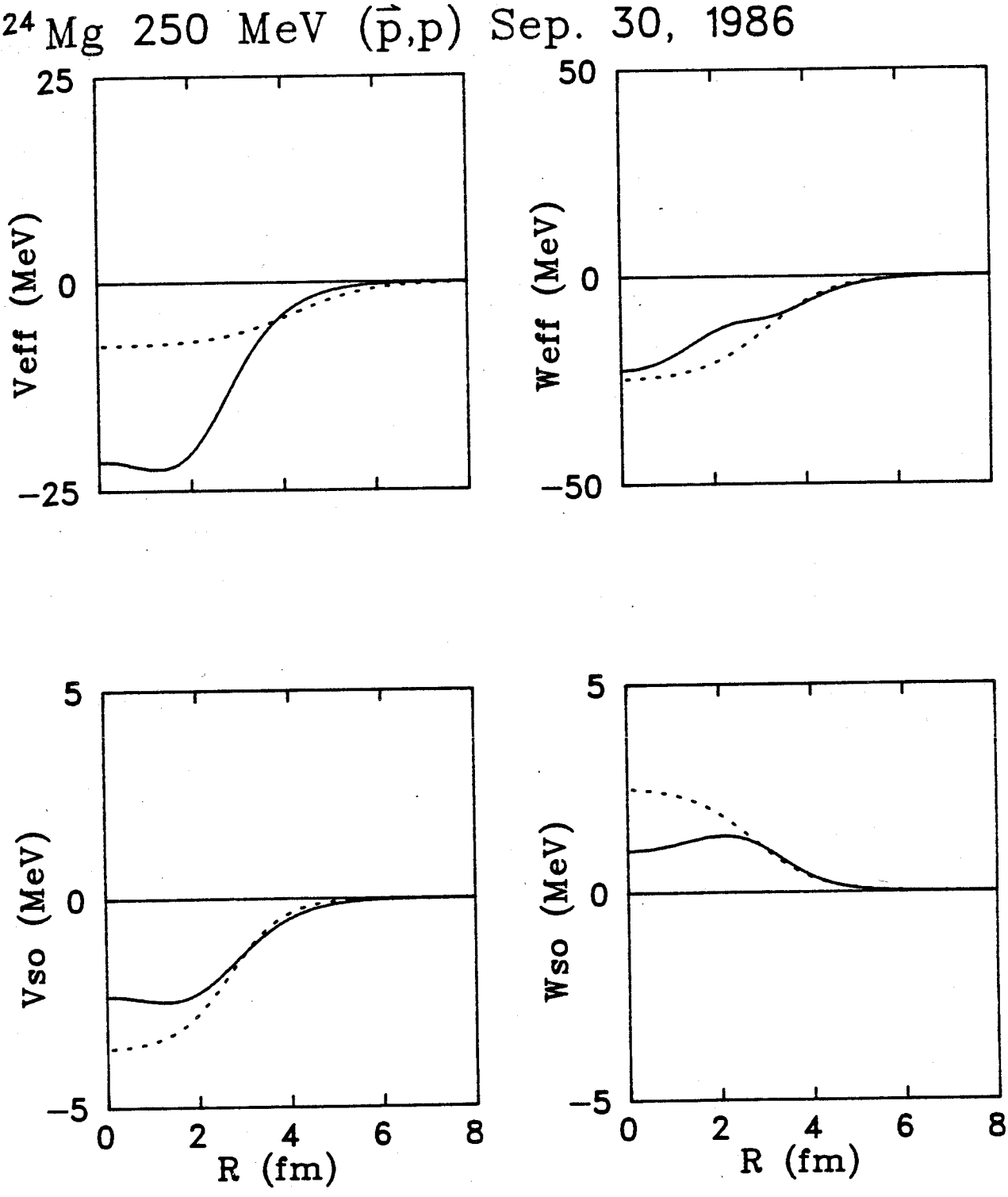

Figure 5.13 POM(dotted line) and RPOM optical potentials for ^{24}Mg at 250 MeV.

^{28}Si POM												
Ep	V_{RC}	r_{RC}	a_{RC}	W_{IC}	r_{IC}	a_{IC}	V_{RSO}	r_{RSO}	a_{RSO}	W_{ISO}	r_{ISO}	a_{ISO}
*80	29.30	1.20	0.72	5.00	1.52	0.35	4.42	1.03	0.64	-0.70	0.92	0.59
*100	25.00	1.23	0.72	5.50	1.49	0.44	4.10	1.01	0.64	-1.10	0.92	0.59
*134	19.30	1.27	0.72	6.90	1.36	0.66	3.53	0.96	0.64	-1.80	0.94	0.59
*180	13.70	1.30	0.72	13.10	1.13	0.72	2.80	0.94	0.64	-2.70	0.95	0.59
^{1}200	10.10	1.45	0.50	23.09	1.12	0.60	4.14	0.86	0.66	-3.42	0.98	0.55
^{2}200	11.19	1.41	0.69	29.09	0.99	0.70	4.18	0.89	0.63	-3.02	0.99	0.79
250	8.08	1.37	0.74	26.85	1.09	0.66	3.67	0.93	0.60	-3.66	0.93	0.62
^{1}400	19.00	1.03	0.43	37.31	1.10	0.58	1.21	0.94	0.47	-3.88	0.96	0.59
^{2}400	18.61	1.02	0.46	42.46	1.08	0.56	1.19	0.85	0.45	-3.90	0.95	0.56
+135	19.40	1.27	0.75	5.63	1.41	0.64	2.92	0.97	0.59	-1.49	0.97	0.59
+333	30.90	0.98	0.49	20.10	1.14	0.66	0.23	1.06	0.75	-2.14	1.06	0.75
$^{+}_{2}$333	33.20	0.89	0.95	20.90	1.13	0.51	0.60	0.99	0.57	-2.26	0.99	0.57
+498	6.39	1.22	0.44	33.00	1.09	0.54	1.28	0.92	0.62	-3.44	0.92	0.62
+800	-6.24	0.94	0.34	74.00	0.97	0.58	0.69	1.07	0.68	0.22	1.07	0.68
^{s}155	13.96	1.34	0.50	58.56	0.78	0.78	4.10	0.42	0.96	-5.94	0.78	0.59

(*–Ol84, +–Hi84, s–Sa83a)

^{24}Mg POM												
Ep	V_{RC}	r_{RC}	a_{RC}	W_{IC}	r_{IC}	a_{IC}	V_{RSO}	r_{RSO}	a_{RSO}	W_{ISO}	r_{ISO}	a_{ISO}
^{1}250	7.61	1.46	0.83	25.04	1.09	0.72	3.63	0.93	0.59	-2.56	0.94	0.70
^{2}250	7.08	1.39	0.75	24.10	1.08	0.80	3.95	0.95	0.60	-1.30	0.97	0.78
^{s}155	12.29	1.39	0.57	22.31	0.98	0.81	4.19	0.90	0.71	-1.65	0.96	0.57

(s–Sa83a)

^{28}Si RPOM												
Ep	V_{RV}	r_{RV}	a_{RV}	W_{IV}	r_{IV}	a_{IV}	V_{RS}	r_{RS}	a_{RS}	W_{IS}	r_{IS}	a_{IS}
^{1}200	274.4	1.00	0.58	-167.3	1.09	0.56	-367.7	0.98	0.63	195.2	1.07	0.55
^{2}200	353.6	0.90	0.68	-165.8	1.08	0.59	-483.2	0.88	0.69	222.6	1.01	0.59
^{1}250	326.1	0.95	0.63	-116.4	0.92	0.89	-448.9	0.93	0.67	125.4	0.84	0.99
^{2}250	289.1	0.99	0.65	-130.4	1.01	0.75	-421.7	0.97	0.65	185.2	0.91	0.76
^{1}400	326.1	1.08	0.68	-83.16	1.33	0.75	-577.7	1.00	0.73	111.9	1.34	0.70
^{2}400	301.6	0.93	0.73	-140.6	1.06	0.62	-490.1	0.91	0.70	210.6	1.00	0.60

^{24}Mg RPOM												
Ep	V_{RV}	r_{RV}	a_{RV}	W_{IV}	r_{IV}	a_{IV}	V_{RS}	r_{RS}	a_{RS}	W_{IS}	r_{IS}	a_{IS}
^{1}250	337.7	0.94	0.63	-103.9	1.10	0.63	-471.5	0.91	0.66	111.9	1.08	0.63
^{2}250	290.4	0.84	0.82	-144.7	1.05	0.67	-416.5	0.83	0.81	193.7	0.99	0.65

Table 5.1 Optical model parameters with comparison

The calculation of observables from the POM fit are plotted in figures 5.16, 5.17, 5.20, 5.21, 5.23, 5.26 and 5.27. These observables are both the differential cross sections and analyzing powers. It can be seen immediately that the fitting results give very good agreement with the data. Figures 5.14, 5.15, 5.18, 5.19, 5.22, 5.24 and 5.25 are the results from the RPOM fit. It is not obvious which one of the calculations is better at first sight. However, the very forward angle fitting results agree with the data better in the RPOM than in the POM at all angles. Also, around 18 degrees, the first minimum from ^{28}Si at 250 MeV of the POM is lower than expected, while the RPOM does not have this problem. One should compare the results of both model carefully from other figures shown in the paper. The Dirac POM is probably a better description when the beam energy is higher. It also means that the optical potentials using wine-bottle shape which is interpreted as the meson exchange process in the nucleon interaction(see section 2.4) is a better model than the smooth Wood-Saxon shape.

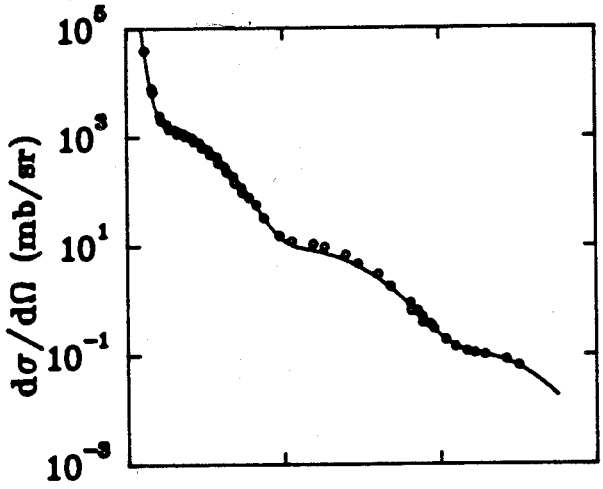

Figure 5.14 RPOM calculation of $\frac{d\sigma}{d\Omega}$ for ^{28}Si at 200 MeV.

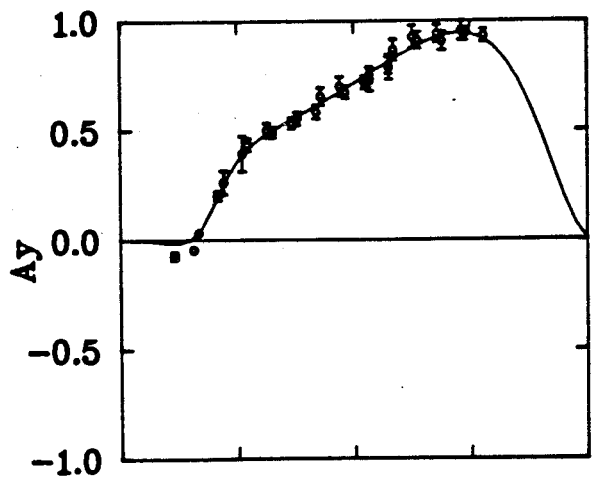

Figure 5.15 RPOM calculation of Ay for ^{28}Si at 200 MeV.

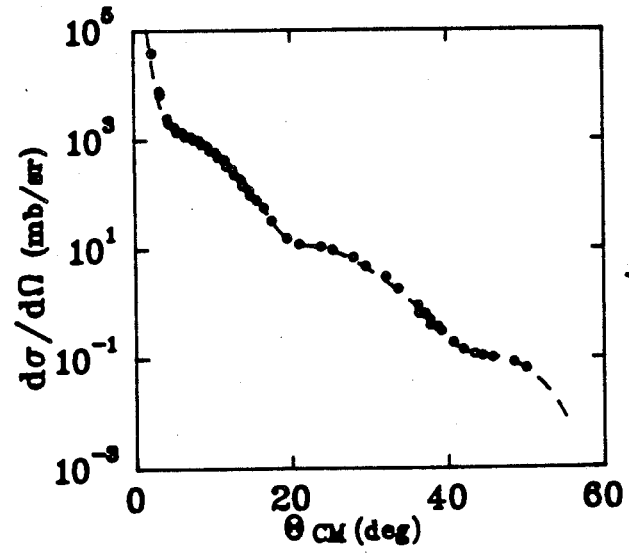

Figure 5.16 POM calculation of $\frac{d\sigma}{d\Omega}$ for ^{28}Si at 200 MeV.

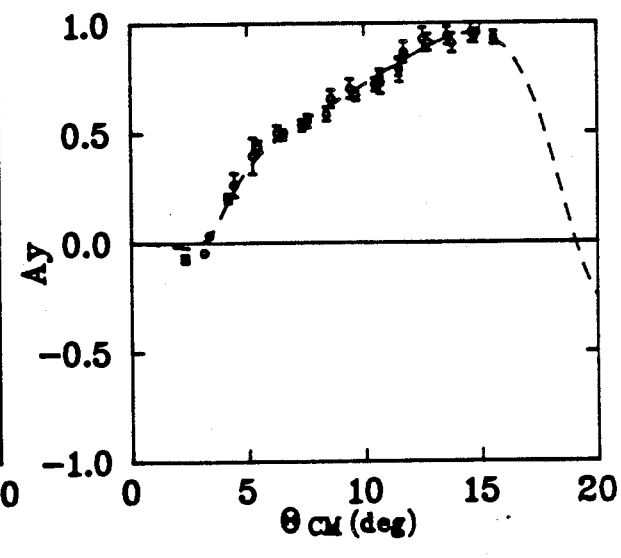

Figure 5.17 POM calculation of Ay for ^{28}Si at 200 MeV.

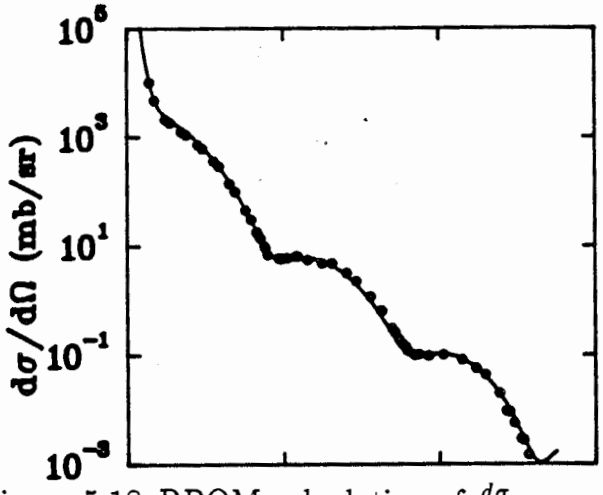

Figure 5.18 RPOM calculation of $\frac{d\sigma}{d\Omega}$ for ^{28}Si at 250 MeV.

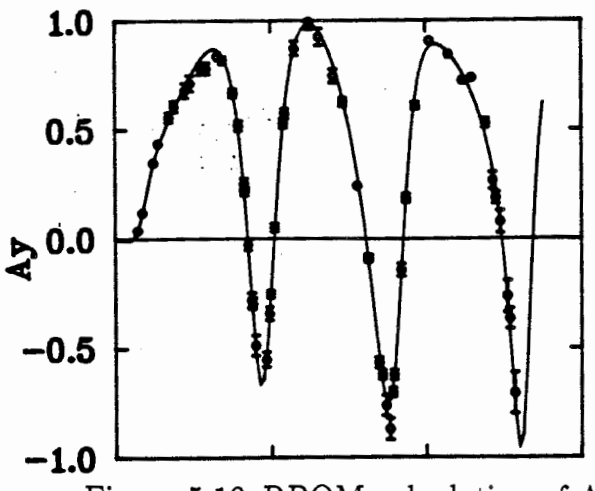

Figure 5.19 RPOM calculation of Ay for ^{28}Si at 250 MeV.

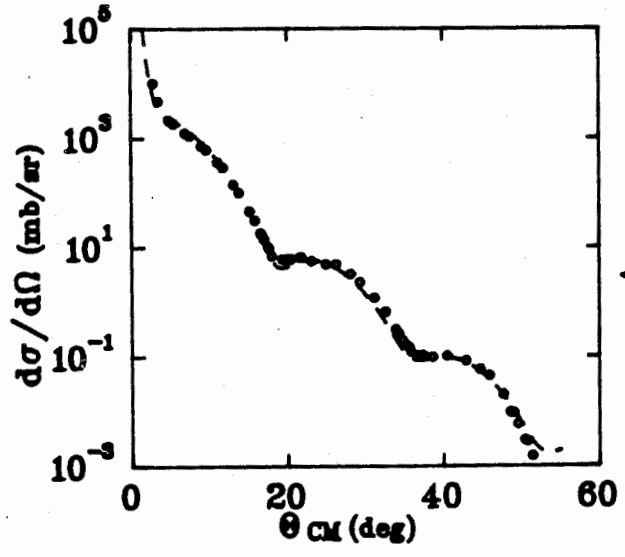

Figure 5.20 POM calculation of $\frac{d\sigma}{d\Omega}$ for ^{28}Si at 250 MeV.

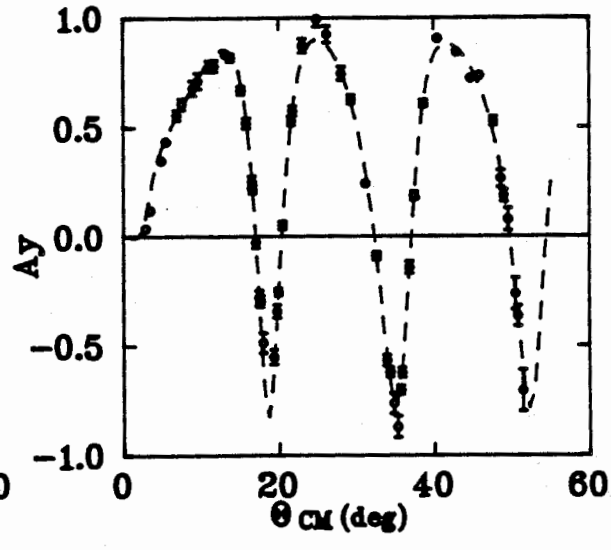

Figure 5.21 POM calculation of Ay for ^{28}Si at 250 MeV.

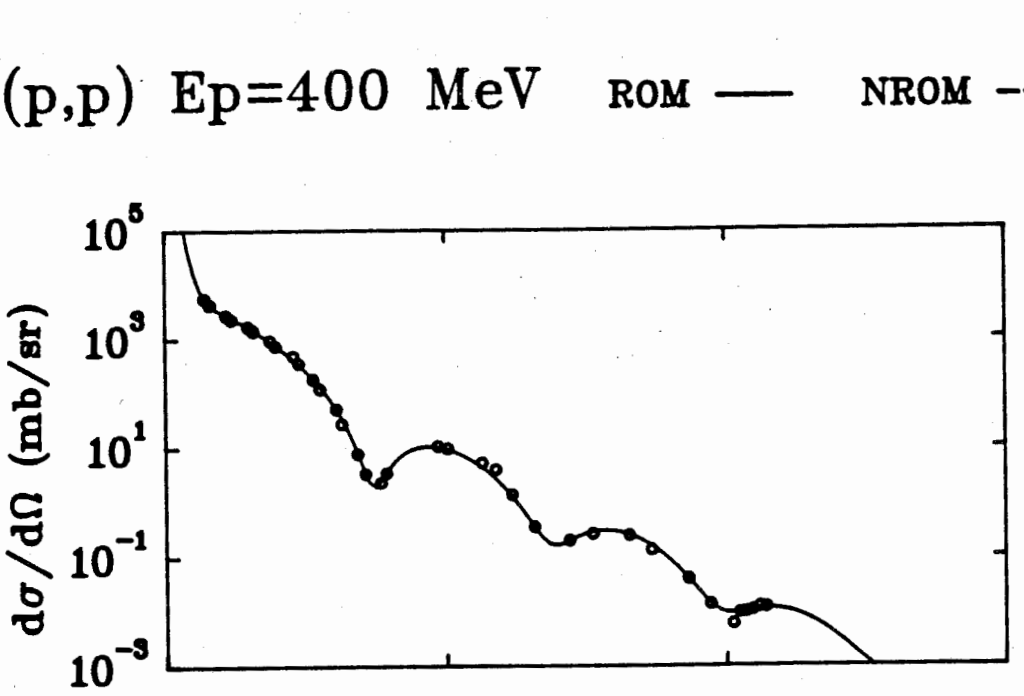

Figure 5.22 RPOM calculation of $\frac{d\sigma}{d\Omega}$ for ^{28}Si at 400 MeV.

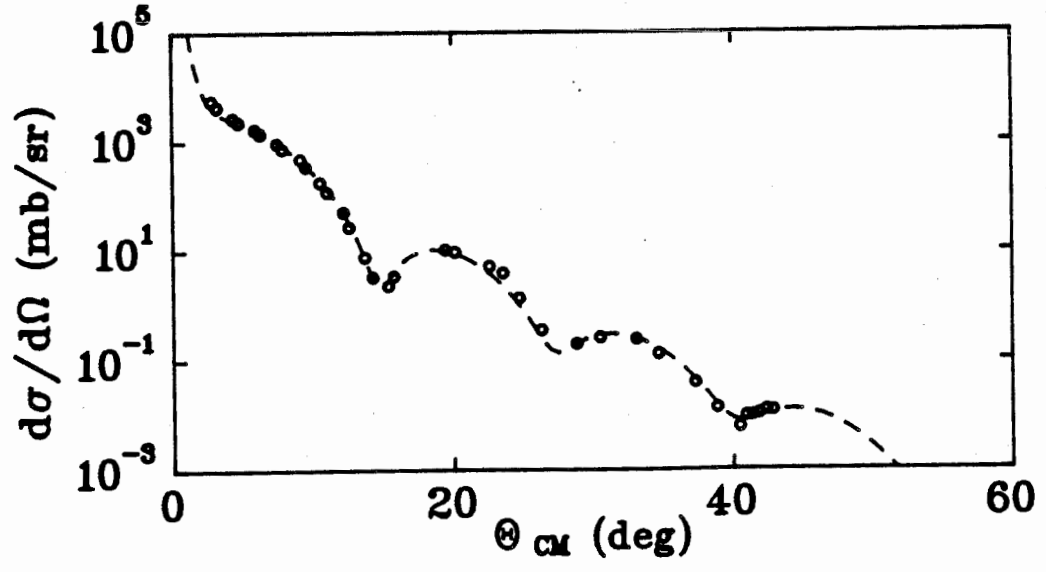

Figure 5.23 POM calculation of $\frac{d\sigma}{d\Omega}$ for ^{28}Si at 400 MeV.

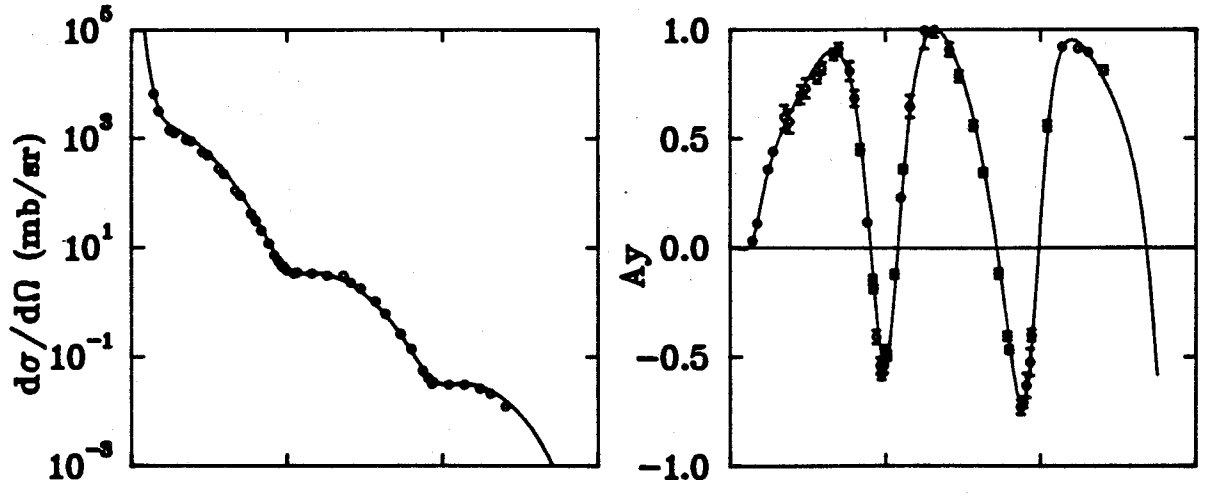

Figure 5.24 RPOM calculation of $\frac{d\sigma}{d\Omega}$ for ^{24}Mg at 250 MeV.

Figure 5.25 RPOM calculation of Ay for ^{24}Mg at 250 MeV.

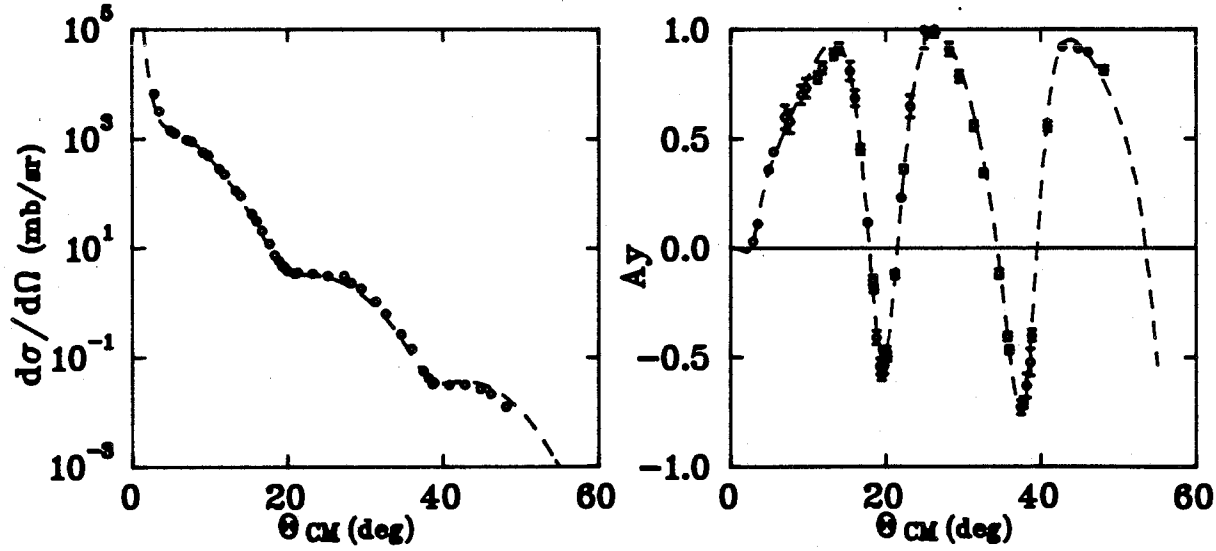

Figure 5.26 POM calculation of $\frac{d\sigma}{d\Omega}$ for ^{24}Mg at 250 MeV.

Figure 5.27 POM calculation of Ay for ^{24}Mg at 250 MeV.

5.3 DWPOM and RDWPOM

This section studies the inelastic collective states with spin transfer J and parity π of $J^\pi = 2^+$. In the DWBA with phenomenological Wood-Saxon potentials, the potential parameters are taken from ground state fit since the elastic process dominates most in the reactions. The observables obtained from the experiment are both the differential cross sections and analyzing powers for the 2^+ state. The code used here is PLTRK(or ECIS79). PLTRK calculates σ and A_y in both the DWPOM and the RDWPOM, while ECIS79 only uses the Schrödinger DWPOM.

Just like what happens in the ground state, the 2^+ data also have higher cross sections for the lower beam energies as expected.

The 2^+ results from the experiment and distorted wave calculations are shown in figures 5.28, 5.29, 5.30 and 5.31. The solid line is the prediction from RDWPOM and the dashed-dotted curve is from Schrödinger DWPOM with equal deformation length$-\delta$ ($\beta_{RC}R_{RC} = \beta_{IC}R_{IC} = \beta_{RSO}R_{RSO} = \beta_{ISO}R_{ISO} = \beta_C R_C$). The dotted curve is for DWPOM but with equal$-\beta$ value. The equal$-\delta$ method is found better than the equal$-\beta$ one.

The calculation is found to be in good agreement with the TRIUMF 250 MeV data. For ^{28}Si at 400 MeV, the fit to the elastic data is not well transfered to the 2^+. This could be due the lack of the analyzing powers in the fitting process. Table 5.3 gives the deformation lengths result and the result from other experiments(Bl79, Ch72, Du78, Ha81, Ha84, Ka85, Le79, Mi74, Re71, Re72, Ta65 and Ya76). It is found that the deformation length is more or less equal with up to 40% deviations from this experiment at different energies. This implies that the collective model with a certain deformation length is suitable for describing the low-lying states. In order to understand the distorted

wave models, more data from 300 to 500 MeV with both cross sections and analyzing powers(and spin rotation parameters Q, if possible) are suggested. One can also see that the minima of the cross section and analyzing power calculations are different from one model to the other. From the figures, it is seen that the minima of RDWPOM are at more forward angles than that of the DWPOM.

One can also see that for different nucleus, the deformation is also different by just comparing the 250 MeV data for ^{28}Si and ^{24}Mg. The δ_i value of ^{24}Mg is much larger that that of ^{28}Si. That is to say, δ_i is target dependent. If one takes the βR value from the electromagnetic result(Ch72) into DWPOM(equal deformation length) method, one needs to take **$\sim$25% reduction on the cross section of the 2^+ state for ^{28}Si and $\sim$35% for ^{24}Mg**(Latter in microscopic study, a reduction is also found).

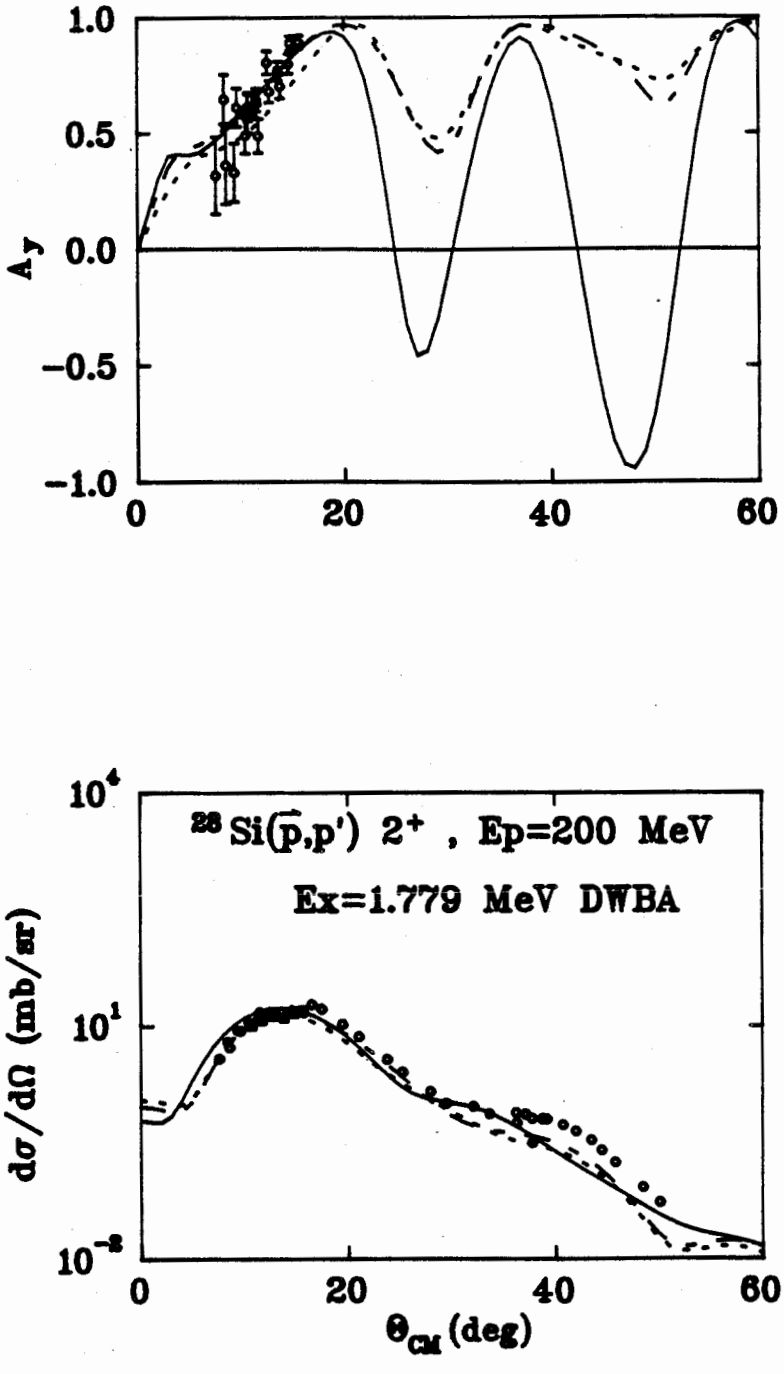

Figure 5.28 DWPOM–equal β(dotted line), DWPOM–equal δ(dashed-dotted line) and RDWPOM(solid line) calculations for ^{28}Si at 200 MeV.

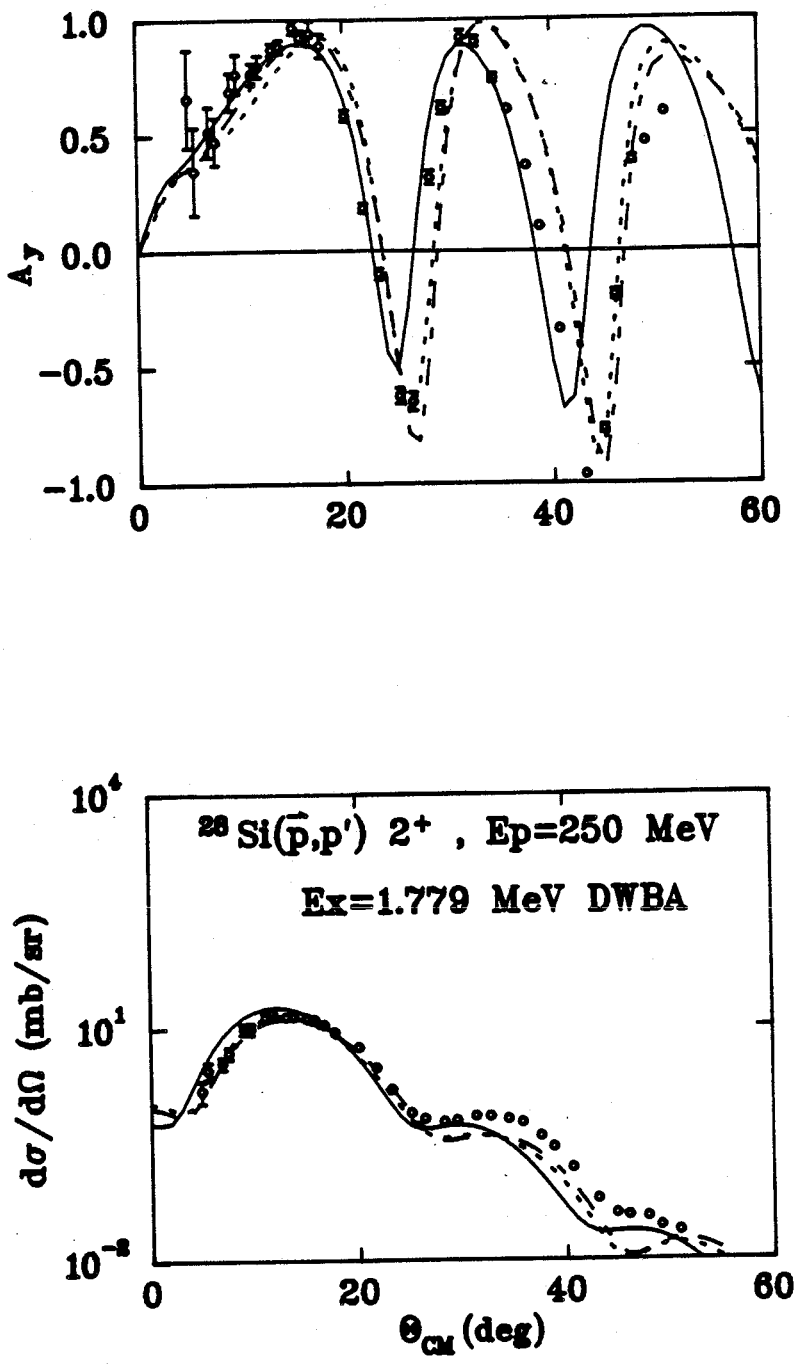

Figure 5.29 DWPOM–equal β(dotted line), DWPOM–equal δ(dashed-dotted line) and RDWPOM(solid line) calculations for ^{28}Si at 250 MeV.

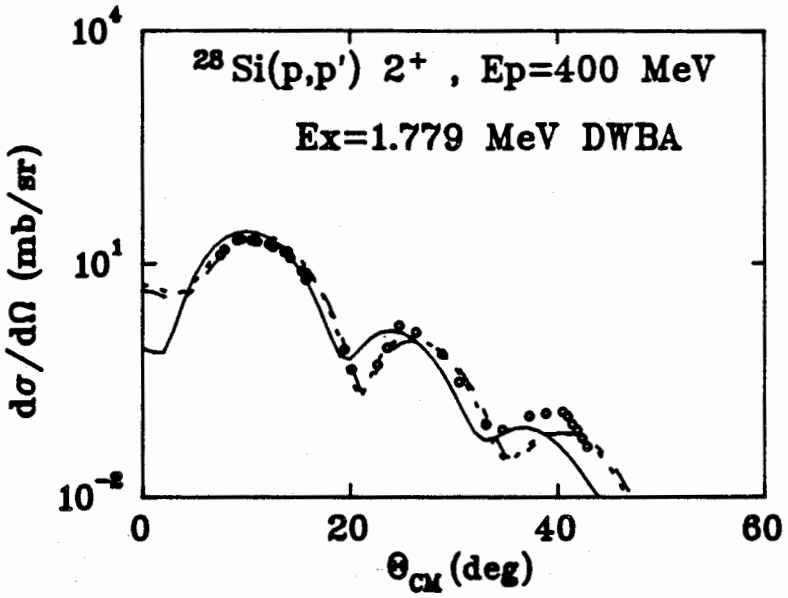

Figure 5.30 DWPOM–equal β(dotted line), DWPOM–equal δ(dashed-dotted line) and RDWPOM(solid line) calculations for ^{28}Si at 400 MeV.

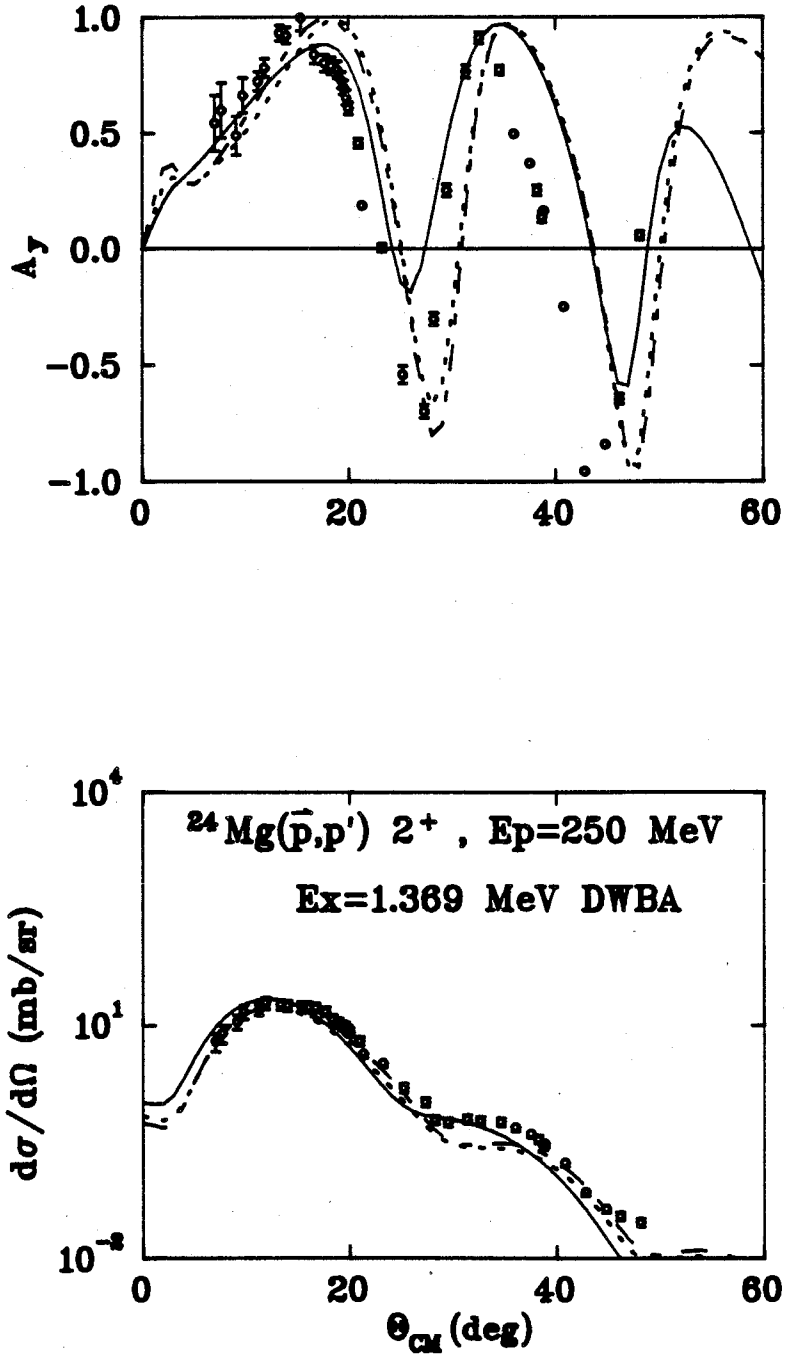

Figure 5.31 DWPOM–equal β(dotted line), DWPOM–equal δ(dashed-dotted line) and RDWPOM(solid line) calculations for ^{24}Mg at 250 MeV.

Comparisons of Deformation lengths			
Ep(MeV),Target	Model	$\beta R(2^+)$	Reference
200, ^{28}Si	DWPOM(δ)	1.32	Present
200, ^{28}Si	DWPOM(β)	1.68	Present
200, ^{28}Si	RDWPOM	1.25	Present
250, ^{28}Si	DWPOM(δ)	1.24	Present
250, ^{28}Si	DWPOM(β)	1.63	Present
250, ^{28}Si	RDWPOM	1.32	Present
400, ^{28}Si	DWPOM(δ)	1.31	Present
400, ^{28}Si	DWPOM(β)	1.36	Present
400, ^{28}Si	RDWPOM	1.36	Present
*, ^{28}Si	(e,e')	1.468*	Ch72
65, ^{28}Si	(p,p')	1.17	Ka85
25–40, ^{28}Si	(p,p')	1.31	Le79
56, ^{28}Si	(d,d')	1.18	Ha81
104, ^{28}Si	(α,α')	1.25	Re71,72
10–15, ^{28}Si	(n,n')	1.47	Ha84
45–63, ^{28}Si	(^{16}O,^{16}O')	1.35	Du78
250, ^{24}Mg	DWPOM(δ)	1.68	Present
250, ^{24}Mg	DWPOM(β)	2.16	Present
250, ^{24}Mg	RDWPOM	1.55	Present
*, ^{24}Mg	(e,e')	2.091*	Ch72
65, ^{24}Mg	(p,p')	1.58	Ka85
800, ^{24}Mg	(p,p')	1.61	Bl79
56, ^{24}Mg	(d,d')	1.44	Ha81
70, ^{24}Mg	(α,α')	1.84	Ya76
104, ^{24}Mg	(α,α')	1.36	Re71,72
28.5, ^{24}Mg	(α,α')	1.72	Ta65
10–15, ^{24}Mg	(n,n')	1.76	Ha84
25–64, ^{24}Mg	(^{16}O,^{16}O')	1.56	Mi74

Table 5.2 Deformation lengths from (p,p') and comparisons. (δ) means same deformation length is applied and, (β), same deformation parameter is used.

5.4 LF and DD

A microscopic DWIA(or IA) Love–Franey t-matrix calculation was carried out. These results are denoted with LF. The DWMM Hamburg code uses the PARIS83 force and a density-dependent G-matrix(instead of t-matrix), and the results are denoted with DD. Both approximations can be calculated by using the optical model program DW83 with associated forces, optical model potentials and shell model transition densities which are consistent with the electromagnetic data. The matter density is taken from the electron 3-parameter Fermi model(Ja74) and the size of the proton is then unfolded. The point density is thus put into the potential calculations for both the t-matrix and the G-matrix. The calculated potential is then applied in the calculation of observables. In LF, the force used is LF85(see Fr85). In DD, the PARIS83 force(Ri84) is applied. Both forces are energy-dependent. LF is tabulated up to 1 GeV while DD is valid only below approximately 400 MeV. The 3-parameter Fermi density with size of the proton unfolded has the value listed in Table 5.3.

The shell model transition density and isoscalar effective charge are taken from a global fit to electromagnetic data in the sd–shell(see Br83 and Br86):

The Harmonic oscillator length parameters $b_f^{2^+}$(fm).

^{28}Si : 1.80

^{24}Mg : 1.76

Effective charge normalization $e_p + e_n$(2^+ only, En78):

^{28}Si : 1.78 (1.71)

^{24}Mg : 2.09 (2.00)

Target	Radius(fm)	a(fm)	w(fm)
^{28}Si	3.1970	0.536	-.1950
^{24}Mg	3.0062	0.606	-.1748

Table 5.3 Three parameter Fermi densities from (e,e′) with proton size unfolded for ^{28}Si and ^{24}Mg.

A_{target}	Ex	5–5	5–1	5–3	1–5	1–3	3–5	3–1	3–3
24	1.369	−.6176	−.3232	−.3197	−.4255	−.1523	.3155	.1473	−.0643
28	1.779	−.2986	−.4066	−.3038	−.5949	−.0862	.3835	.1532	−.1714

Table 5.4 0^+ to 2^+ one-body transition density matrix elements from the shell model of Brown and Wildenthal. 3-1 means d3/2 particle– s1/2 hole etc.

Ep(MeV)	Target	Reduction factor	$\lvert\frac{t_{NA}}{t_{NN}}\rvert$
200	^{28}Si	0.85	0.924
250	^{28}Si	0.75	0.909
400	^{28}Si	0.75	0.871
250	^{24}Mg	0.75	0.909

Table 5.5 Potential reduction factors for microscopic calculations. Both DWIA and DWMM have the same values.

The one-body transition density matrix elements for 0^+ to 2^+(first) are listed in Table 5.4 with the particle-hole configurations in the order of $0d_{5/2}$, $1s_{1/2}$ and $0d_{3/2}$.

The force of LF is from LF85 based on the SP84 amplitude of Arndt. The DD force is taken from PARIS83. Figures 5.32 and 5.33 give the LF and DD optical potentials such that the energy dependent potentials can be compared easily. Note that in these pictures the optical potentials were not reduced.

From figures 5.34 to 5.53, we utilize them to demonstrate that in order to fit the data better, the reduction of the optical model potentials is necessary.

Table 5.5 lists the potential reduction values. Since the ^{28}Si data at 250 MeV has both observables, it is used to prove our reducing assumption on the potentials. Figure 5.34 shows that for the DD version, the ground state observables are improved significantly when one reduces the optical potentials (all the 4 parts of the potentials) by 25%. Finally, one takes the effective charge for 2^+ which is less than the average effective charge. For ^{28}Si, the effective charge for 2^+ is 1.71. The 2^+ calculation shows that **an extra ~28%(40%) reduction should be put in Si(Mg) cross sections prediction.** Note that this reduction does not apply on the ground state.

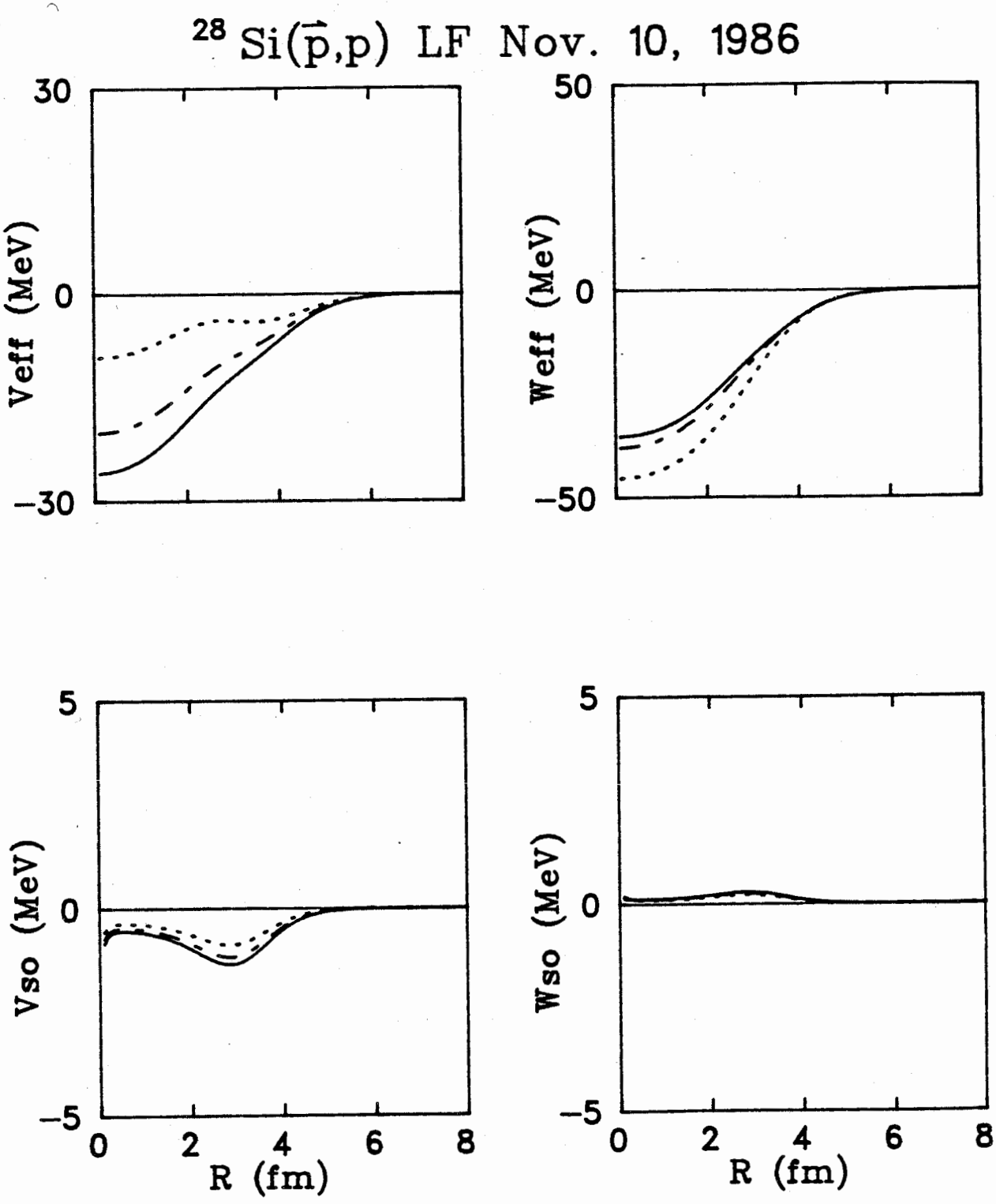

Figure 5.32 LF full strength optical potentials for ^{28}Si at 200 MeV(solid curve), 250 MeV(dashed curve) and 400 MeV(dotted curve).

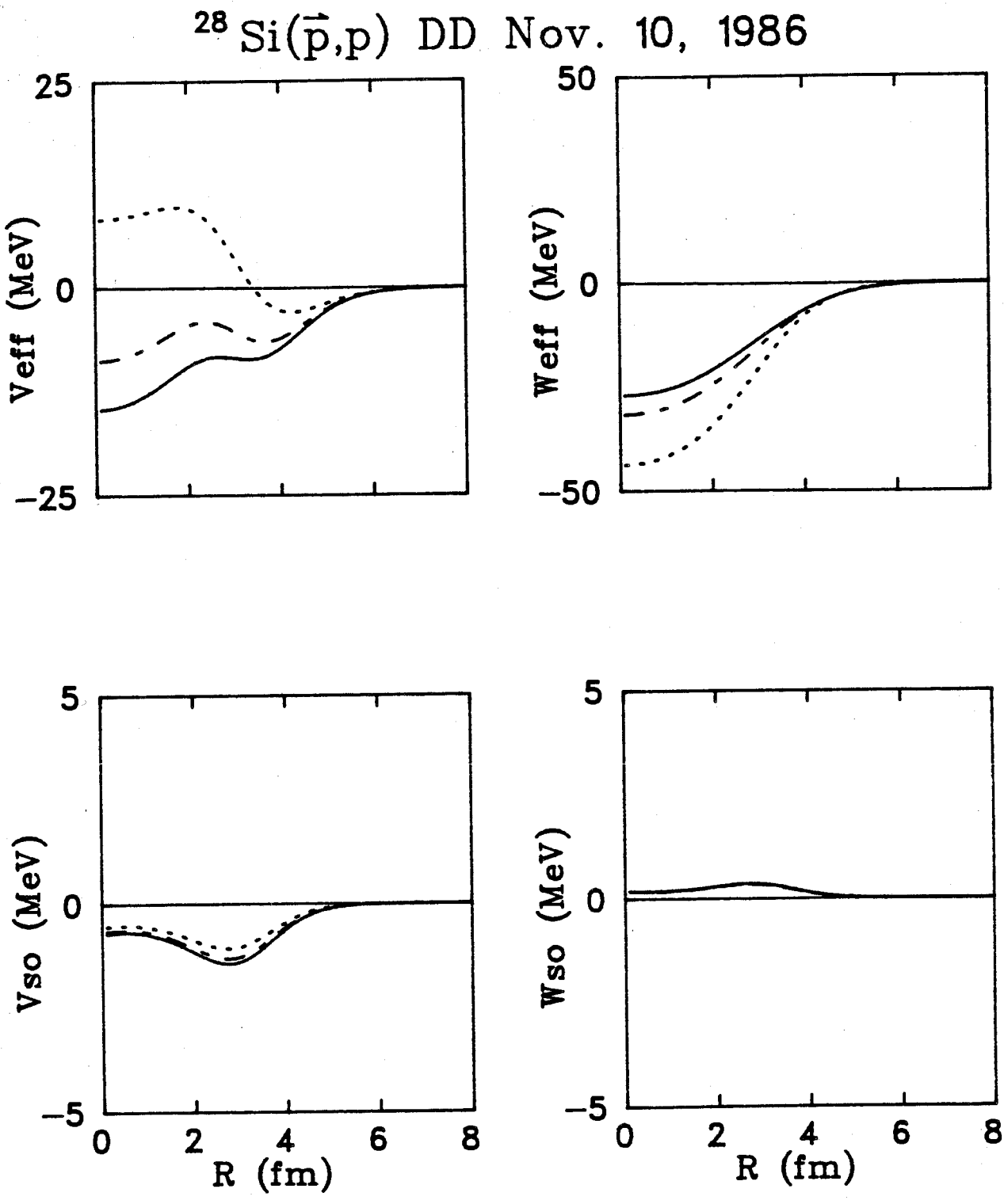

Figure 5.33 DD full strength optical potentials for ^{28}Si at 200 MeV(solid curve), 250 MeV(dashed curve) and 400 MeV(dotted curve).

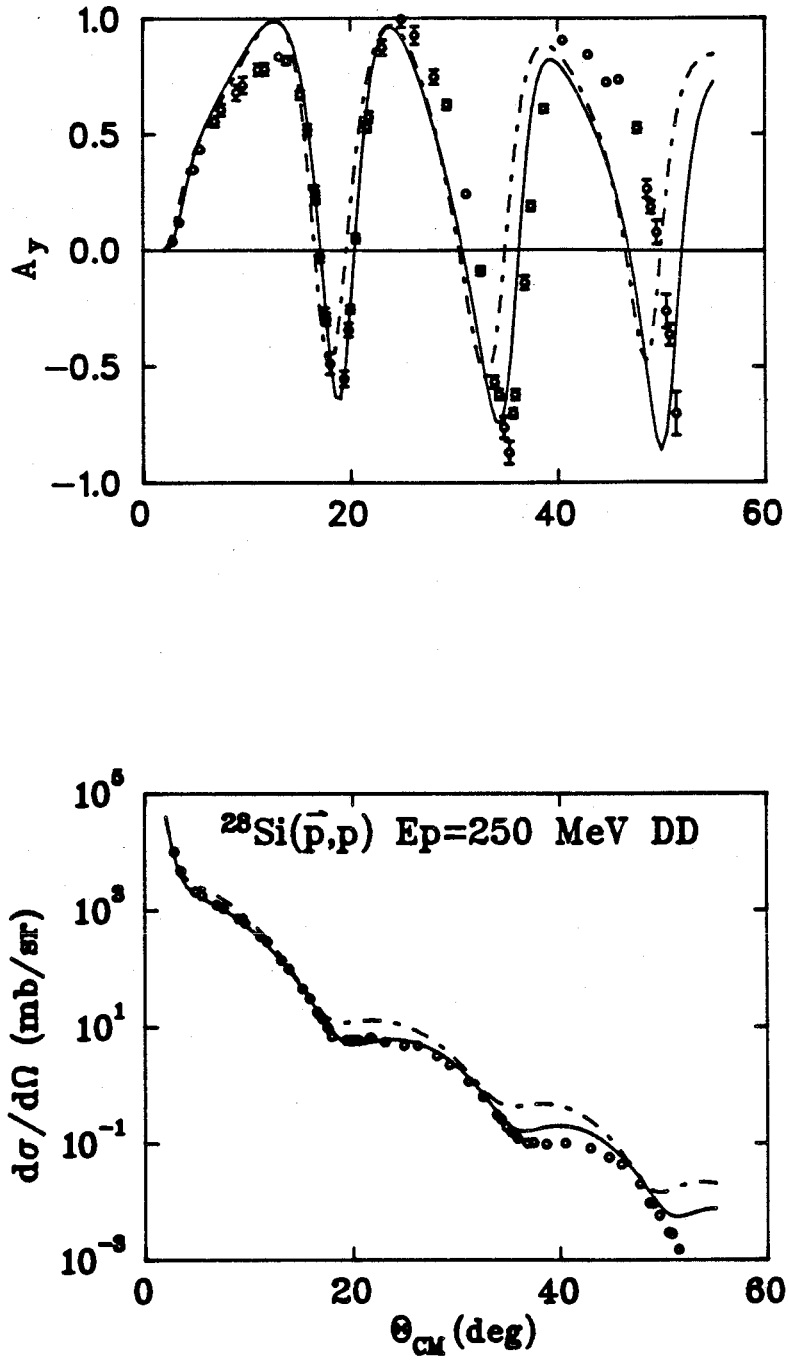

Figure 5.34 DD(dashed line) and DD with 75% optical potentials(solid line) for ^{28}Si 0^+ at 250 MeV.

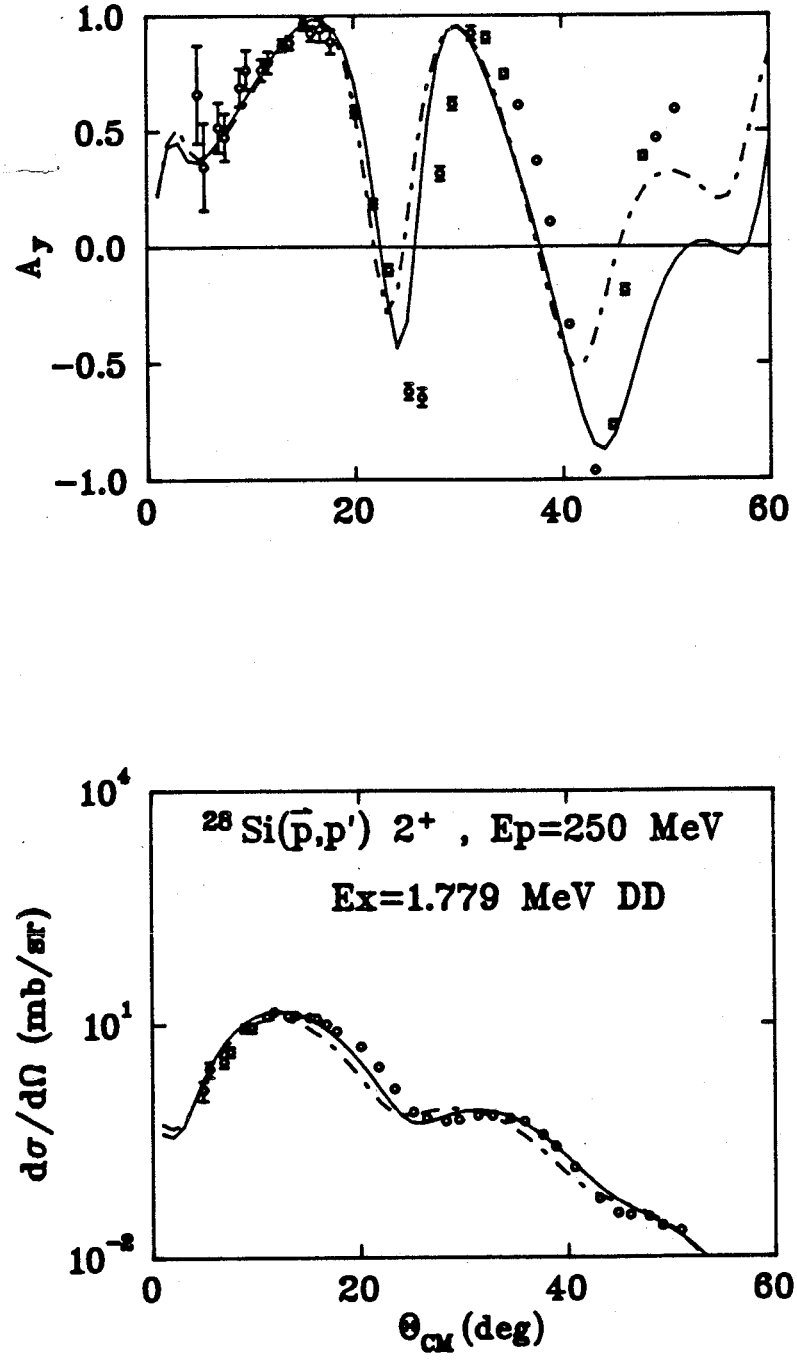

Figure 5.35 DD(dashed line) and DD with 75% optical potentials(solid line) for ^{28}Si 2^+ at 250 MeV.

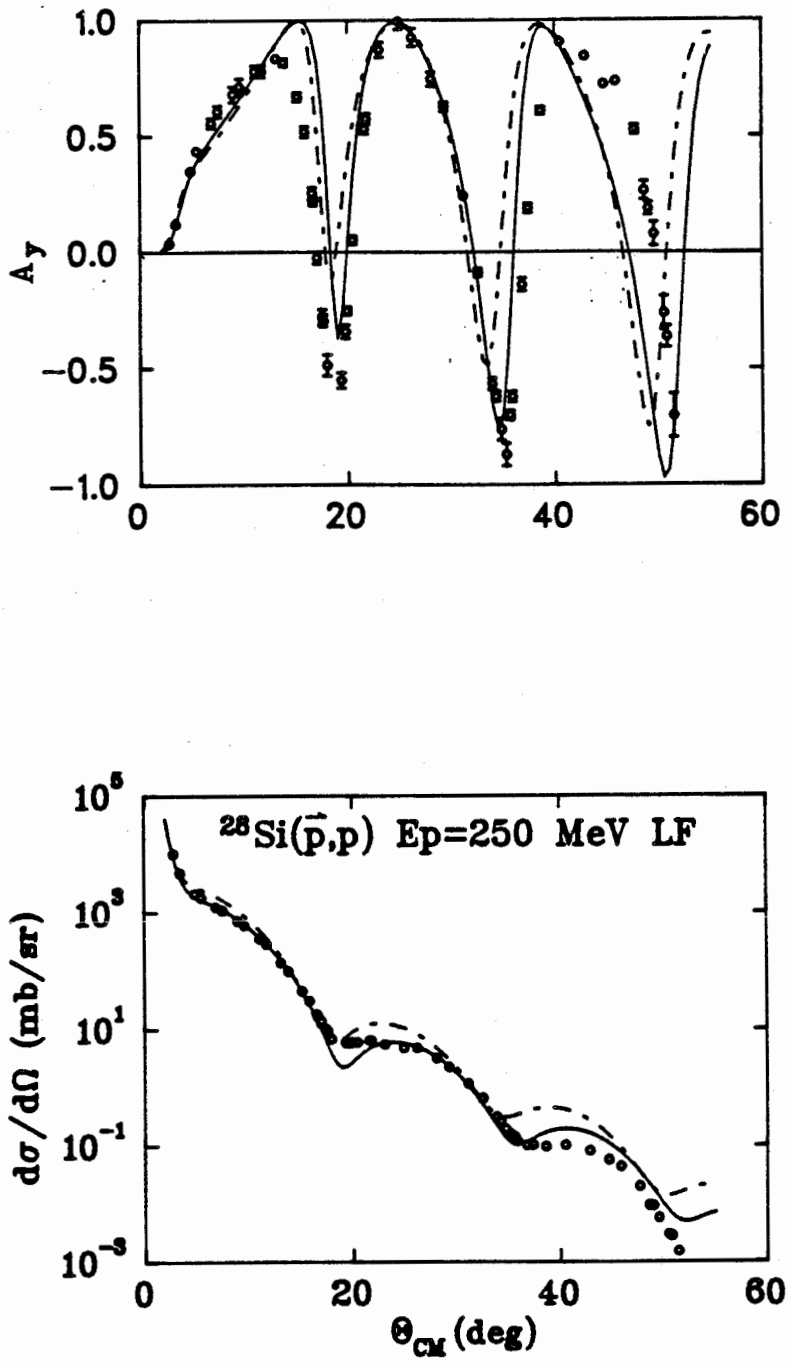

Figure 5.36 LF(dashed line) and LF with 75% optical potentials(solid line) for ^{28}Si 0^+ at 250 MeV.

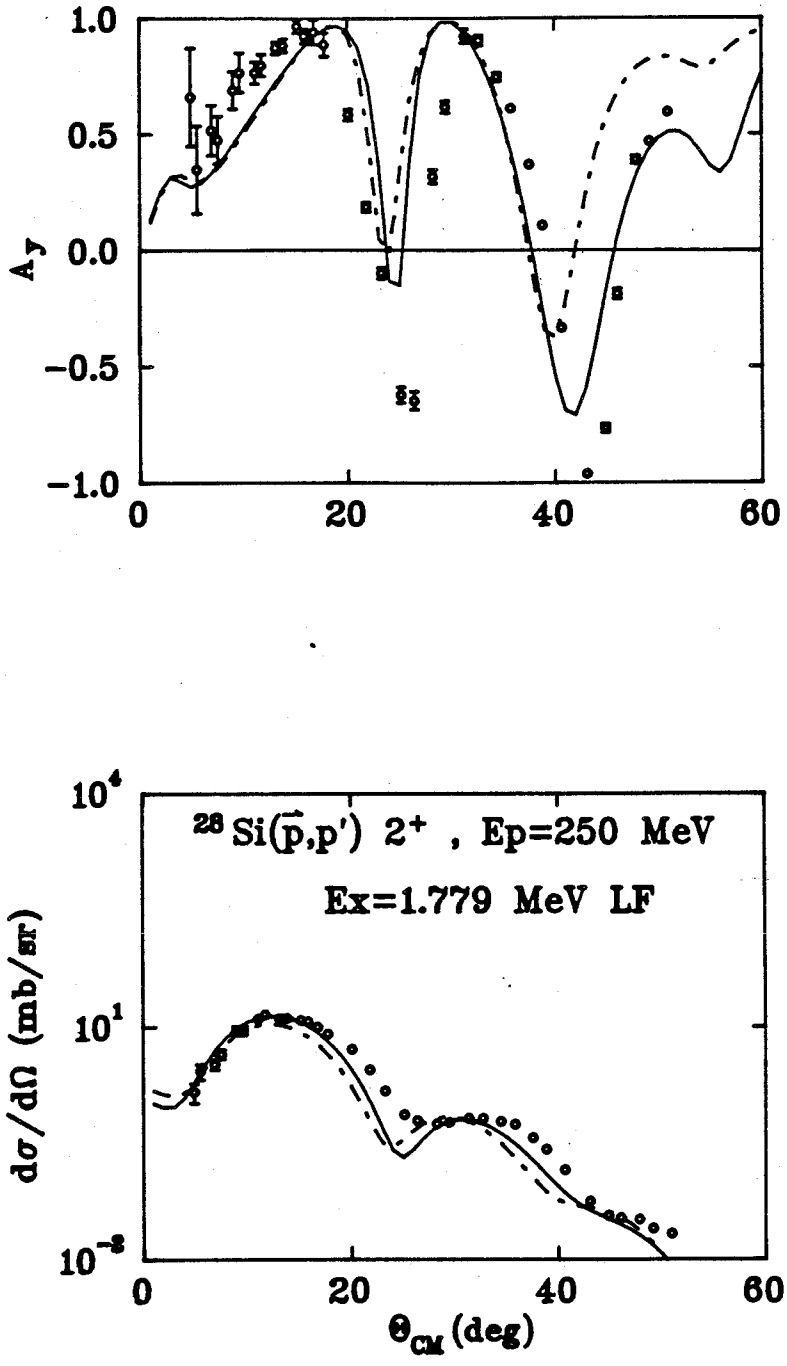

Figure 5.37 LF(dashed line) and LF with 75% optical potentials(solid line) for ^{28}Si 2^+ at 250 MeV.

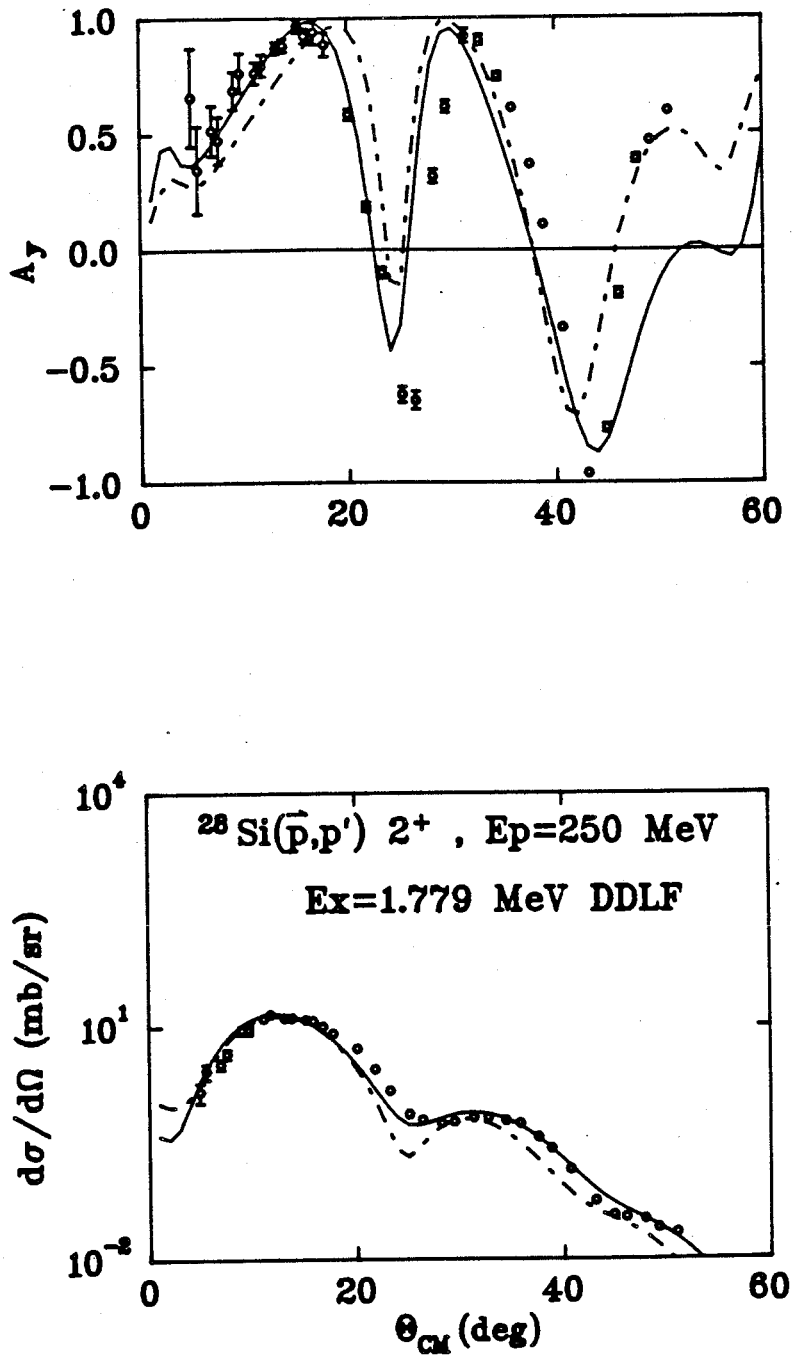

Figure 5.38 LF with 75% potentials(dashed line) and DD with 75% potentials(solid line) for ^{28}Si 2^+ at 250 MeV.

With the reduction on the optical potentials shown in table 5.5, it is found that the improvement can apply to both DD and LF at all energies which can be reached at TRIUMF. However, the reduction factor may not necessarily be the same at different energies or with different target nuclei. The LF result of ^{28}Si at 250 MeV beam energy is shown in figures 5.36 and 5.38. Table 5.6 shows the reaction cross section calculation with various models. These values are comparable with the results of Dymarz(Dy85).

Since DD is the medium-modified prediction from LF and is suitable in the energy range between 100 to 400 MeV, it can be expected that the 250 MeV result from DD should be better than that of LF. Figure 5.38 proves that the medium modification are important for the 2^+ state. Also, comparing figures 5.34 and 5.36, one can confirm immediately that DD is slightly more successful. This is due to Pauli blocking effects and a local modification of the short range force. On the other hand, LF only considers a single collision which is not affected by other particles nearby. The data from other energies and different targets are shown in figures 5.39 to 5.53 for both DD and LF predictions. Similar conclusions are obtained.

For high energy(see 400 MeV prediction), the assumption of a single collision within a very short period of time is not naive anymore because of the high velocity of the beam. Also the Fermi energy compared to the incident energy is so small that one can neglect the blocking effect from the Fermi sea.

Total reaction cross sections

Target	Ex(MeV)	Model	σ_R
^{28}Si	200	POM[1]	407.0
		POM[2]	396.2
		RPOM[1]	426.3
		RPOM[2]	395.7
		DWMM	815
		DWMM*.85	713
		DWIA	721
		DWIA*.85	590
^{28}Si	250	POM[1]	409.4
		POM[2]	408.3
		RPOM[1]	418.6
		RPOM[2]	401.6
		DWMM	743.6
		DWMM*.75	590.3
		DWIA	729
		DWIA*.75	590.4
^{28}Si	400	POM[1]	401.6
		POM[2]	389.2
		RPOM[1]	409.7
		RPOM[2]	439.9
		DWMM	671
		DWMM*.75	545
		DWIA	648.7
		DWIA*.75	530.7
^{24}Mg	250	POM[1]	418.3
		POM[2]	395.7
		RPOM[1]	393.1
		RPOM[2]	395.0
		DWMM	664
		DWMM*.75	523
		DWIA	650
		DWIA*.75	520

Table 5.6 The values of reaction cross sections of various models for (p,p) experiment: POM, RPOM, DD, LF, DD*rf(reduction factor) and LF*rf.

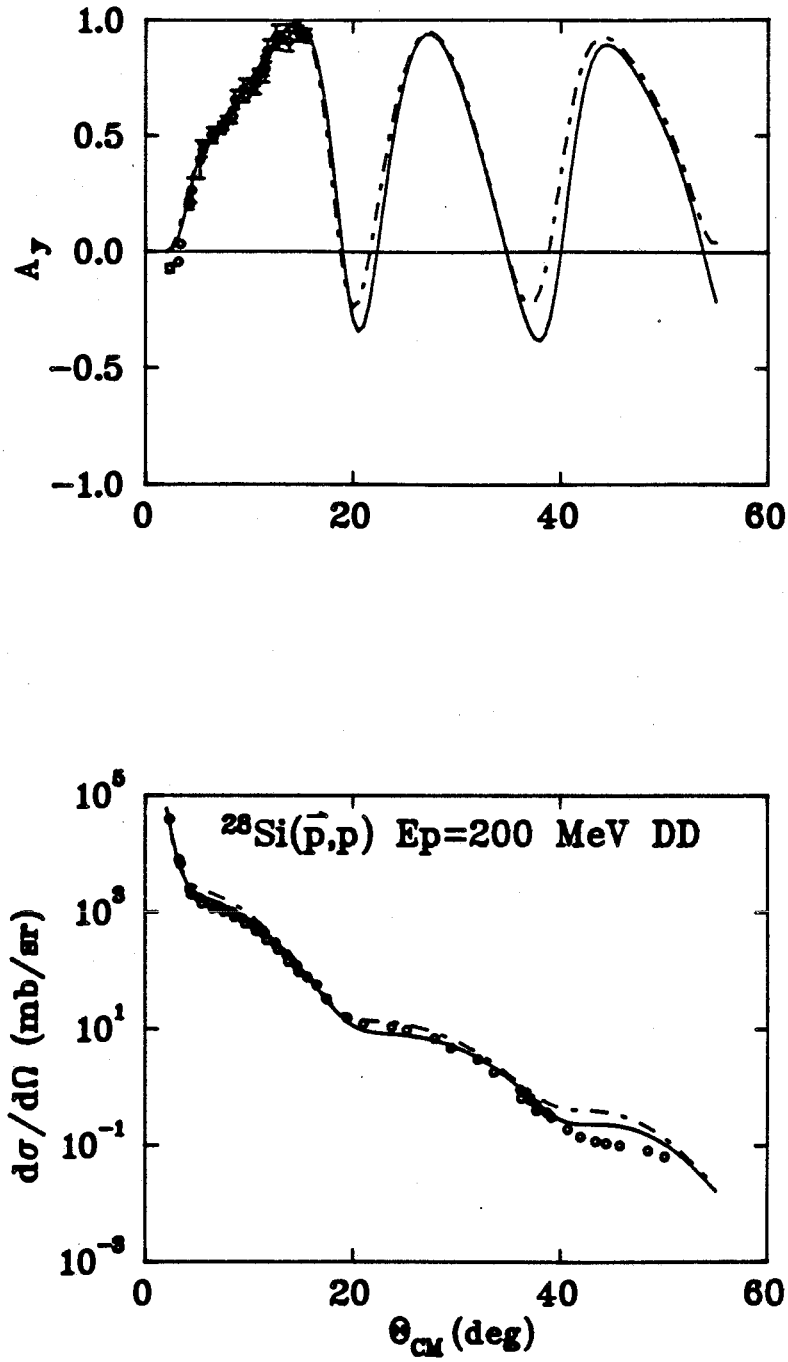

Figure 5.39 DD(dashed line) and DD with 75% optical potentials(solid line) for ^{28}Si 0^+ at 200 MeV.

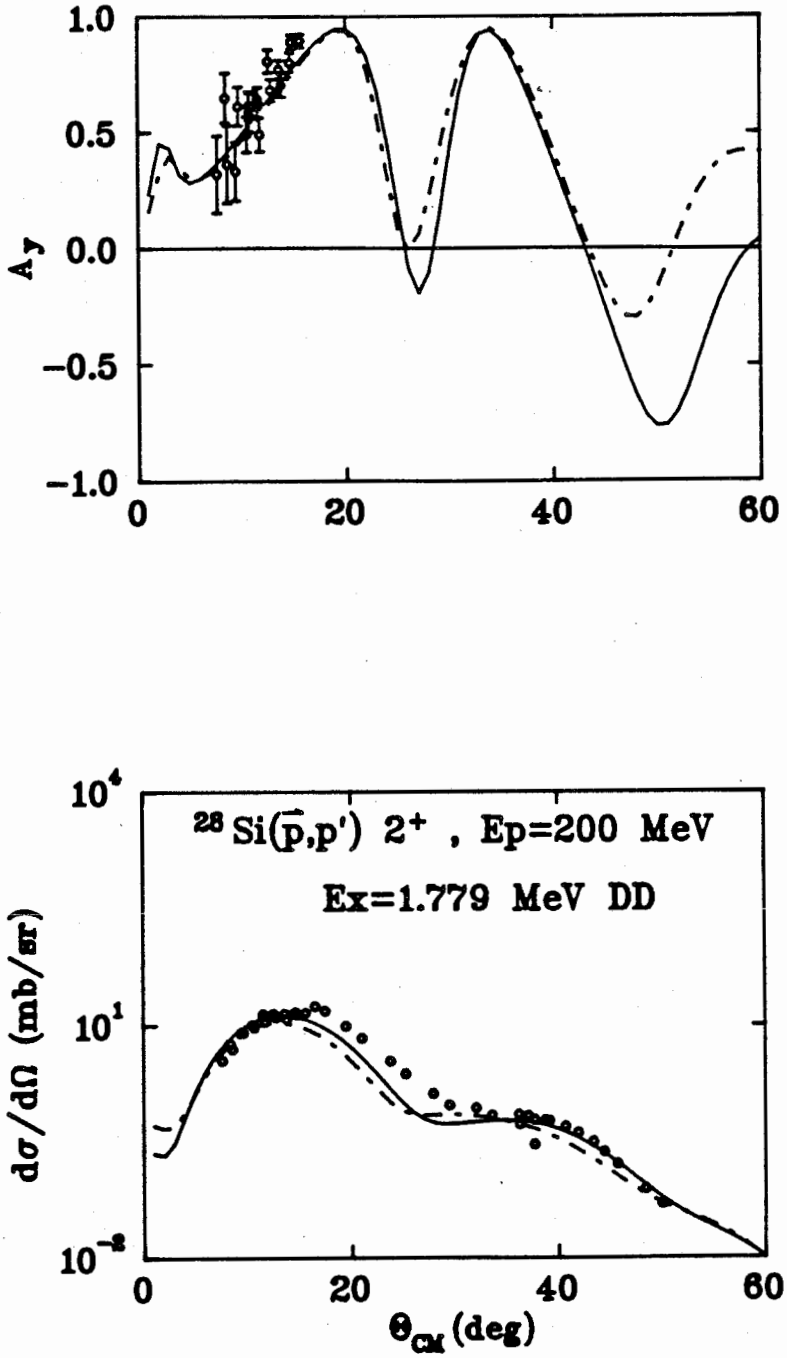

Figure 5.40 DD(dashed line) and DD with 75% optical potentials(solid line) for ^{28}Si 2^+ at 200 MeV.

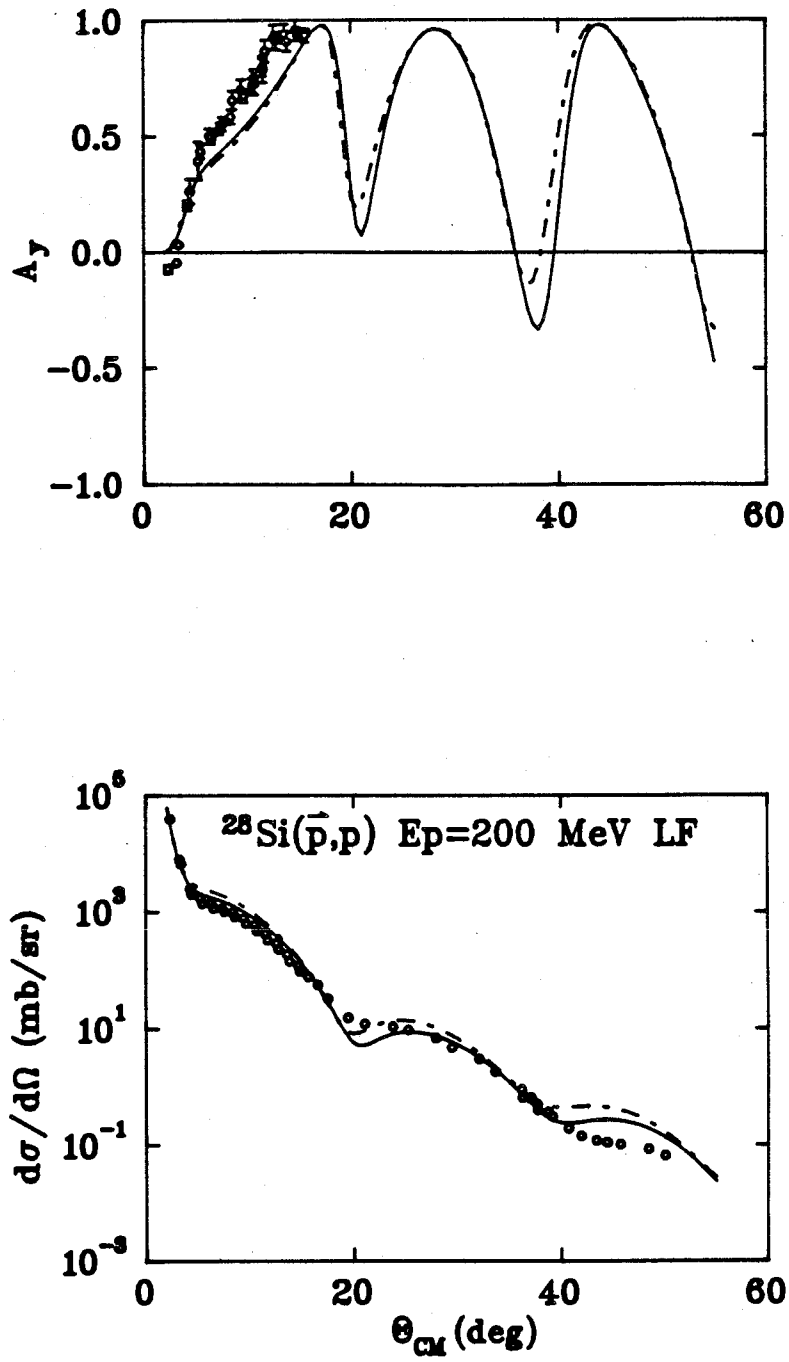

Figure 5.41 LF(dashed line) and LF with 75% optical potentials(solid line) for ^{28}Si 0^+ at 200 MeV.

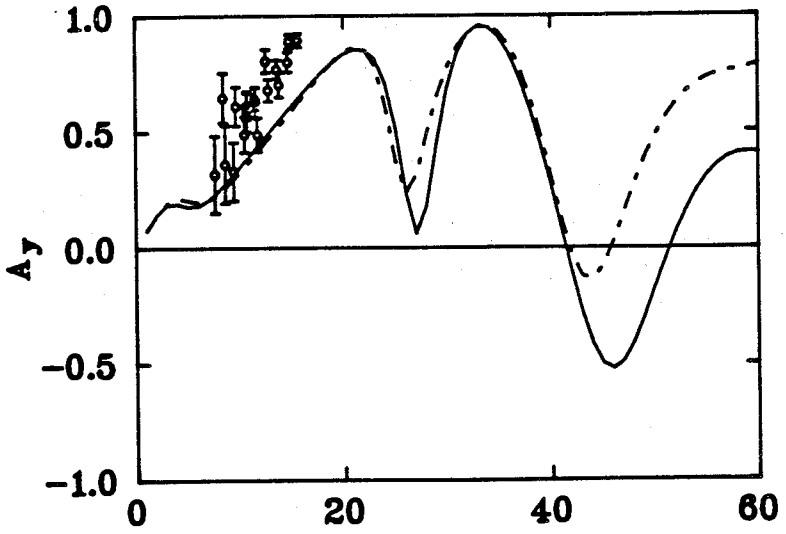

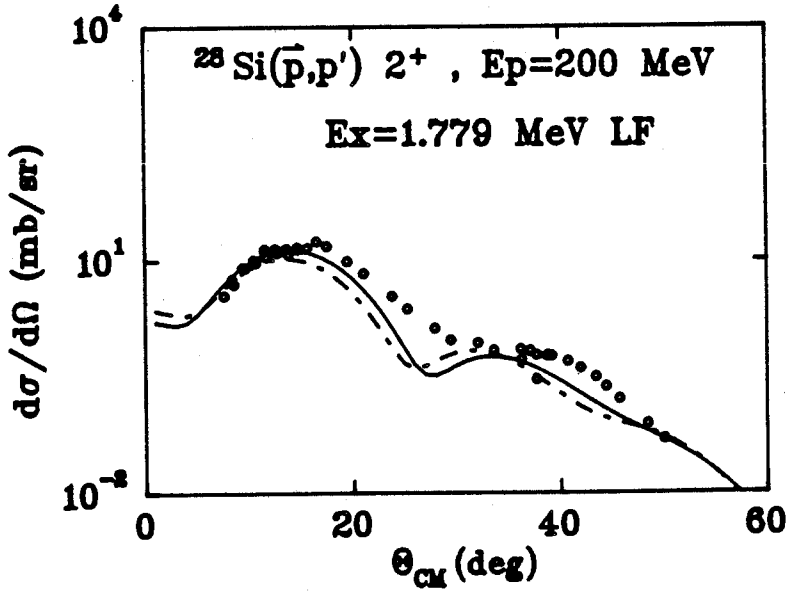

Figure 5.42 LF(dashed line) and LF with 75% optical potentials(solid line) for ^{28}Si 2^+ at 200 MeV.

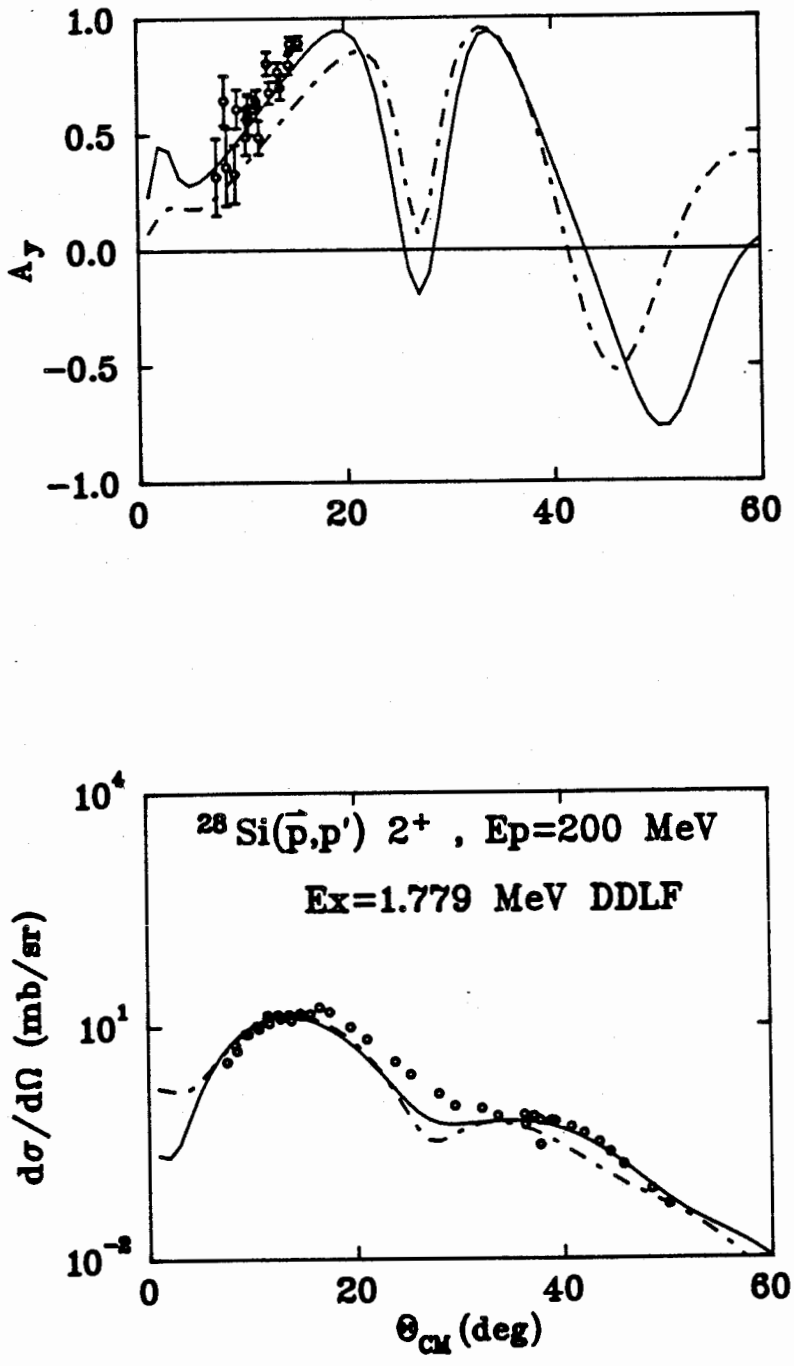

Figure 5.43 LF with 75% potentials(dashed line) and DD with 75% potentials(solid line) for ^{28}Si 2^+ at 200 MeV.

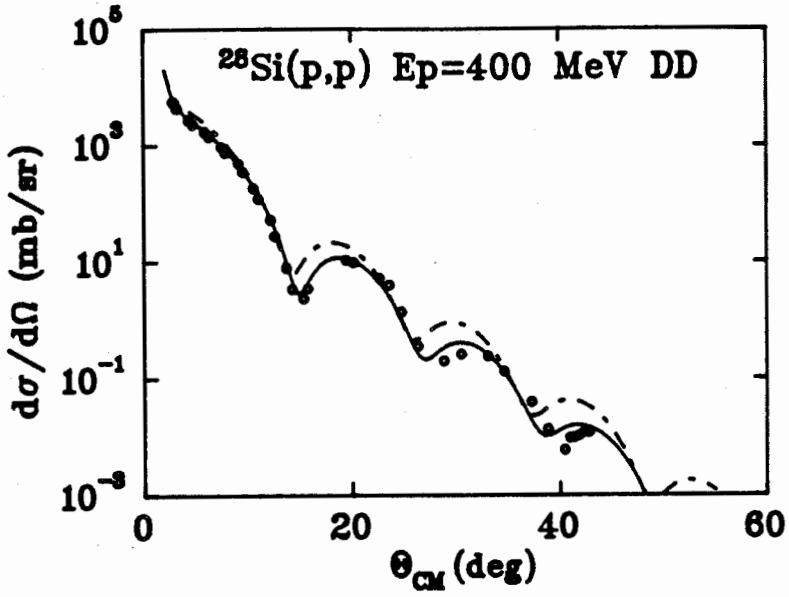

Figure 5.44 DD(dashed line) and DD with 75% optical potentials(solid line) for ^{28}Si 0^+ at 400 MeV.

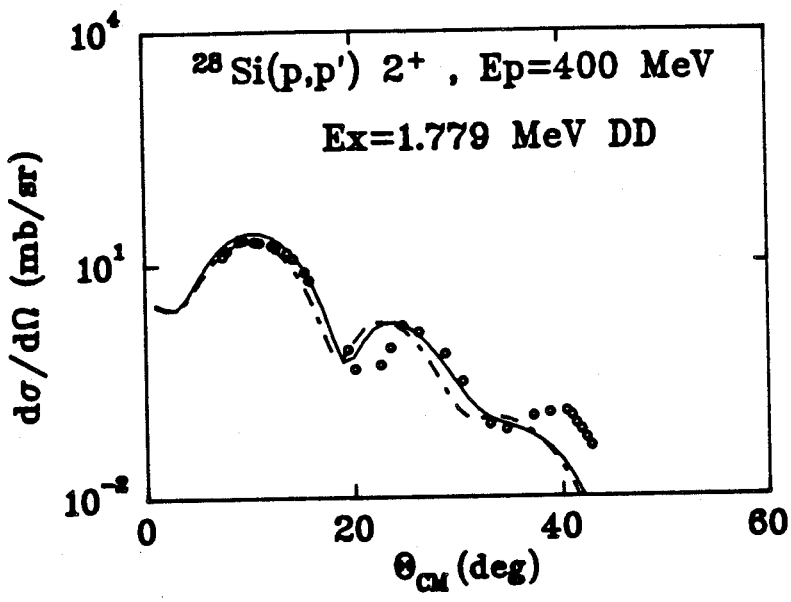

Figure 5.45 DD(dashed line) and DD with 75% optical potentials(solid line) for ^{28}Si 2^+ at 400 MeV.

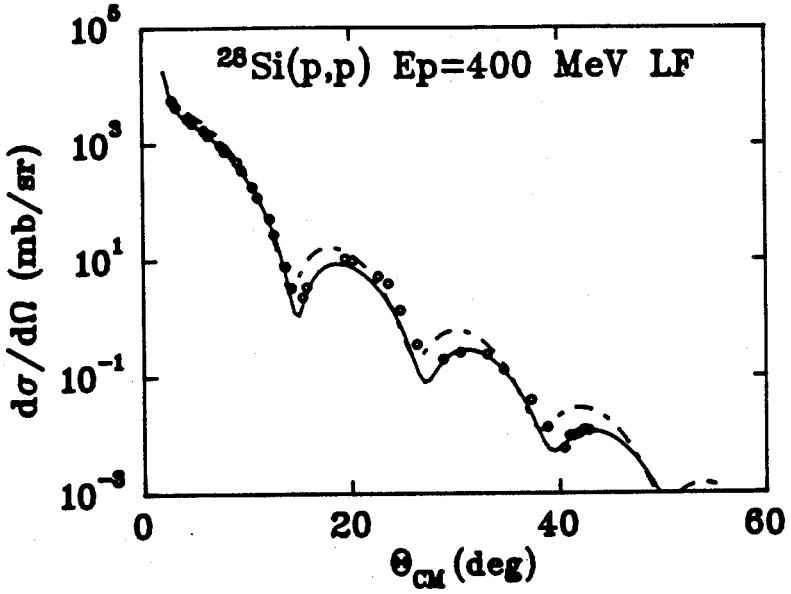

Figure 5.46 LF(dashed line) and LF with 75% optical potentials(solid line) for ^{28}Si 0^+ at 400 MeV.

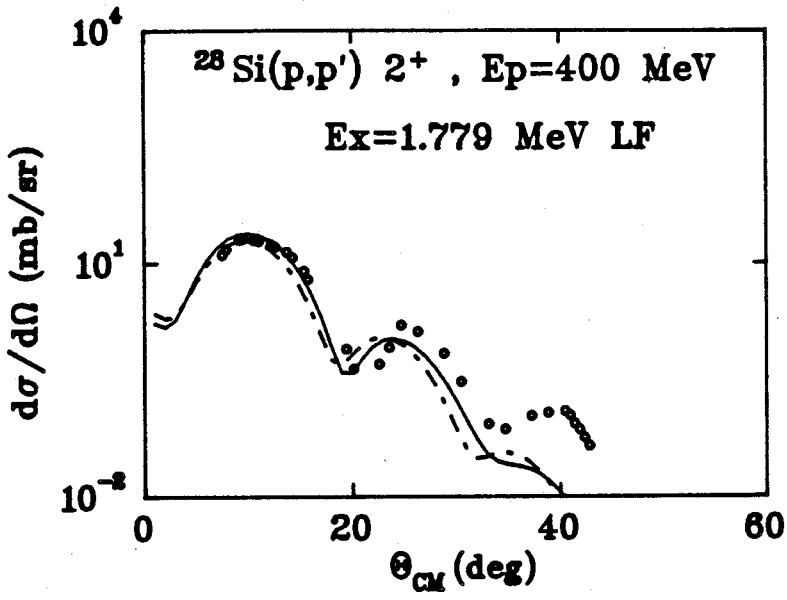

Figure 5.47 LF(dashed line) and LF with 75% optical potentials(solid line) for ^{28}Si 2^+ at 400 MeV.

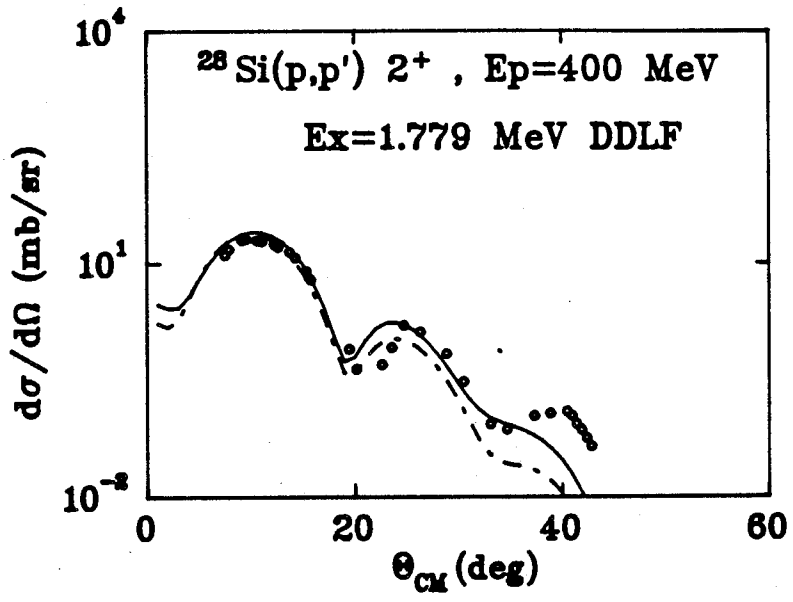

Figure 5.48 LF with 75% potentials(dashed line) and DD with 75% potentials(solid line) for ^{28}Si 2^+ at 400 MeV.

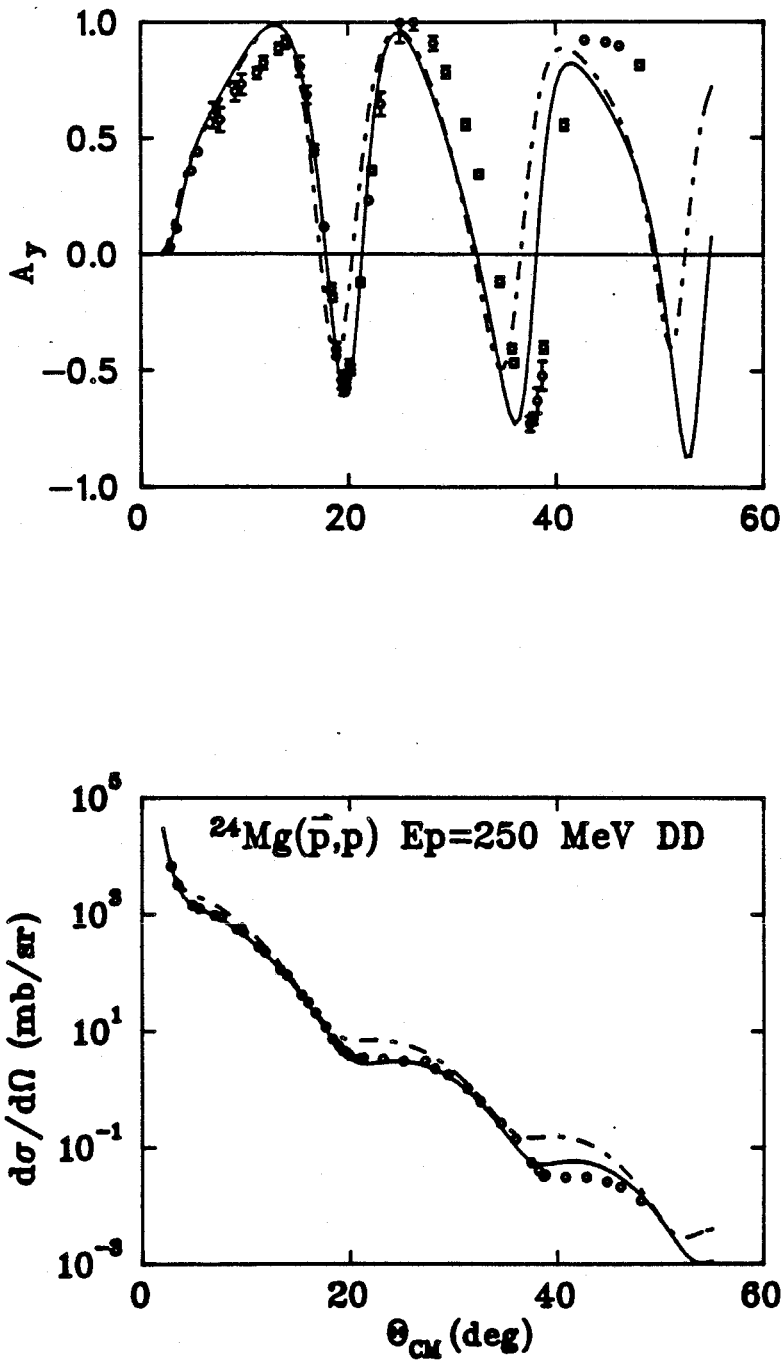

Figure 5.49 DD(dashed line) and DD with 75% optical potentials(solid line) for ^{24}Mg 0^+ at 250 MeV.

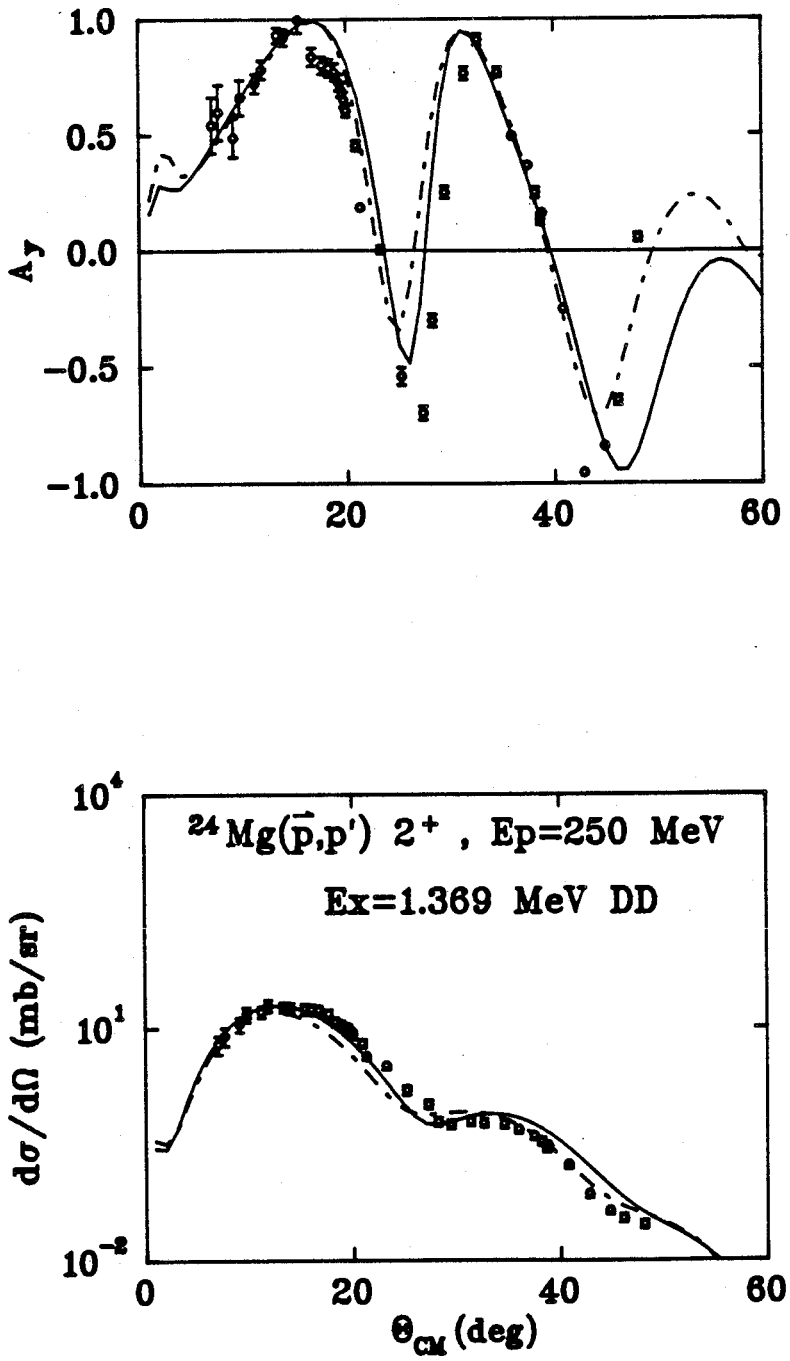

Figure 5.50 DD(dashed line) and DD with 75% optical potentials(solid line) for ^{24}Mg 2^+ at 250 MeV.

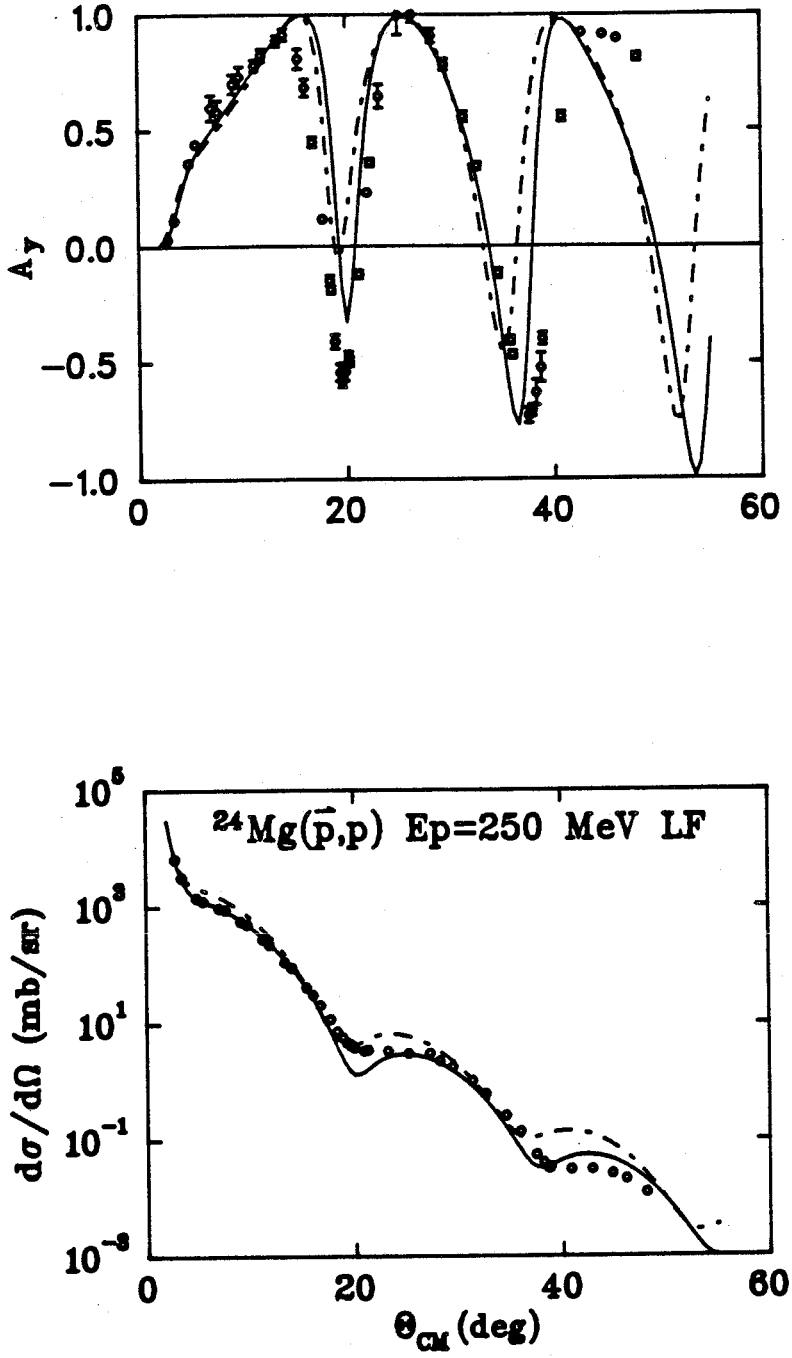

Figure 5.51 LF(dashed line) and LF with 75% optical potentials(solid line) for ^{24}Mg 0^+ at 250 MeV.

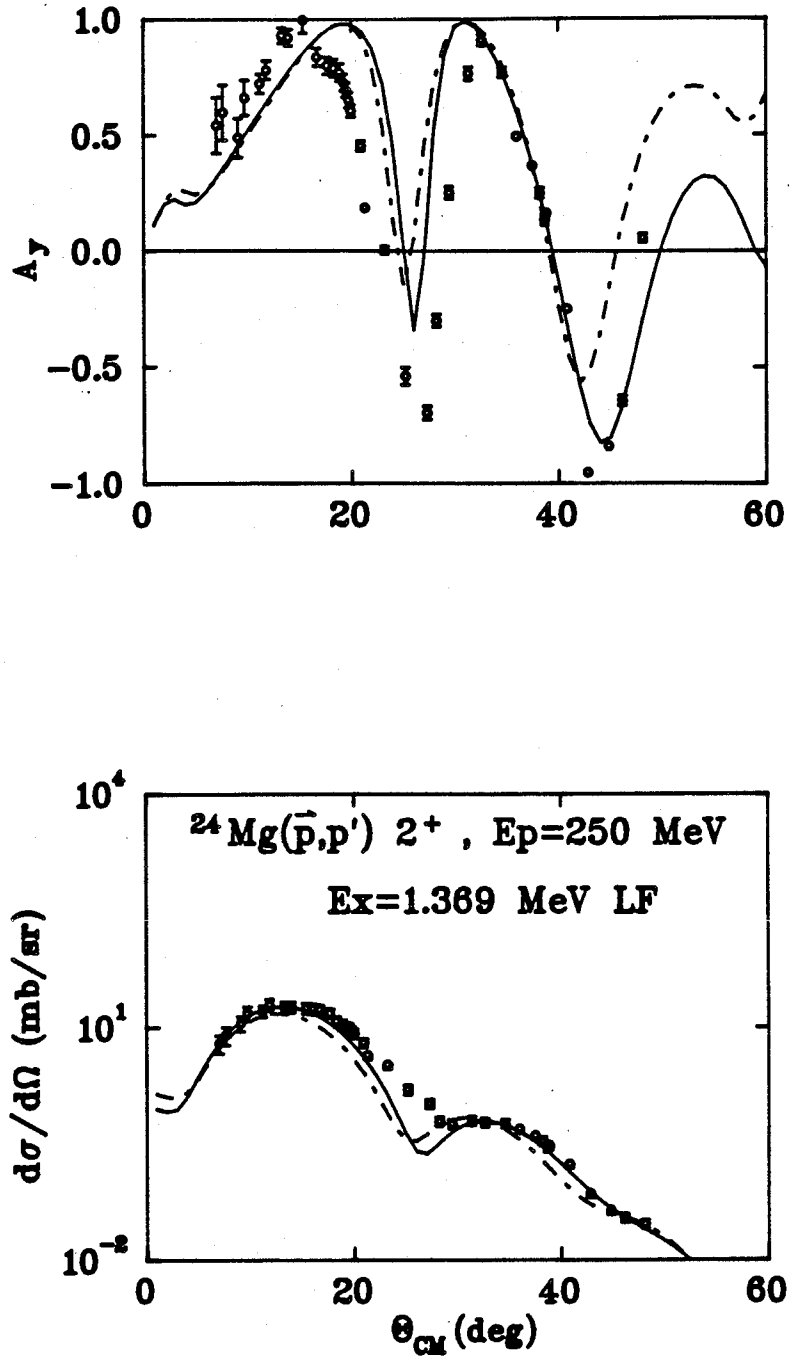

Figure 5.52 LF(dashed line) and LF with 75% optical potentials(solid line) for ^{24}Mg 2^+ at 250 MeV.

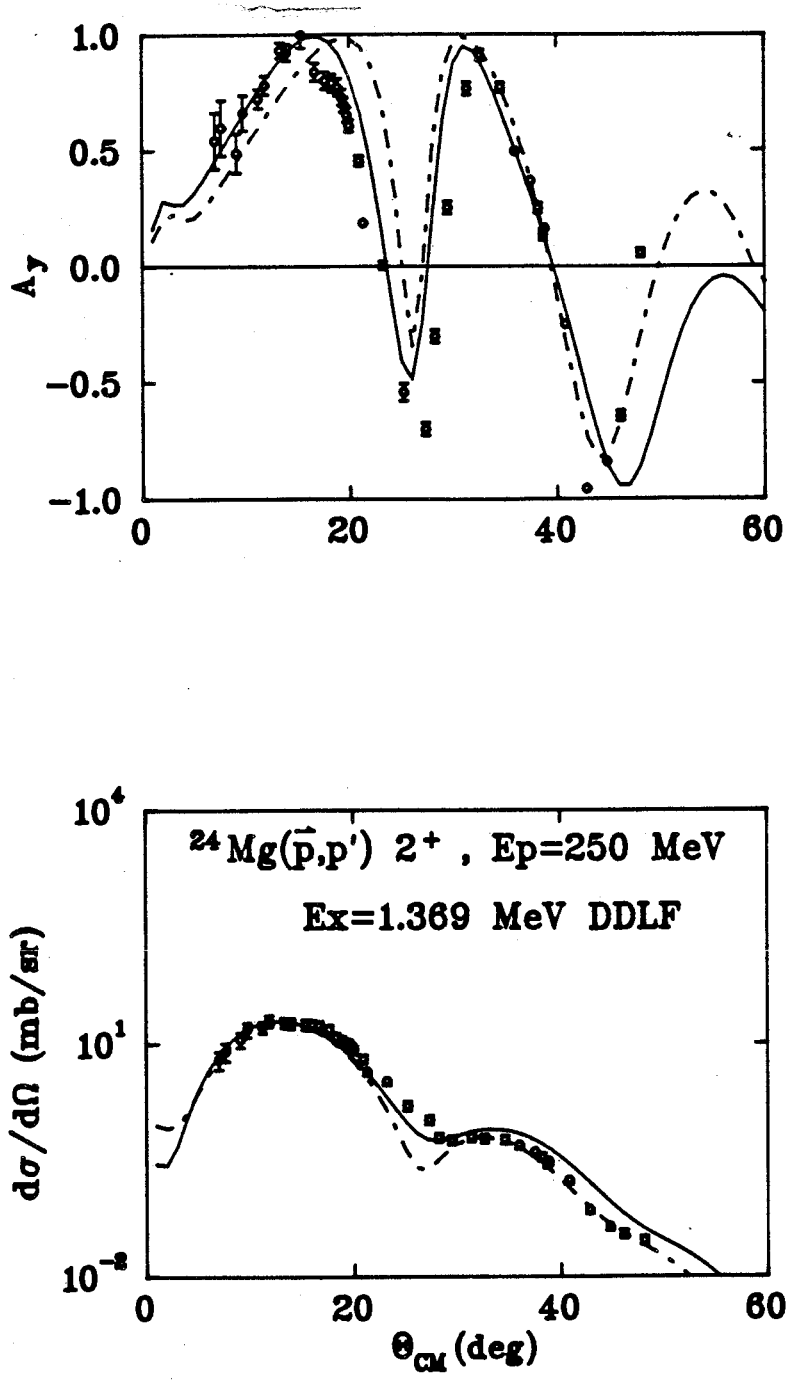

Figure 5.53 LF with 75% potentials(dashed line) and DD with 75% potentials(solid line) for ^{24}Mg 2^+ at 250 MeV.

Reducing the potential lowers the 0^+ cross section, thereby slightly increasing the 2^+ cross section. At the same time, the analyzing power oscillations become large and spread to larger angles. It is also shown that the reduction factor necessary to fit the 0^+ data also brings the results for the 2^+ into the better agreement.

CHAPTER VI

CONCLUSIONS

Proton elastic and inelastic scattering study offers the information about nuclear structure and nuclear interactions.

The Phenomenological Optical Model(POM) with all the Wood-Saxon(WS) potential parameters set free fits the data well. The Dirac (Relativistic) Phenomenological Optical Model(RPOM) gives an unconventional shape(wine bottle shape) of the effective optical potential where scalar and vector parts of the potentials are explained as the exchange of scalar and vector mesons. Fitted POM and RPOM optical potential parameters are not unique because the spin rotation parameter data are missing. Inside the nucleus, the potentials change dramatically. Even so, the observable calculations for the elastic process and the inelastic behavior are reasonably predicted from these ambiguous WS potential parameters. The RPOM with the radius-dependent potentials(wine-bottle shape) does slightly better than the POM at forward angles and local extrema.

Data for the collective 2^+ states of ^{28}Si and ^{24}Mg are well reproduced by the Distorted Wave POM(DWPOM) and the Dirac (Relativistic) DWPOM(RDWPOM) by using the optical parameters from elastic scattering and deforming the spherical nucleus to an ellipsoidal shape. The deformation lengths βR's (or the reduced transition probabilities B(EL)) were fitted. The electromagnetic result gives larger deformation length than proton scattering one.

Microscopic Optical Model calculations which are consistent with existing electromagnetic data reproduce experimental (p,p$'$) data for the proton energies above 200 MeV. The shell model structure used in this paper is extracted from the shell model

of Brown and Wildenthal. With the active sd-shell for the 2^+ state of ^{28}Si and ^{24}Mg, this study gives prediction of $(\vec{p}, p')$ cross sections larger than the experimental values. By reducing the cross sections to ~70% of its original value, good agreement is then obtained at various enerigies(60% for ^{24}Mg).

The prediction of DWIA and DWMM using shell model transition densities shows that the strong proton-nucleus interaction calculation has discrepencies when compared to differential cross section data. For the bombarding energies below 400 MeV, the Hamburg potential derived from the PARIS83 force which includes Pauli blocking and short range corrections does a slightly better job than the IA. The microscopic calculations with the Density Dependence (DD) or the Love-Franey (LF) interaction do not agree with the data in normalization and in angle extrema. Reducing all the optical potentials seems able to fix both the normalization and the angle shifts in one step for the ground state. This procedure shows that the microscopic Schrödinger formulation over-estimates the optical potentials for the light nuclei at intermediate energies, whereas the nuclear structure is less in doubt as the major problem.

It is very clear now that both microscopic and macroscopic calculations give larger cross section prediction than the experimental data if one takes the electromagnetic results as a guide. Two conclusions can be drawn:

1) Non-relativistic IA and MM overestimate the optical potentials.

2) The 2^+ state is overpredicted in both microscopic and macroscopic calculations. This indicates that the DWIA and DWMM are not quantitatively reliable to investigate low-lying collective states. It should be noted that all hadronic probes(see p.62) suffer from the same defect.

BIBLIOGRAPHY

(Ar81) L. G. Arnold, B. C. Clark, R. L. Mercer and P. Schwandt, Phys. Rev. **C23** 1949 (1981).

(Ar82) L. G. Arnold et al., Phys. Rev. **C25** 936 (1982).

(Bl64) J. S. Blair, Nuclear Spectroscopy with Direct Reactions, ANL–6878, (1964).

(Bl79) G. S. Blanpied et al., Phys. Rev. **C20** 1490 (1979).

(Br67) G. E. Brown, Unified Theory of Nuclear Models and Forces (Wiley, N. Y., 1967).

(Br83) B. A. Brown and B. H. Wildenthal, Phys. Rev. **C28** 2397 (1983).

(Br86) B. A. Brown, MSUCL, #572 (1986).

(Cl64) A. B. Clegg and G. R. Satchler, Nucl. Phys. **27**, (1961)431; Mitsuji Kawai, Tukuo Terasawa and Koichi Izumo, *ibid.* **59** 289 (1964).

(Co81) E. D. Cooper, Ph. D. thesis, University of Alberta (1983), unpublished.

(Ch72) A. Christy and O. F. Häusser, Nuclear Data Tables **11** 281 (1972).

(Du56) H. P. Duerr, Phys. Rev. **103** 469 (1956).

(Du78) A. Dudek-Ellis, V. Shkolnik and D. Dehnhard, Phys. Rev. **C18** 1039 (1978).

(Dy85) R. Dymarz, Phys. Lett. **155B** 5 (1985).

(En78) P. M. Endt and C. Van Der Leun, Nucl. Phys. **A310** 1 (1978).

(Fu36) W. H. Furry, Phys. Rev. **50** 784 (1936).

(Ge79) H. V. von Geramb and F. A. Brieva, in Microscopic Optical Potentials Conf. Proc., Hamburg 1978, ed. H. V. von Geramb (Springer, Berlin, 1979).

(Ge82) H. V. von Geramb and K. Nakano, in Interaction Between Medium Energy Nucleons in Nuclei, AIP Conf. Proc. No. **97**, edited by H. O. Meyer 44 (AIP, N. Y., 1982).

(Ge83) H. V. von Geramb, L. Rikus and K. Nakano in Proc. RNCP Int. Symp. on light ion reactions.

(Ha81) K. Hatanaka et al., Phys. Rev. Lett. **46** 15 (1981).

(Ha84) G. Haouat et al., Phys. Rev. **C30** 1795 (1984).

(Hi84) N. M. Hintz et al., Phys. Rev. **C30** 1976 (1984).

(Hi86) K. H. Hicks, MRS Manual, TRIUMF (1986).

(Hu86) D. A. Hutcheon et al. (1986) private communication.

(Ja70) D. F. Jackson, Nuclear Reactions (Methuen Co. Ltd., 1970).

(Ja74) C. W. de Jager, H. de Vries and C. de Vries, Atomic Data and Nuclear Data Tables **14** 479-508 (1974).

(Ji83) J. R. Tinsley, Ph. D. thesis, University of Oregon (1983), unpublished.

(Ka85) S. Kato et al., Phys. Rev. **C31** 1616 (1985).

(Ke59) A. K. Kerman, H. McManus and R. M. Thaler, Ann. Phys. **8** 551 (N. Y., 1959).

(Le79) R. De Leo et al., Phys. Rev. **C19** 646 (1979).

(Lo81) W. G. Love and M. A. Franey, Phys. Rev. **C24** 1073 (1981).

(Lo83) W. G. Love and M. A. Franey, Phys. Rev. **C27** 438(E) (1983).

(Mi74) W. Mittig et al., Nucl. Phys.**A233** 48 (1974).

(Ol84) C. Olmer, A. D. Bacher, G. T. Emery, W. P. Jones, D. W. Miller, H. Nann, P. Schwandt, S. Yen, T. E. Drake and R. J. Sobie, Phys. Rev. **C29** 361 (1984).

(Pi83) J. Piekarewicz, R. D. Amado, D. A. Sparrow and J. A. McNeil, Phys. Rev. **C28** 2392 (1983).

(Re71) H. Rebel et al., Phys. Rev. Lett. **26** 1190 (1971).

(Re72) H. Rebal et al., Nucl. Phys. **A182** 145 (1972).

(Ri84) L. Rikus, K. Nakano, and H. V. von Geramb, Nucl. Phys. **A414** 413 (1984).

(Sa83) G. R. Satchler, Nucl. Phys. **A394** 349-359 (1983).

(Sa83a) R. I. Sawafta, M. Sc. thesis, University of Alberta (1983), unpublished.

(Sh68) H. S. Sherif, Ph. D. thesis, University of Washington (1968), unpublished.

(Sh69) H. S. Sherif, Nucl. Phys. **A131** 532 (1969).

(Sh85) H. S. Sherif, E. D. Cooper and R. I. Sawafta, Phys. Lett. **158B** 193 (1985).

(Sh86) H. S. Sherif, R. I. Sawafta and E. D. Cooper, Nucl. Phys. **A449** 709 (1986).

(Ta65) T. Tamura, Nucl. Phys. **73** 241 (1965).

(Wi85) B. H. Wildenthal, B. A. Brown and I. Sick, Phys. Rev. **C32** 2185 (1985).

(Ya76) G. C. Yang, P. P. Singh, A. van der Woude and A. G. Drentje, Phys. Rev. **C13** 1376 (1976).

(Ye83) S. Yen, Ph. D. thesis, University of Toronto (1983), unpublished.